



NEURONS ARE POISED NEAR THE EDGE OF CHAOS

LEON CHUA

*Department of Electrical Engineering and Computer Sciences,
University of California, Berkeley,
Berkeley, CA 94720, USA*

*TUM Affiliated Distinguished Professor,
Fakultat für Elektrotechnik und Informationstechnik,
Technische Universität München,
Arcisstrasse 21, 80333 München, Germany
chua@eecs.berkeley.edu*

VALERY SBITNEV

*Department of Electrical Engineering and Computer Sciences,
University of California, Berkeley,
Berkeley, CA 94720, USA*

*St. Petersburg Nuclear Physics Institute, NRC Kurchatov Institute,
Gatchina, Leningrad district, 188350, Russia
valery.sbitnev@gmail.com*

HYONGSUK KIM

*Division of Electronics Engineering,
Chonbuk National University,
Jeonju, Jeonbuk, 561-756, South Korea
hskim@jbnu.ac.kr*

Received February 15, 2012; Revised March 15, 2012

This paper shows the *action potential (spikes)* generated from the Hodgkin–Huxley equations emerges near the *edge of chaos* consisting of a tiny subset of the *locally active* regime of the HH equations. The main result proves that the eigenvalues of the 4×4 Jacobian matrix associated with the mathematically intractable system of four nonlinear differential equations are identical to the zeros of a *scalar complexity function* from complexity theory. Moreover, we show the loci of a pair of complex-conjugate zeros migrate continuously as a function of an externally applied DC current excitation emulating the net synaptic excitation current input to the neuron. In particular, the pair of complex-conjugate zeros move from a *subcritical* Hopf bifurcation point at low excitation current to a *super-critical* Hopf bifurcation point at high excitation current. The spikes are generated as the excitation current approaches the vicinity of the *edge of chaos*, which leads to the onset of the *subcritical* Hopf bifurcation regime. It follows from this in-depth qualitative analysis that *local activity is the origin of spikes*.

Keywords: Action potential; spikes; neurons; axons; Hodgkin–Huxley equations; Hodgkin–Huxley axon; memristor; complexity function; edge of chaos; local activity; Hopf bifurcation; subcritical Hopf bifurcation; super-critical Hopf bifurcation; complexity; limit cycles; basin of attraction; eigenvalues; stability.

1. Introduction

One of the marvels of the HH (Hodgkin–Huxley) equations [Hodgkin & Huxley, 1952] is its ability to generate an *action potential (spikes)* in response to an external current excitation emulating the net synaptic current excitation. Although the spikes are consistently generated numerically, no one knows the physical and mathematical origin of the action potential (spikes). The objective of this paper is to demonstrate that *local activity* [Chua, 2005] is the origin of spikes. In particular, we will show that neurons are poised near a tiny subset of the local activity regime, called the *edge of chaos*. We will derive the domain of the edge of chaos by deriving an explicit scalar complexity function [Chua, 2005] $Z(s; I_{\text{ext}})$ called the impedance function of the small-signal Hodgkin–Huxley memristor circuit model derived in [Chua et al., 2012].

The main theorem of this paper asserts that the zeros of the scalar function

$$Y(s; V_m) \triangleq \frac{1}{Z(s; V_m)} \quad (1)$$

called the *small-signal admittance* of the Hodgkin–Huxley memristor circuit model, are identical to the *eigenvalues* of the 4×4 Jacobian matrix of the HH equation, calculated at the equilibrium point $V_m = V(Q(I_{\text{ext}}))$ of the HH equations, for each constant DC excitation current I_{ext} .¹

Here $s = \sigma + i\omega$ denotes the complex variable associated with the Laplace transform $\hat{v}(s)$ of a time function $v(t)$ [Chua et al., 2012] and I_{ext} denotes an external current source applied to the Hodgkin–Huxley axon circuit model shown in Fig. 1.

1.1. Recap on Hodgkin–Huxley equations

A typical neuron consists of a single nerve fiber called an *axon* shown in Fig. 2(a) attached to the

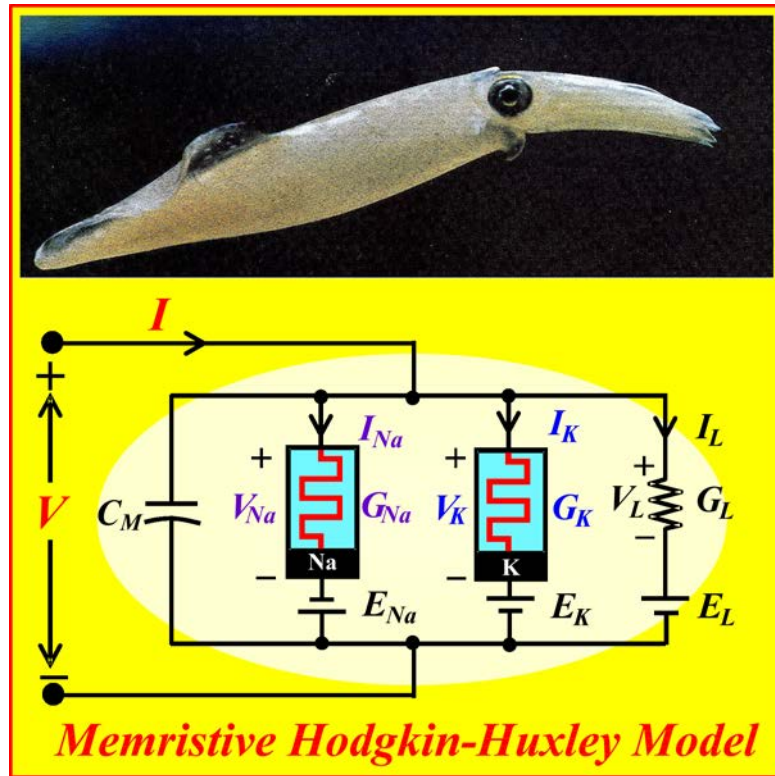
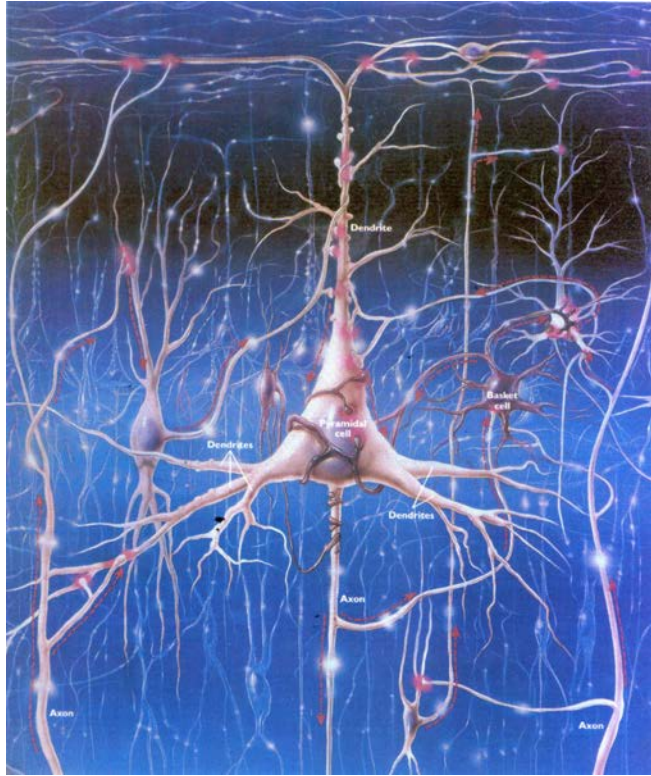
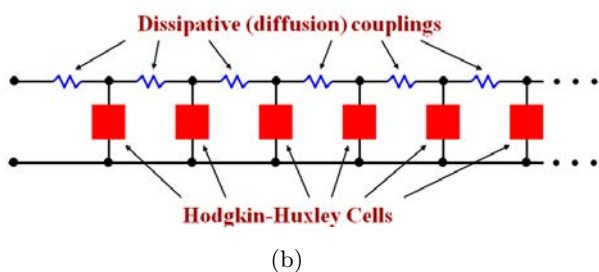
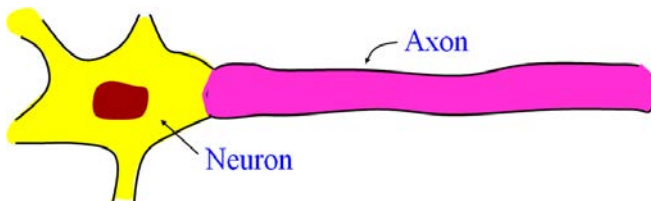


Fig. 1. The Hodgkin–Huxley axon is made of a capacitor, a resistor, three batteries and two memristors.

¹This theorem is valid not only for the four-dimensional HH equation, but for any system of n differential equations. This theorem is a powerful tool because instead of calculating the eigenvalues of a high dimensional $n \times n$ matrix, one only has to calculate the roots (zeros) of a scalar *polynomial* equation of a single variable s , for any integer n .



(a)



(b)

Fig. 2. Axons from neurons in (a) can be modeled as a one-dimensional transmission line in (b) made of linear passive resistors and nonlinear 2-terminal Hodgkin–Huxley cells.

lower cone-shaped area (called the axon hillock) of the cell body (called the soma). When the net current excitations coming from the *dendrites*, which made contacts with the axons from neighboring neurons, exceed a certain threshold, a large but

narrow electrical pulse called an *action potential (spike)* emerges from the axon hillock and traverses down the axon with a fixed shape and undiminished signal amplitude. Depending on the strength of the net excitation current, as well as on the nature of the neuron, the action potential may emerge as a single *spike*, or as a burst of many closely-spaced identical pulses, called a *spike train* in this paper. Hodgkin and Huxley have shown that the axon may be modeled as an electrical cable made of a chain of identical linear passive resistors and a 2-terminal device, as depicted schematically in Fig. 3 and dubbed a Hodgkin–Huxley cell in Fig. 2(b). Each cell is an electrical circuit (shown in Fig. 1 of [Hodgkin & Huxley, 1952]) consisting of a capacitor, a linear resistor, three batteries, and two unconventional elements identified by Hodgkin and Huxley as *time-varying resistors*, which we now know was a serious blunder that had led to numerous anomalies and paradoxes, and had hindered progress on neural physiology and brain science for over 70 years. Such anomalies had recently been definitively resolved by substituting the potassium and sodium time-varying resistors, by a potassium ion-channel memristor, and a sodium ion-channel memristor, respectively, as depicted in Fig. 1 [Chua *et al.*, 2012]. The revised circuit model in Fig. 1 is called the memristive *Hodgkin–Huxley axon model*. It is described by a system of four nonlinear differential equations, which we reproduced below from

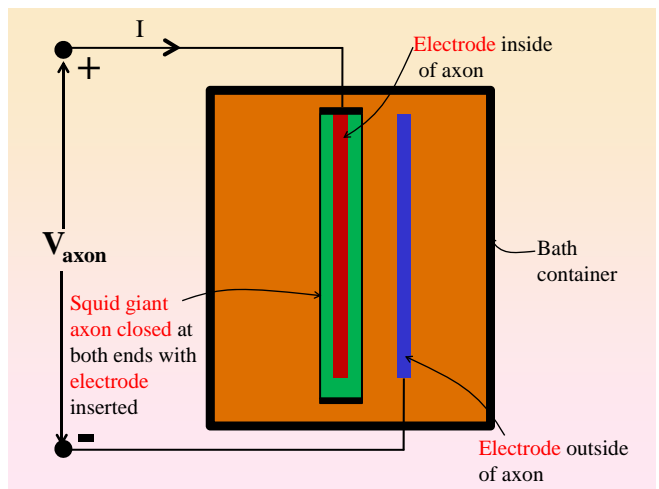


Fig. 3. The Hodgkin–Huxley cell is a simplified 2-terminal electrical circuit model of the giant axon of the North Atlantic squid *Loligo* extracted and repackaged as a 2-terminal electrical device in the above vignette.

Table 1 of [Chua et al., 2012]:

Table 1. Hodgkin–Huxley equations.

	$I = C_M \frac{dV}{dt} + \bar{g}_K n^4 (V - V_K) + \bar{g}_{Na} m^3 h (V - V_{Na}) + \bar{g}_l (V - V_l)$	(2a)
where,	$dn/dt = \alpha_n(1 - n) - \beta_n n,$	(2b)
	$dm/dt = \alpha_m(1 - m) - \beta_m m,$	(2c)
	$dh/dt = \alpha_h(1 - h) - \beta_h h,$	(2d)
and	$\alpha_n = 0.01(V + 10)/\left(\exp \frac{V + 10}{10} - 1\right),$	(2e)
	$\beta_n = 0.125 \exp(V/80),$	(2f)
	$\alpha_m = 0.1(V + 25)/\left(\exp \frac{V + 25}{10} - 1\right),$	(2g)
	$\beta_m = 4 \exp(V/18),$	(2h)
	$\alpha_h = 0.07 \exp(V/20),$	(2i)
	$\beta_h = 1/\left(\exp \frac{V + 30}{10} + 1\right),$	(2j)

We remark that the variables and symbols in Eq. (2) are originally chosen by Hodgkin–Huxley and *are different* from those found in recent literatures where the reference polarity of the voltage V , and the reference direction of the current I are defined as the *negative* of the voltages and currents in Fig. 1. We have opted to adopt the reference assumption in [Hodgkin & Huxley, 1952] for ease in comparison of our results with those from Hodgkin and Huxley.

The parameters in the HH equations in Table 1 are reproduced from [Hodgkin & Huxley, 1952] and listed in Table 2.

Table 2. Parameter values for HH equations.

$C_M = 1.0 \mu\text{F}/\text{cm}^2$
$V_{Na} = -115 \text{ mV}$
$V_K = 12 \text{ mV}$
$V_l = -10.613 \text{ mV}$
$\bar{g}_{Na} = 120 \text{ mS/cm}^2$
$\bar{g}_K = 36 \text{ mS/cm}^2$
$\bar{g}_l = 0.3 \text{ mS/cm}^2$

In particular, we caution the reader that the voltages v , v_{Na} , v_K , and v_l are *shifted* by a referenced equilibrium “resting” voltage E_r as defined in Eq. (3), whose value ranges between 60 mV to 70 mV, in the literature.

$$V = E - E_r \quad (3a)$$

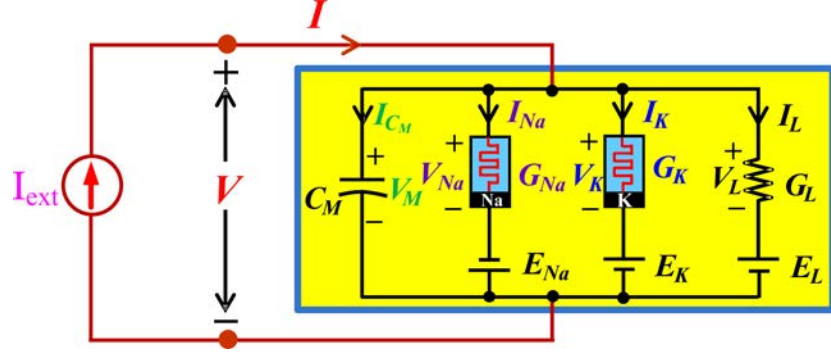
$$V_{Na} = E_{Na} - E_r \quad (3b)$$

$$V_K = E_K - E_r \quad (3c)$$

$$V_l = E_l - E_r \quad (3d)$$

1.2. Equilibrium point and resting potential V_m as function of I_{ext}

Since most deep insights concerning *local activity* and *edge of chaos* can be uncovered from an analysis of the linearized differential equations about the equilibrium points of its associated nonlinear dynamical system, we will derive the relationship between the resting potential (equilibrium voltage) V_m as a function of the constant (DC) external excitation current I_{ext} applied across the two external terminals of the Memristive Hodgkin–Huxley model in Fig. 1, as shown in Fig. 4. Since

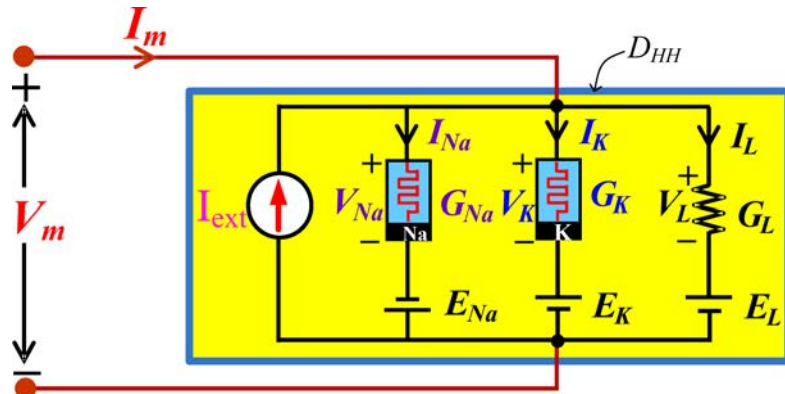
Fig. 4. Hodgkin–Huxley axon driven by external current source I_{ext} .

$I_{C_M} = C_M dV_{C_M}/dt = 0$ at rest, we can delete the capacitor C_M from Fig. 4 and attach a new pair of external terminals, as depicted in the redrawn circuit in Fig. 5, with I_m representing the external “membrane” current, and V_m representing the membrane voltage across the “space-clamped” electrodes depicted in Fig. 3 [Hodgkin & Huxley, 1956]. Observe that

$$V_m = V_{Na} - E_{Na} = V_K + E_K = V_L + E_L \quad (4)$$

where $E_{Na} = 115 \text{ mV}$, $E_K = 12 \text{ mV}$, and $E_L = -10.613 \text{ mV}$, are extracted from Table 2.² The two terminals are added in Fig. 5 for pedagogical reasons when the capacitor C_M will be reconnected in our later sections. For now, $I_m = 0$ at equilibrium, i.e. with the capacitor replaced by an open circuit. To derive the relationship between the resting

voltage V_m as a function of the DC excitation current I_{ext} in Fig. 5, let us derive the V_m versus I_m curve of the composite 1-port D_{HH} ³ for each value of I_{ext} , and identify the coordinate of V_m at the point where the V_m - I_m curve intersects the $I_m = 0$ (horizontal) axis. For maximum efficiency and clarity, let us derive first the V - I curve of the Hodgkin–Huxley DC circuit model from [Chua *et al.*, 2012] which we have reproduced as Fig. 6(a). Pedagogically, it is convenient to define three new 1-ports D_{Na} , D_K , and D_L as depicted in Fig. 6(b), which include the battery as a part of the 1-port. Now observe that Kirchhoff Current Law (KCL) [Chua, 1969] implies $I'_{Na} = I_{Na}$, $I'_K = I_K$, and $I'_L = I_L$. Similarly, Kirchhoff Voltage Law (KVL) [Chua, 1969] implies $V'_{Na} = V_{Na} - E_{Na} = V_{Na} - 115$, $V'_K = V_K + E_K = V_K + 12$, and $V'_L = V_L + E_L = V_L - 10.613$.

Fig. 5. Hodgkin–Huxley DC circuit model in parallel with the external current source I_{ext} .

²We cautioned the reader that the discrepancy in the negative sign of $V_{Na} = -115 \text{ mV}$ in Table 2 is due to an inconsistency between the Na battery polarity in Fig. 1 and Eq. (2b) in [Hodgkin & Huxley, 1952].

³In electrical circuit theory [Chua, 1969, 1980], any box containing circuit elements where one pair of wires are brought out for inter-connection with other circuit element is called *1-port*.

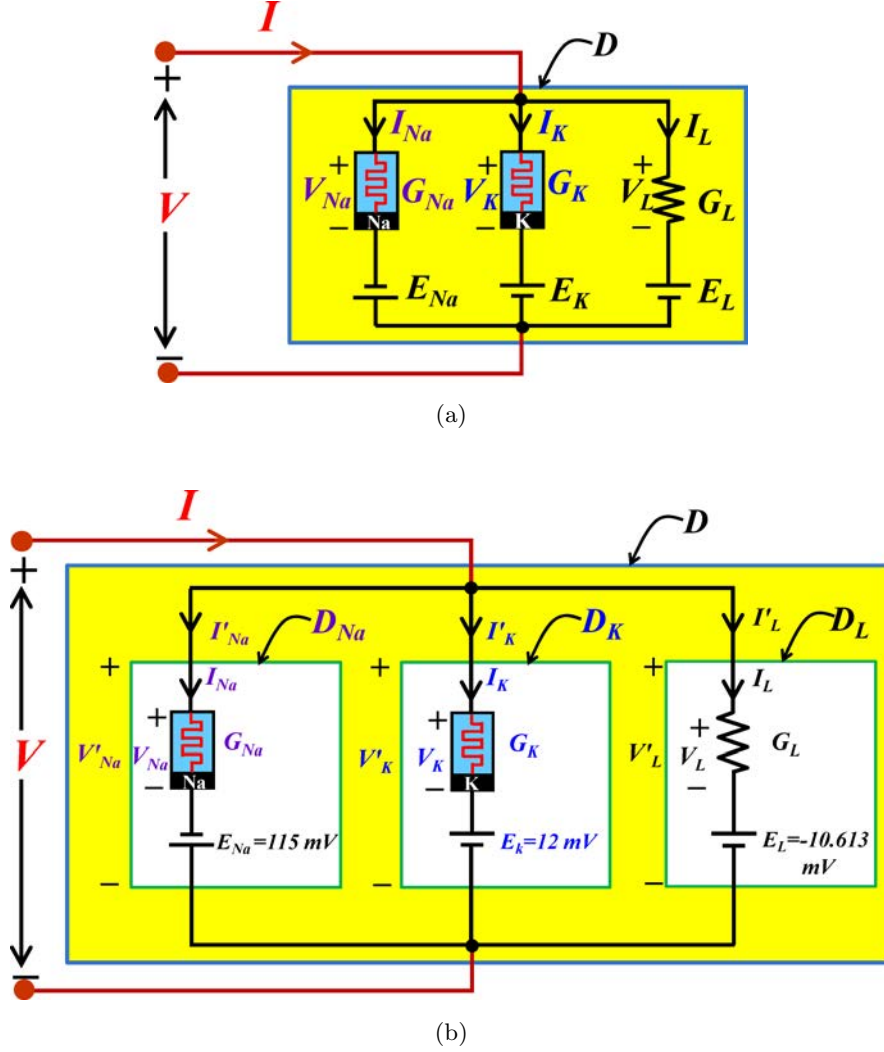


Fig. 6. The Hodgkin–Huxley DC circuit model in (a) can be viewed as 3 one-ports D_{Na} , D_K , and D_L [depicted in (b)] connected in parallel.

It follows that the $V'_{Na} - I'_{Na}$ curve of D_{Na} is simply obtained by translating the $V_{Na} - I_{Na}$ curve of the sodium ion channel memristor from Fig. 22 of [Chua et al., 2012] by 115 mV to the left as illustrated graphically in the upper part of Fig. 7. Similarly, the $V'_K - I'_K$ curve of D_K is simply obtained by translating the $V_K - I_K$ curve of the potassium ion-channel memristor from Fig. 20 of [Chua et al., 2012] by 12 mV to the right, as illustrated graphically in the middle part of Fig. 7. Likewise the $V'_L - I'_L$ curve of D_L is obtained by translating the $V_L - I_L$ curve of the leakage conductance G_L by 10.613 mV to the left, in view of the *negative sign*, as illustrated graphically in the lower part of Fig. 7. Here the $V_L - I_L$ curve is a straight line, with slope equal to G_L S, drawn through the

origin, representing Ohm's law $V_L = R_L I_L$, where $R_L = 1/G_L$, Ω .

Observe next that KCL implies $I = I'_{Na} + I'_K + I'_L$, and KVL implies $V = V'_{Na} = V'_K = V'_L$ in Fig. 6(b).

It follows that the V - I curve of the composite 1-port D in Fig. 6(a) can be obtained by aligning the current axis I'_{Na} , I'_K , and I'_L of the $V'_{Na} - I'_{Na}$ curve, $V'_K - I'_K$ curve, and $V'_L - I'_L$ curve, from Fig. 7 and adding their ordinates. This graphical construction was illustrated in Fig. 41 of [Chua et al., 2012], which we reproduce here as Fig. 8, for the reader's convenience. For future reference, we have presented an enlarged version of this V - I curve in Fig. 9(a) with the port voltage V as the horizontal axis. The same V - I curve is replotted

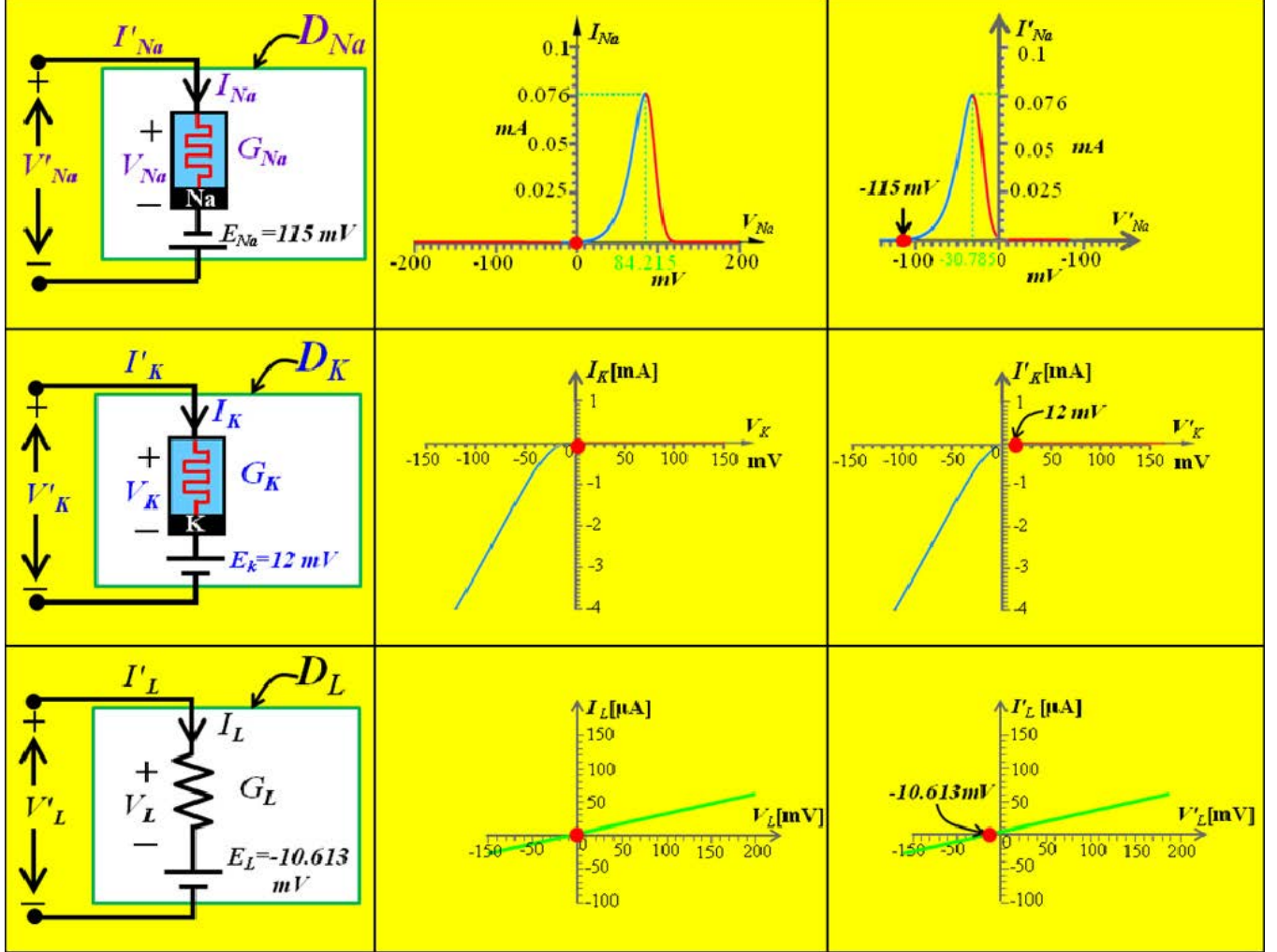


Fig. 7. Graphical illustration of effect of the battery in the DC voltage–current curve of the composite 1-port D_{Na} , D_K , and D_L .

in Fig. 9(b) with the port current I on the horizontal axis.

Finally, we are ready to derive the V_m – I_m curve of the composite 1-port D_{HH} in Fig. 5, which consists of a current source I_{ext} connected in parallel with the Hodgkin–Huxley DC circuit model in Fig. 6(a), whose V – I curve we have just derived in Fig. 9. Now since $V_m = V$, and $I_m = I - I_{\text{ext}}$, where $I = I'_{Na} + I'_K + I'_L$ in Fig. 6(b), it follows that the V_m – I_m curve can be obtained by simply translating the V – I curve in Fig. 9(a) along the current axis by $I_{\text{ext}} \mu\text{A}$ in a *downward* direction, assuming $I_{\text{ext}} > 0$. However, as will be shown in the latter sections, we are mainly interested in the case where $I_{\text{ext}} < 0$, which is equivalent to reversing the current source direction in Figs. 4 and 5. For

the case $I_{\text{ext}} < 0$, the V_m – I_m curve of the composite 1-port D_{HH} is obtained by translating the red V – I curve in Fig. 9(a) by $|I_{\text{ext}}| \mu\text{A}$ in an *upward* direction as illustrated by the blue V_m – I_m curve shown in Table 3.

Since $I_m = 0$ at equilibrium, the *equilibrium point Q* of the current-driven Hodgkin–Huxley circuit in Fig. 10 is located at the intersection between the blue V_m – I_m curve and the horizontal axis I_m , as illustrated in Table 3.

Table 3 also contains the *explicit* equations for calculating the resting potential V_∞ by numerical methods. The first equation is in fact the equation of the red DC V – I curve which we have just derived graphically and exhibited in Fig. 9(a). The second equation is the equation of the blue DC V_m – I_m

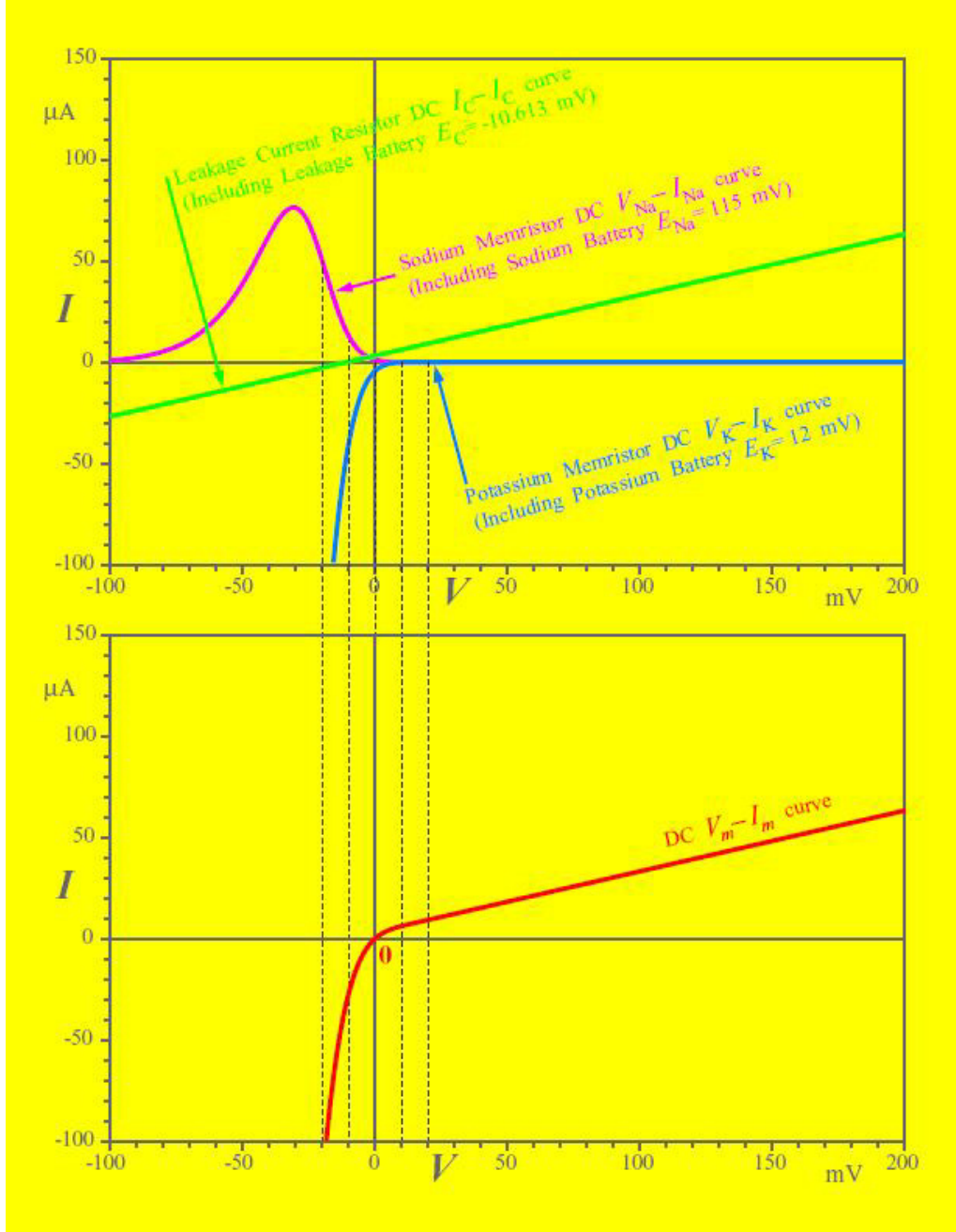


Fig. 8. The red DC $V_m - I_m$ curve at the bottom is obtained by adding the ordinate of the 12 mV right-shifted blue $V_K - I_K$ curve, the 115 mV left-shifted magenta $V_{Na} - I_{Na}$ curve, and the 10.613 mV left-shifted green $V_{G_L} - I_{G_L}$ curve.

curve in Table 3, defining $I_m(V_m)$ as a function of V_m with I_{ext} as parameter. The resting potential $V_m = V_\infty$ is obtained by solving for the root of the equation

$$I_m(V_m) = 0 \quad (5)$$

where $I_m(V_m)$ is specified explicitly by the second equation, along with the formulas defining the various nonlinear functions in Eq. (2). The

advantage of solving Eq. (5) numerically is that the resting potential V_∞ can be calculated to a high precision as illustrated in the inset table in Fig. 11, at 16 different values of I_{ext} , where some of these data will be used in Sec. 3 to illustrate the concept of edge of chaos and local activity.

On the other hand, the graphical approach elucidated in this section provides an invaluable intuition on the role played by the sodium ion-channel

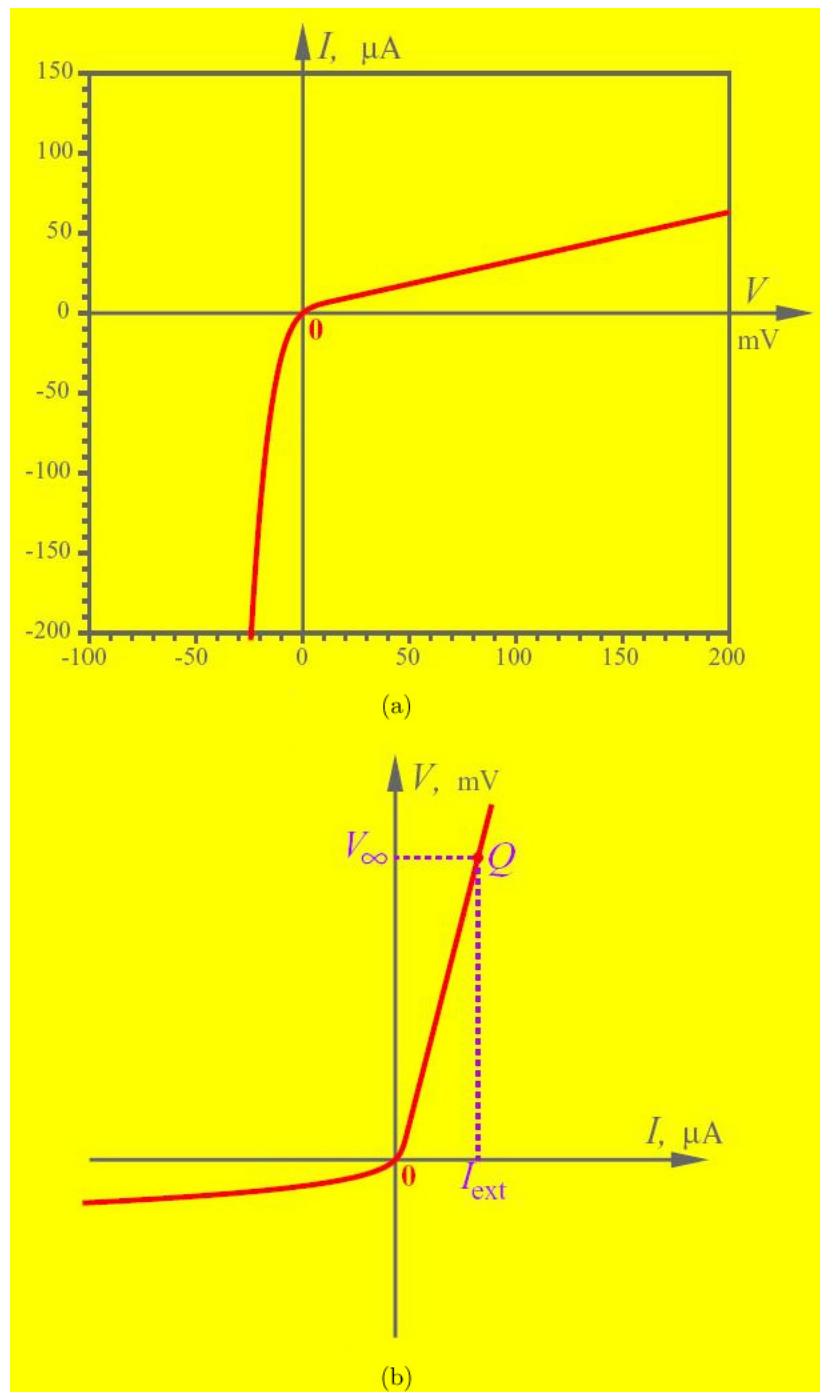
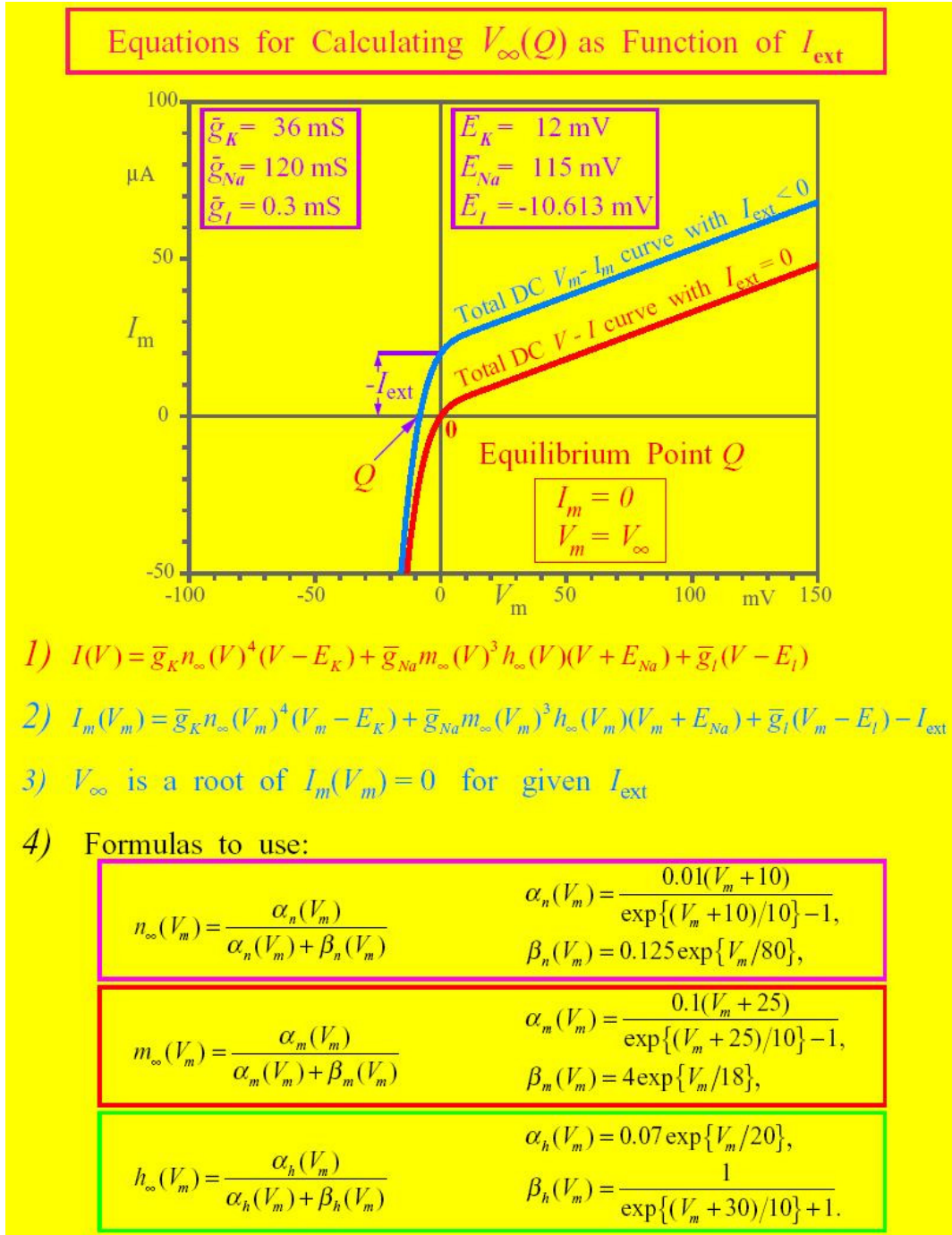
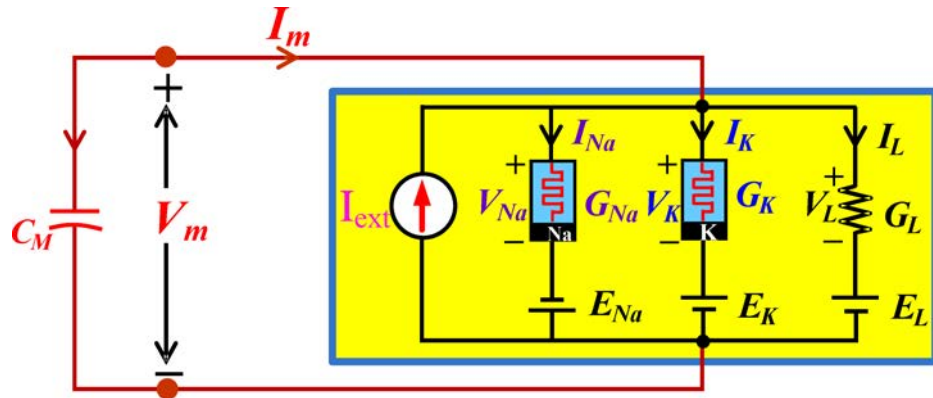
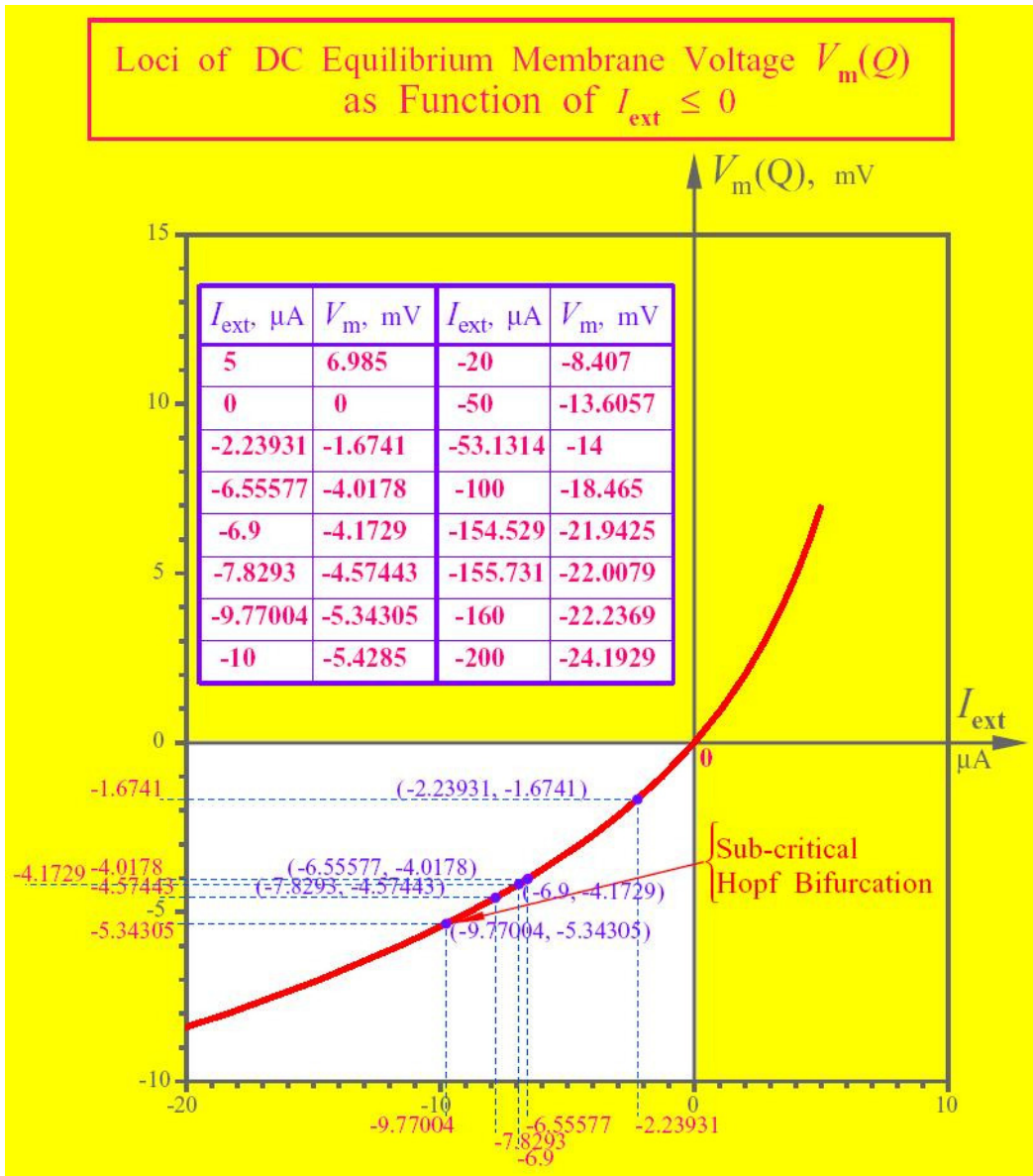


Fig. 9. V - I curve of the Hodgkin-Huxley DC circuit in Fig. 6(a). (a) V - I curve extracted from the bottom of Fig. 8. (b) The same V - I curve replotted with the port current I as the horizontal axis.

Table 3. Graphical method for deriving the resting potential $V_m = V_\infty$ for each value of $I_{\text{ext}} < 0$, and explicit equations for calculating V_∞ numerically.



Fig. 10. Hodgkin–Huxley axon circuit model driven by an external current source I_{ext} .Fig. 11. Relationship between the equilibrium voltage $V_m = V_\infty$ as a function of the DC excitation current I_{ext} .

memristor, and the potassium ion-channel memristor. Moreover, from the interpretation of the resting voltage V_∞ as the value of V_m where the blue V_m - I_m curve intersects the horizontal axis, and from the observation that this V_m - I_m curve is a strictly *monotonically-increasing function* of I_{ext} , we arrive at the following fundamental result:

Theorem 1. Unique Equilibrium Point Theorem. *For each DC excitation current I_{ext} , the Hodgkin-Huxley equations has a unique equilibrium point.*

2. Neurons are Locally Active

How does the leopard get its spots?
How does the zebra get its stripes?
How does the neuron get its spikes?

The answer to the above and, many other unrelated phenomena in nature is *local activity* [Chua, 2005].

The objective of this section is not to present a primer on local activity but rather to illustrate a simple mathematical technique for testing whether a particular dynamical system is locally active, and if it is, whether the local activity domain contains a subdomain called the *edge of chaos*. In the literature on *complexity* [Chua, 1998; Schrodinger, 1944; Turing, 1952; Smale, 1974; Prigogine, 1980; Haken, 1983], the mathematical and physical origins of many seemingly unrelated phenomena comes from the edge of chaos, which is typically a very small subset of the local activity domain. So small and yet so profound is the edge of chaos domain that we often dramatize its significance by dubbing it

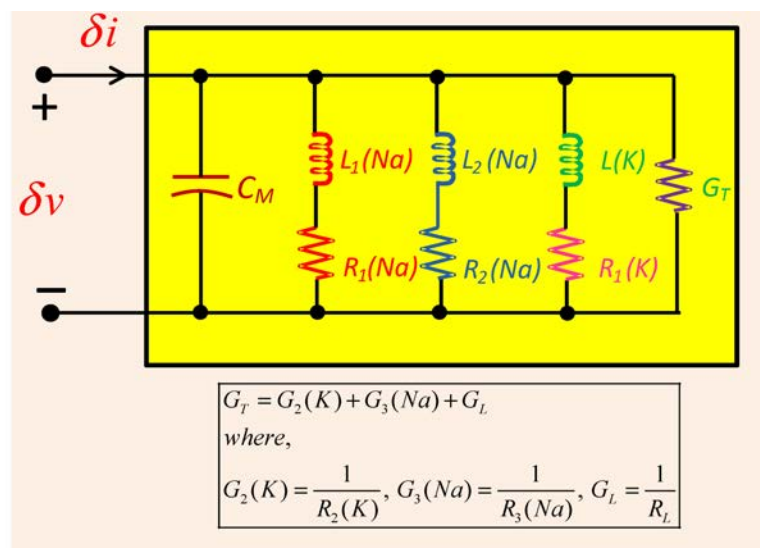
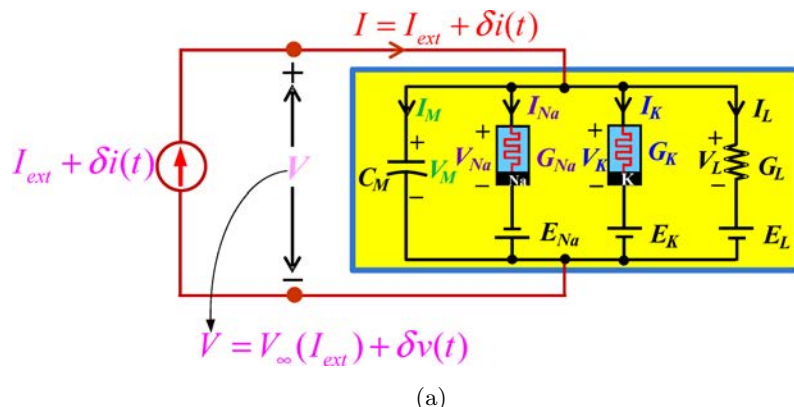


Fig. 12. (a) Hodgkin-Huxley axon circuit model and (b) its linearized small-signal equivalent HH circuit.

the *pearl of local activity*. Indeed, edge of chaos is the *elan vital* of life, and we will show that neurons are poised near this pearl of local activity.

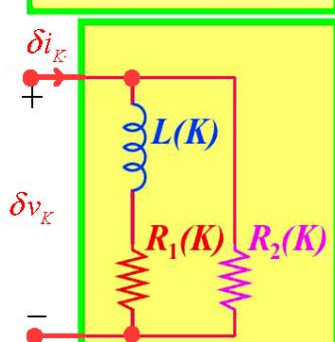
It is rather enigmatic that while all complexity phenomena, including the generation of spikes, require strongly nonlinear dynamics, yet the mathematical genesis of such *global* phenomena is strictly *local*. The theory of local activity and edge of chaos is based entirely on *linearized* differential equations about an equilibrium point [Chua, 1998]. In this paper, the equilibrium points are represented by the V - I curve of the Hodgkin–Huxley DC circuit depicted in Fig. 9(b), namely for each DC excitation current $I = I_{\text{ext}}$, there is a unique equilibrium point Q whose *resting voltage* is $V = V_{\infty}(I_{\text{ext}})$. Testing an equilibrium point Q for local activity in general, or

edge of chaos in particular, involves examining the *linearized* Hodgkin–Huxley equations about Q .

2.1. Linearized HH equations

For each equilibrium point Q corresponding to a DC excitation current I_{ext} , let us superimpose an *infinitesimally small* current signal $\delta i(t)$ and apply the composite signal $I_{\text{ext}} + \delta i(t)$ to the HH axon circuit model (Fig. 1), as shown in Fig. 12(a). Whether a system (in this case the Hodgkin–Huxley axon) is *locally active* at Q or not is completely determined by the response $\delta v(t)$ to an infinitesimally small *sinusoidal* testing signal $\delta i(t) = A \sin \omega t$, where A denotes the amplitude,⁴ and $\omega = 2\pi f$ denotes the angular frequency. It follows from elementary

Table 4. Explicit equations for $L(K)$, $R_1(K)$ and $R_2(K)$ as functions of $V_K = V_m - 12$ mV (reproduced from [Chua *et al.*, 2012]).

$L(K) = \frac{1}{c_n b_n}$	$c_n(V_K) = 4\bar{g}_K n(V_K)^3 V_K,$
	$b_n(V_K) = 0.01(n(V_K) - 1) \left(\frac{(V_K + E_K + 10)e^{(V_K + E_K + 10)/10}}{10(e^{(V_K + E_K + 10)/10} - 1)^2} - \frac{1}{(e^{(V_K + E_K + 10)/10} - 1)} \right)$ $- 0.125n(V_K) \frac{e^{(V_K + E_K)/80}}{80},$
$R_1(K) = \frac{\alpha_n + \beta_n}{c_n b_n}$	
	$\alpha_n(V_K) = \frac{0.01(V_K + E_K + 10)}{\exp\{(V_K + E_K + 10)/10\} - 1},$ $\beta_n(V_K) = 0.125 \exp\{(V_K + E_K)/80\},$
$R_2(K) = \frac{1}{d_K}$	
	$d_K = \bar{g}_K n(V_K)^4,$ $n(V_K) = \frac{\alpha_n(V_K)}{\alpha_n(V_K) + \beta_n(V_K)},$
$E_K = 12$ mV, $\bar{g}_K = 36$ mS	
Potassium Ion-Channel Memristor Small-Signal Equivalent circuit at Equilibrium Point $V_K(Q)$ 	

⁴Since the linearized HH circuit is described by a system of linear differential equations, A can assume any value without affecting the model's validity.

circuit theory [Chua *et al.*, 1987] that the response $\delta v(t)$ to any small-signal current excitation $\delta i(t)$ can be predicted analytically from a small-signal equivalent circuit whose elements are calculated explicitly from the Jacobian matrix of the associated nonlinear differential equations, evaluated at the equilibrium point Q . Such an equivalent circuit has been derived and presented in Fig. 44 of [Chua *et al.*, 2012], which we reproduced in Fig. 12(b) for convenience. Note that apart from a linear sodium conductance $G_3(Na)$ and a linear potassium conductance $G_2(K)$ which we have extracted from the small-signal sodium and potassium ion-channel memristors from Tables 5 and 7 of [Chua *et al.*, 2012], and combined with the leakage conductance G_L to form G_T in Fig. 12(b), the other circuit elements are associated with the sodium ion-channel memristor (via the symbol Na) and the potassium ion-channel memristor (via the symbol K) in the HH circuit model in Fig. 12(a). The values of the

circuit elements depend on the DC excitation current I_{ext} , and are calculated via explicit formulas given in Tables 5 and 7 of [Chua *et al.*, 2012], which we reproduced below as Tables 4 and 5, respectively.

A look-up-table listing the circuit element values of the sodium ion-channel memristor for 25 values of V_{Na} (leftmost column) or the equivalent values of $V_m = V_{Na} - 115$ mV (rightmost column) are given in Table 6. A similar look-up-table listing the circuit element values of the potassium ion-channel memristor for 13 values of V_K (leftmost column) or $V_m = V_K + 12$ mV (rightmost column) is given in Table 7.

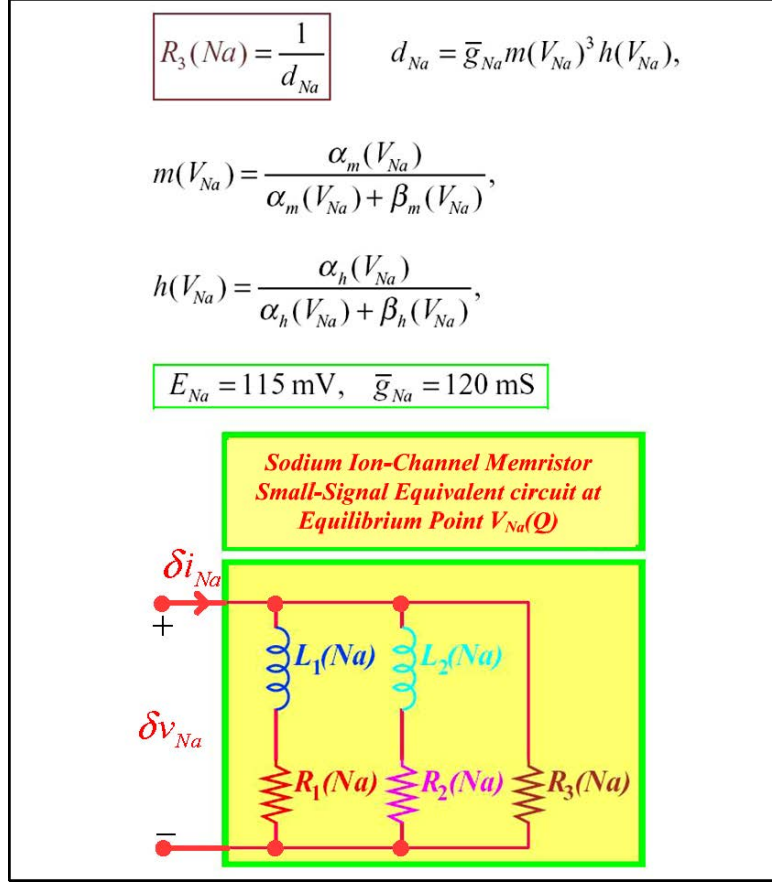
2.2. Complexity function of HH equations

Testing for local activity and edge of chaos of an equilibrium point Q of the HH axon circuit in Fig. 12(a) at any $I = I_{\text{ext}}$ requires that we examine

Table 5. Explicit equations for $L_1(Na)$, $R_1(Na)$, $L_2(Na)$, $R_2(Na)$ and $R_3(Na)$ as functions of V_{Na} . (Part 1).

$L_1(Na) = \frac{1}{c_m b_m}$	$c_m(V_{Na}) = 3\bar{g}_{Na}m(V_{Na})^2 h(V_{Na})V_{Na},$
$b_m(V_{Na}) = 0.1(m(V_{Na}) - 1) \left(\frac{(V_{Na} - E_{Na} + 25)e^{(V_{Na} - E_{Na} + 25)/10}}{10(e^{(V_{Na} - E_{Na} + 25)/10} - 1)^2} - \frac{1}{(e^{(V_{Na} - E_{Na} + 25)/10} - 1)} \right) - 4m(V_{Na}) \frac{e^{(V_{Na} - E_{Na})/18}}{18},$	
$L_2(Na) = \frac{1}{c_h b_h}$	$c_h(V_{Na}) = \bar{g}_{Na}m(V_{Na})^3 V_{Na},$
$b_h(V_{Na}) = \frac{h(V_{Na})e^{(V_{Na} - E_{Na} + 30)/10}}{10(e^{(V_{Na} - E_{Na} + 30)/10} + 1)^2} - 0.07(h(V_{Na}) - 1) \frac{e^{(V_{Na} - E_{Na})/20}}{20},$	
$R_1(Na) = \frac{\alpha_m + \beta_m}{c_m b_m}$	$\alpha_m(V_{Na}) = \frac{0.1(V_{Na} - E_{Na} + 25)}{\exp\{(V_{Na} - E_{Na} + 25)/10\} - 1},$
	$\beta_m(V_{Na}) = 4\exp\{(V_{Na} - E_{Na})/18\},$
$R_2(Na) = \frac{\alpha_h + \beta_h}{c_h b_h}$	$\alpha_h(V_{Na}) = 0.07\exp\{(V_{Na} - E_{Na})/20\},$
	$\beta_h(V_{Na}) = \frac{1}{\exp\{(V_{Na} - E_{Na} + 30)/10\} + 1},$

Table 5. Explicit equations for $L_1(Na)$, $R_1(Na)$, $L_2(Na)$, $R_2(Na)$ and $R_3(Na)$ as functions of $V_{Na} = V_m + 115$ mV (reproduced from [Chua *et al.*, 2012]). (Part 2).



the *complexity function*⁵ defined by

$$Z(s) = \frac{\hat{v}(s)}{\hat{i}(s)} \quad (6)$$

where $\hat{v}(s) = L(\delta v(t))$ and $\hat{i}(s) = L(\delta i(t))$ denote the Laplace transform of $\delta v(t)$ and $\delta i(t)$, respectively. The *complexity function* $Z(s)$ is called the *impedance* function in circuit theory [Chua *et al.*, 1987]. The impedance functions $Z(s)$ for the small-signal equivalent HH circuit in Fig. 12(b) has been derived in [Chua *et al.*, 2012] and is reproduced below:

$$Z(s; V_m) = \frac{a_3 s^3 + a_2 s^2 + a_1 s + a_0}{b_4 s^4 + b_3 s^3 + b_2 s^2 + b_1 s + b_0}. \quad (7)$$

The formulas for calculating the four coefficients $\{a_0, a_1, a_2, a_3\}$ in the numerator and the five coefficients $\{b_0, b_1, b_2, b_3, b_4\}$ in the denominator of $Z(s)$ are listed in the upper and lower parts of Table 8, respectively. Observe that these coefficients depend on the resting voltage $V_m = V_\infty$ at the DC excitation current I_{ext} depicted in Table 3 because the circuit elements in Fig. 12(b) are functions of V_m in Table 4, via the substitution $V_K = V_m - 12$ mV, and in Table 5, via the substitution $V_{Na} = V_m + 115$ mV. The coefficients of the impedance function $Z(s; V_m)$ in Eq. (7) calculated at 25 values of resting voltages $V_m = V_\infty$, and their corresponding values of V_{Na} and V_K , are listed in Table 9 for the readers' convenience.

⁵In general, the complexity function $C(s)$ for a single-input single-output system is defined by the ratio between the Laplace transform $\hat{y}(s)$ of the output variable $y(t)$ and the Laplace transform $\hat{u}(s)$ of the input variable $u(t)$; namely, $C(s) = \frac{L(y(t))}{L(u(t))} = \frac{\hat{y}(s)}{\hat{u}(s)}$. In Fig. 12(a), $u(t) = \delta i(t)$ and $y(t) = \delta v(t)$, respectively.

Table 6. Circuit element parameters of the small-signal circuit model of the Sodium Ion-Channel Memristor, where $V_{Na} = V_m + 115$ mV (reproduced from [Chua et al., 2012]).

V_{Na} , mV	L_1 , H	L_2 , H	R_1 , kΩ	R_2 , kΩ	R_3 , kΩ	V_m , mV
0	-1.96302e+018	5.27493e+016	-1.76825e+019	5.27503e+016	37.4882	-115
5	-3262.38	116.84	-27764.8	116.834	29.2198	-110
10	-953.116	45.5388	-7638.65	45.5304	22.782	-105
15	-370.987	23.6716	-2789.68	23.6612	17.7699	-100
20	-162.321	13.8475	-1140.6	13.8351	13.8682	-95
25	-75.6962	8.644	-494.806	8.62935	10.8316	-90
30	-36.7434	5.62315	-222.316	5.60588	8.46878	-85
35	-18.3342	3.76428	-102.113	3.74391	6.63098	-80
40	-9.33623	2.57354	-47.5768	2.5495	5.20238	-75
45	-4.8309	1.78808	-22.3788	1.7597	4.09294	-70
50	-2.53394	1.2584	-10.5988	1.22493	3.23282	-65
55	-1.34636	0.895416	-5.05109	0.85607	2.5681	-60
60	-0.725427	0.644425	-2.42697	0.598424	2.05768	-55
65	-0.397837	0.471397	-1.18248	0.417913	1.67112	-50
70	-0.223838	0.355284	-0.591241	0.293092	1.38757	-45
75	-0.131151	0.283677	-0.310081	0.210072	1.196	-40
80	-0.0821023	0.251228	-0.176868	0.159435	1.09783	-35
85	-0.057089	0.262424	-0.115677	0.135311	1.1153	-30
90	-4.62226e-015	0.35333	-9.16143e-015	0.140483	1.34759	-25
95	-0.0460213	0.602394	-0.0960704	0.177521	1.8947	-20
100	-0.058022	1.43207	-0.134633	0.308599	3.44212	-15
105	-0.0945203	4.65009	-0.257647	0.751734	8.03651	-10
110	-0.200267	20.4233	-0.669472	2.66268	24.2703	-5
115	-0.548625	118.978	-2.31715	13.9711	94.2579	0
120	-1.88833	884.521	-10.2687	105.43	457.571	5

2.3. Testing for local activity and edge of chaos

The principle of local activity and edge of chaos is a rather deep and powerful mathematical theory [Chua, 1998, 2005]. Here we extract and rephrase only the key aspects that are essential for this paper.

Local activity Theorem

It is *impossible* to generate a spike train unless the memristive Hodgkin–Huxley 1-port in Fig. 1 is *locally active* at some equilibrium point $V = V_\infty$

Edge of Chaos Theorem

A locally *asymptotically stable-equilibrium point* Q of the Hodgkin–Huxley Eq. (2) is poised on the *edge of chaos* if, and only if,⁶

$$\operatorname{Re} Z(i\omega; V_m(Q)) < 0 \quad (8)$$

at some frequency ω .

⁶ $Z(i\omega; V_m(Q))$ is the *impedance function* defined in Eq. (6) calculated at $s = 0 + i\omega$. $\operatorname{Re} Z$ denotes the *real part* of the complex number Z .

Table 7. Circuit element parameters of the small-signal circuit model of the Potassium Ion-Channel Memristor, where $V_K = V_m - 12$ mV (reproduced from [Chua *et al.*, 2012]).

V_K , mV	L , H	R_1 , k Ω	R_2 , k Ω	V_m , mV
-25	0.589568	0.130885	0.37588	-13
-20	1.23073	0.250377	0.714556	-8
-15	3.19081	0.604497	1.57402	-3
-10	10.9705	1.97344	4.06444	2
-5	59.4587	10.3713	12.3348	7
0	-9.50947e+015	-1.64175e+015	43.6909	12
5	-696.443	-121.215	178.012	17
10	-1454.43	-259.128	818.572	22
15	-4501.41	-830.778	4163.96	27
20	-17088.0	-3295.8	22997.4	32
25	-74195.6	-15048.3	135707.0	37

In the following sections, we will consider the important situation where $s = i\omega_p$ is a *pole* of the impedance function $Z(s)$ on the imaginary axis; namely, $|Z(i\omega)| \rightarrow \infty$ as $\omega \rightarrow \omega_p$. Since “infinities” are often difficult to handle mathematically, we will be working instead with the *inverse function*.

$$Y(s) \triangleq \frac{1}{Z(s)} \quad (9)$$

called the *admittance function* in circuit theory [Chua *et al.*, 1987] because

$$|Y(i\omega)| = \frac{1}{|Z(i\omega)|} \rightarrow 0 \quad \text{as } \omega \rightarrow \omega_p \quad (10)$$

thereby avoiding infinities. The following observation allows us to test Eq. (8) using $Y(s)$ instead of $Z(s)$.

Theorem 2. Equivalent Edge of Chaos Test

$$\operatorname{Re} Z(i\omega; V_m(Q)) < 0 \quad \text{at } \omega = \omega_p$$

if, and only if

$$\operatorname{Re} Y(i\omega; V_m(Q)) < 0 \quad \text{at } \omega = \omega_p$$

Proof. Let $Z = R + iX$

$$\begin{aligned} \operatorname{Re} Y &= \operatorname{Re} \left[\frac{1}{R + iX} \right] \\ &= \operatorname{Re} \left[\frac{(R - iX)}{(R + iX)(R - iX)} \right] \\ &= \frac{R}{R^2 + X^2} \\ &= \frac{\operatorname{Re} Z}{(\operatorname{Re} Z)^2 + (\operatorname{Im} Z)^2} \end{aligned} \quad (11)$$

where $\operatorname{Im} Z$ denotes the imaginary part of Z .

It follows from Eq. (11) that

$$\operatorname{Re} Y < 0 \Leftrightarrow \operatorname{Re} Z < 0. \quad (12)$$

■

Theorem 3. RHP Pole of $Z(s)$ implies Local Activity. *If the impedance function $Z(s; V_m(Q))$ of the Hodgkin–Huxley equation has a pole $s = s_p$, in the open right-half-plane, i.e. $\operatorname{Re} s_p > 0$, then the memristive HH axon model is locally active at Q .*

Proof. See [Chua, 2005]. ■

Theorem 4. Edge of Chaos implies Local Activity. *If the Hodgkin–Huxley equation is poised on an edge of chaos at an equilibrium point Q , then it is locally active at Q .*

Proof. This is a deep mathematical result. For a sketch of the proof, see [Chua, 2005]. ■

Remark. Theorems 3 and 4 provide two sufficient (but not necessary) conditions for the Hodgkin–Huxley axon model to be *locally active*. The hypothesis of Theorem 4 is much more stringent than that of Theorem 3 because in addition to satisfying Eq. (8), the equilibrium point Q must be *locally asymptotically stable*, thereby requiring that all poles “ s_p ” of $Z(s)$ at Q must be restricted to the open left-half plane; namely $\operatorname{Re} s_p < 0$. Since it is mathematically difficult to satisfy both conditions simultaneously at an equilibrium point $Q(V_m)$ at V_m , the subset of resting potentials $V_m \in \mathbb{R}$ that gives rise to an *edge of chaos* situation is rare indeed. This Goldilocks scenario is precisely where the neuron fits!

Table 8. Formulas for calculating coefficients of the small-signal impedance function $Z(s; V_m)$ of the Hodgkin–Huxley axon.

$$\begin{aligned}
 a_0 &= R_1(Na)R_2(Na)R_3(Na)R_1(K)R_2(K) \\
 a_1 &= R_3(Na)R_2(K)[L(K)R_1(Na)R_2(Na) + R_1(K)\{R_1(Na)L_2(Na) + R_2(Na)L_1(Na)\}] \\
 a_2 &= R_3(Na)R_2(K)[R_1(K)L_1(Na)L_2(Na) + L(K)\{R_1(Na)L_2(Na) + R_2(Na)L_1(Na)\}] \\
 a_3 &= R_3(Na)R_2(K)L_1(Na)L_2(Na)L(K)
 \end{aligned}$$

$$\begin{aligned}
 b_0 &= R_1(K)R_2(K)[R_1(Na)R_2(Na) + R_2(Na)R_3(Na) + R_3(Na)R_1(Na)] + R_1(Na)R_2(Na)R_3(Na)[R_1(K) + R_2(K)] \\
 &\quad + R_1(Na)R_2(Na)R_3(Na)R_1(K)R_2(K)G_L
 \end{aligned}$$

$$\begin{aligned}
 b_1 &= R_3(Na)[R_1(K)L_2(Na)R_1(Na) + R_2(Na)\{L(K)R_1(Na) + R_1(K)L_1(Na)\} + R_2(K)\{L_1(Na)R_2(Na) + L_2(Na)R_1(Na)\}] \\
 &\quad + R_3(Na)R_2(K)[[L(K)R_1(Na)R_2(Na) + R_1(K)\{L_1(Na)R_2(Na) + L_2(Na)R_1(Na)\}]G_L + R_1(K)R_1(Na)R_2(Na)C_M] \\
 &\quad + L(K)R_2(K)[R_1(Na)R_2(Na) + R_2(Na)R_3(Na) + R_1(Na)R_3(Na)] \\
 &\quad + R_1(K)R_2(K)[L_1(Na)\{R_2(Na) + R_3(Na)\} + L_2(Na)\{R_1(Na) + R_3(Na)\}]
 \end{aligned}$$

$$\begin{aligned}
 b_2 &= R_2(K)R_3(Na)\left[\left\{(R_1(K)L_1(Na)L_2(Na) + L(K)\{R_1(Na)L_2(Na) + R_2(Na)L_1(Na)\})\right\]G_L\right] \\
 &\quad + \{L(K)R_1(Na)R_2(Na) + R_1(K)[R_1(Na)L_2(Na) + R_2(Na)L_1(Na)]\}C_M\right] \\
 &\quad + R_3(Na)[L(K)L_2(Na)R_1(Na) + L_1(Na)\{L(K)R_2(Na) + L_2(Na)[R_1(K) + R_2(K)]\}] \\
 &\quad + R_2(K)[L_1(Na)L_2(Na)R_1(K) + L(K)\{L_1(Na)[R_2(Na) + R_3(Na)] + L_2(Na)[R_1(Na) + R_3(Na)]\}]
 \end{aligned}$$

$$\begin{aligned}
 b_3 &= L_1(Na)L_2(Na)L(K)[R_2(K) + R_3(Na)] \\
 &\quad + R_3(Na)R_2(K)[L_1(Na)L_2(Na)L(K)G_L + [R_1(K)L_1(Na)L_2(Na) + L(K)\{R_1(Na)L_2(Na) + R_2(Na)L_1(Na)\}]C_M]
 \end{aligned}$$

$$b_4 = R_3(Na)R_2(K)L_1(Na)L_2(Na)L(K)C_M$$

Table 9. Coefficients of the impedance function $Z(s; V_m)$ of the small-signal HH axon circuit model in Fig. 12, $V_{Na} = V_m + 115$ mV, $V_K = V_m - 12$ mV (reproduced from [Chua *et al.*, 2012]).

V_m mV	V_{Na} mV	V_K mV	a_0	a_1	a_2	a_3	b_0	b_1	b_2	b_3	b_4
-115	0	-127	-2.21397e+021	-4.51022e+021	-2.52388e+021	-2.27632e+020	-9.39405e+028	-1.73270e+029	-8.90357e+028	-9.92769e+027	-2.27624e+026
-110	5	-122	-278935.0	-582102.0	-334937.0	-31771.1	-1.19439e+007	-2.23116e+007	-1.16913e+007	-1.35545e+006	-31771.1
-105	10	-117	-21920.5	-46943.0	-27803.5	-2780.93	-947567	-1.79352e+006	-958986	-115863	-2780.93
-100	15	-112	-3056.74	-6730.61	-4108.47	-434.524	-133443	-256061	-139810	-17645.6	-434.524
-95	20	-107	-538.583	-1222.02	-769.855	-86.3627	-23752.3	-46236.8	-25800.5	-3410.68	-86.3627
-90	25	-102	-107.829	-252.746	-164.598	-19.6514	-4805.32	-9496.62	-5421	-752.749	-19.6514
-85	30	-97	-23.4071	-56.8422	-38.3404	-4.88972	-1054.22	-2117.2	-1237.78	-181.103	-4.88972
-80	35	-92	-5.37599	-13.5709	-9.50288	-1.29985	-244.693	-500.011	-299.812	-46.3765	-1.29985
-75	40	-87	-1.2884	-3.39413	-2.47454	-0.364626	-59.2439	-123.385	-76.0114	-12.4759	-0.364626
-70	45	-82	-0.319688	-0.882974	-0.672718	-0.107289	-14.8381	-31.5704	-20.0262	-3.50139	-0.107289
-65	50	-77	-0.081837	-0.2383	-0.190636	-0.0330744	-3.82762	-8.34741	-5.46748	-1.02273	-0.0330744
-60	55	-72	-0.0216281	-0.0668411	-0.0565012	-0.0107209	-1.01622	-2.28226	-1.54903	-0.311552	-0.0107209
-55	60	-67	-0.00594051	-0.019643	-0.0176925	-0.00369201	-0.27889	-0.649225	-0.458621	-0.0998079	-0.00369201
-50	65	-62	-0.00172521	-0.00616328	-0.00598059	-0.00138018	-0.0801679	-0.195122	-0.144185	-0.0342671	-0.00138018
-45	70	-57	-0.000549461	-0.00214562	-0.00227491	-0.000583543	-0.0248579	-0.063929	-0.0496482	-0.0130913	-0.000583543
-40	75	-52	-0.000205692	-0.000890108	-0.0010491	-0.000300055	-0.00879871	-0.0241663	-0.0197426	-0.00595678	-0.000300055
-35	80	-47	-0.000101766	-0.000495834	-0.000662425	-0.000210834	-0.00391185	-0.0115446	-0.00978993	-0.00360537	-0.000210834
-30	85	-42	-7.90744e-005	-0.00044166	-0.000682162	-0.000238595	-0.00251549	-0.00792547	-0.0065717	-0.00339574	-0.000238595
-25	90	-37	5.68656e-008	3.71348e-007	6.7432e-007	2.51655e-007	-0.00148979	-0.00374834	-0.000379861	-0.00408231	-0.000358966
-20	95	-32	-0.000436575	-0.00339898	-0.00732524	-0.00277707	-0.00669613	-0.0224851	-0.00239072	-0.0243055	-0.00277707
-15	100	-27	-0.00460075	-0.0432751	-0.110339	-0.039883	-0.0418533	-0.156755	0.0991905	-0.266038	-0.039883
-10	105	-22	2.26638e-013	2.565e-012	7.59062e-012	2.45067e-012	-0.922293	-6.04349	-2.09298	1.77197e-013	3.40403e-014
-5	110	-17	-20.0658	-263.077	-868.204	-236.712	-50.9518	-388.666	-271.096	-1159	-236.712
0	115	-12	-9803.38	-139319.0	-488150.0	-107898.0	-11428.9	-121821	-290745	-561182	-107898
5	120	-7	1.89256e+007	-269704068	-950376189	-165764351	1.03313e+007	-1.43158e+008	-5.97293e+008	1.02176e+009	-1.65764e+008

3. Mapping the Zeros of Admittance Function $Y(s; V_m)$

Let us recast the Hodgkin–Huxley equations (2), with external current excitation I_{ext} , in the following generic form:

$$\begin{aligned} \frac{dV}{dt} &= F_V(V, n, m, h; I_{\text{ext}}) \\ \frac{dn}{dt} &= F_n(V, n, m, h; I_{\text{ext}}) \\ \frac{dm}{dt} &= F_m(V, n, m, h; I_{\text{ext}}) \\ \frac{dh}{dt} &= F_h(V, n, m, h; I_{\text{ext}}) \end{aligned} \quad (13)$$

Let

$$V = V_m(Q(I_{\text{ext}})) = V_m(I_{\text{ext}}) \quad (14)$$

denote the unique equilibrium voltage $V_m(I_{\text{ext}})$ at Q calculated from the equilibrium equation $I_m(V_m) = 0$ from Table 3. Let the 4×4 Jacobian matrix

$J_{\text{HH}} = (V, n, m, h; I_{\text{ext}})$ be denoted by

$$J_{\text{HH}} = \begin{bmatrix} \frac{\partial F_V}{\partial V} & \frac{\partial F_V}{\partial n} & \frac{\partial F_V}{\partial m} & \frac{\partial F_V}{\partial h} \\ \frac{\partial F_n}{\partial V} & \frac{\partial F_n}{\partial n} & \frac{\partial F_n}{\partial m} & \frac{\partial F_n}{\partial h} \\ \frac{\partial F_m}{\partial V} & \frac{\partial F_m}{\partial n} & \frac{\partial F_m}{\partial m} & \frac{\partial F_m}{\partial h} \\ \frac{\partial F_h}{\partial V} & \frac{\partial F_h}{\partial n} & \frac{\partial F_h}{\partial m} & \frac{\partial F_h}{\partial h} \end{bmatrix} \quad (15)$$

The local stability of the equilibrium point Q of the HH-equations (13), for any $I_{\text{ext}} \in \mathbb{R}$, is determined by the four eigenvalues of the Jacobian matrix $J_{\text{HH}} = (V, n, m, h; I_{\text{ext}})$. Since the formulas defining $F_V(\cdot)$, $F_n(\cdot)$, $F_m(\cdot)$, and $F_h(\cdot)$ in Eq. (13) are quite involved, the 16 elements of the Jacobian matrix $J_{\text{HH}} = (V, n, m, h; I_{\text{ext}})$ are rather messy and are best stored as computer codes. The four eigenvalues of $J_{\text{HH}} = (V, n, m, h; I_{\text{ext}})$ must be calculated numerically for each I_{ext} . This enormous computation task was carried out [Hassard, 1978]

Table 10. Table of eigenvalues of $J_{\text{HH}} = (V, n, m, h; I_{\text{ext}})$.

(a) From Jacobian matrix of the HH equation (reproduced from [Hassard, 1978]).

I	v_*	m_*	n_*	h_*	λ_1, λ_2	λ_3	λ_4
-5	-6.98	0.023	0.218	0.804	-0.251±0.106i	-0.124	-6.08
0	0	0.053	0.318	0.596	-0.203±0.383i	-0.121	-4.68
5	-3.27	0.077	0.369	0.479	-0.097±0.521i	-0.129	-4.60
9	-5.05	0.094	0.397	0.416	-0.015±0.578i	-0.137	-4.73
9.780	-5.35	0.097	0.402	0.406	0±0.586i	-0.138	-4.76
10	-5.43	0.098	0.403	0.403	0.004±0.588i	-0.139	-4.77
20	-8.41	0.135	0.450	0.308	0.155±0.642i	-0.158	-5.28
50	-13.61	0.222	0.530	0.179	0.320±0.715i	-0.204	-6.66
100	-18.46	0.331	0.599	0.104	0.229±0.903i	-0.262	-8.24
150	-21.69	0.413	0.640	0.072	0.020±1.053i	-0.307	-9.33
154.5	-21.94	0.420	0.643	0.070	0±1.063i	-0.311	-9.41
160	-22.24	0.427	0.647	0.068	-0.025±1.075i	-0.315	-9.51
200	-24.19	0.479	0.670	0.055	-0.203±1.138i	-0.346	-10.17
300	-28.12	0.581	0.711	0.036	-0.606±1.172i	-0.412	-11.52

(b) From zeros of the Admittance matrix $Y(i\omega; V_m)$ (derived in [Chua et al., 2012]).

I_{ext} , μA	V_{∞} , mV	m_{∞}	n_{∞}	h_{∞}	λ_1, λ_2	λ_3	λ_4
5	6.98582	0.0225637	0.218026	0.80425	-0.250862 ± i 0.105924	-0.124313	-6.08672
0	0	0.0529325	0.317677	0.596121	-0.202539 ± i 0.383073	-0.12066	-4.6753
-5	-3.26737	0.0772018	0.368711	0.479357	-0.0969946 ± i 0.520832	-0.129215	-4.59741
-9	-5.04838	0.0941408	0.39704	0.416475	-0.0146833 ± i 0.578284	-0.136964	-4.73056
-9.77003183	-5.34305	0.0972275	0.401739	0.406324	± i 0.586124	-0.13846	-4.76383
-10	-5.42865	0.09814	0.403105	0.403392	0.00430308 ± i 0.588311	-0.138907	-4.77407
-20	-8.40711	0.134578	0.450474	0.307655	0.155147 ± i 0.641558	-0.157593	-5.27624
-50	-13.6057	0.222068	0.530413	0.179059	0.320389 ± i 0.714698	-0.204061	-6.65824
-100	-18.465	0.330717	0.598985	0.103886	0.22912 ± i 0.902532	-0.261768	-8.23881
-150	-21.6929	0.41313	0.640222	0.0723248	0.020315 ± i 1.05273	-0.307146	-9.32765
-154.529003	-21.9425	0.419693	0.643257	0.0703507	± i 1.06295	-0.310876	-9.41197
-160	-22.2369	0.427455	0.646807	0.0680973	-0.0246114 ± i 1.07458	-0.315315	-9.51143
-200	-24.1929	0.479295	0.669594	0.0550009	-0.203417 ± i 1.13776	-0.345837	-10.173
-300	-28.1193	0.581226	0.711171	0.0364869	-0.605894 ± i 1.17212	-0.411787	-11.522

before the advent of super computers. We reproduce a table of eigenvalues of $J_{\text{HH}} = (V, n, m, h; I_{\text{ext}})$ from Table 1 on page 404 of [Hassard, 1978] in Table 10(a). Our next theorem shows that this same table can be calculated by solving for the roots of a polynomial equation.

Theorem 5. Eigenvalues of J_{HH} are Zeros of $Y(s; I_{\text{ext}})$. The four eigenvalues of the Jacobian matrix $J_{\text{HH}} = (V, n, m, h; I_{\text{ext}})$ are identical to the four zeros of the numerator polynomial of the scalar admittance function

$$Y(s; I_{\text{ext}}) = \frac{b_4 s^4 + b_3 s^3 + b_2 s^2 + b_1 s + b_0}{a_3 s^3 + a_2 s^2 + a_1 s + a_0} \quad (16)$$

Proof. It follows from the theory developed in [Chua et al., 1987] that the eigenvalues of $J_{\text{HH}} = (V, n, m, h; I_{\text{ext}})$ are identical to the poles of the impedance function $Z(s; V_m(I_{\text{ext}}))$ defined in Eq. (7). Since the admittance function $Y(s; V_m(I_{\text{ext}}))$ in Eq. (9) is the inverse of $Z(s; V_m(I_{\text{ext}}))$, it follows that the eigenvalues of $J_{\text{HH}} = (V, n, m, h; I_{\text{ext}})$ are the zeros of $Y(s; V_m(I_{\text{ext}}))$. ■

Theorem 5 implies that the four eigenvalues of $J_{\text{HH}} = (V, n, m, h; I_{\text{ext}})$ can be found by calculating the four roots of the polynomial equation

$$b_4 s^4 + b_3 s^3 + b_2 s^2 + b_1 s + b_0 = 0 \quad (17)$$

This is a much simpler computation task and we have calculated the four roots of Eq. (17) for the same set of 14 excitation currents $I_{\text{ext}} = -I$ listed in the leftmost column⁷ of Hassard's Table 1. They are listed in Table 10(b). A comparison of these two tables shows that their corresponding eigenvalues are remarkably close to each other, in spite of the fundamental differences of methodology. Our calculations, which were carried out on a desktop PC, circa 2008, are accurate up to six decimal digits. We believe our more accurate calculated values are due to our considerably simpler numerical algorithms for solving the roots of the fourth degree polynomial Eq. (17) than those for solving the eigenvalues of the 4×4 matrix J_{HH} .

It is much more illuminating to exhibit the zeros $z_k = \text{Re } z_k + i \text{Im } z_k$, $k = 1, 2, 3, 4$, of the

admittance function $Y(s; V_m(I_{\text{ext}}))$ from Table 10 as a loci in the $\text{Im } z_k$ versus $\text{Re } z_k$ plane, with either V_m , or I_{ext} as a parameter, as shown in Fig. 13. Since the complex zeros of $Y(s; V_m(I_{\text{ext}}))$ occur in complex conjugate pairs [Chua *et al.*, 1987], this loci exhibits a mirror-symmetry with respect to the real axis. Consequently, we have printed both parameter values (I_{ext}, V_m) at corresponding points on the loci. Since the points chosen in the loci have special significance in the next section, we have enlarged the region of interest in two mirrored insets. Since each zero z_K of $Y(s; V_m(I_{\text{ext}}))$ is equal to an eigenvalue λ_k of the Jacobian matrix $J_{\text{HH}} = (V, n, m, h; I_{\text{ext}})$ of the HH equation (Theorem 5), Fig. 13 represents also the loci of the four eigenvalues $\lambda_k = z_k$ of J_{HH} .

An examination of the loci in Fig. 13 yields the following numerical results:

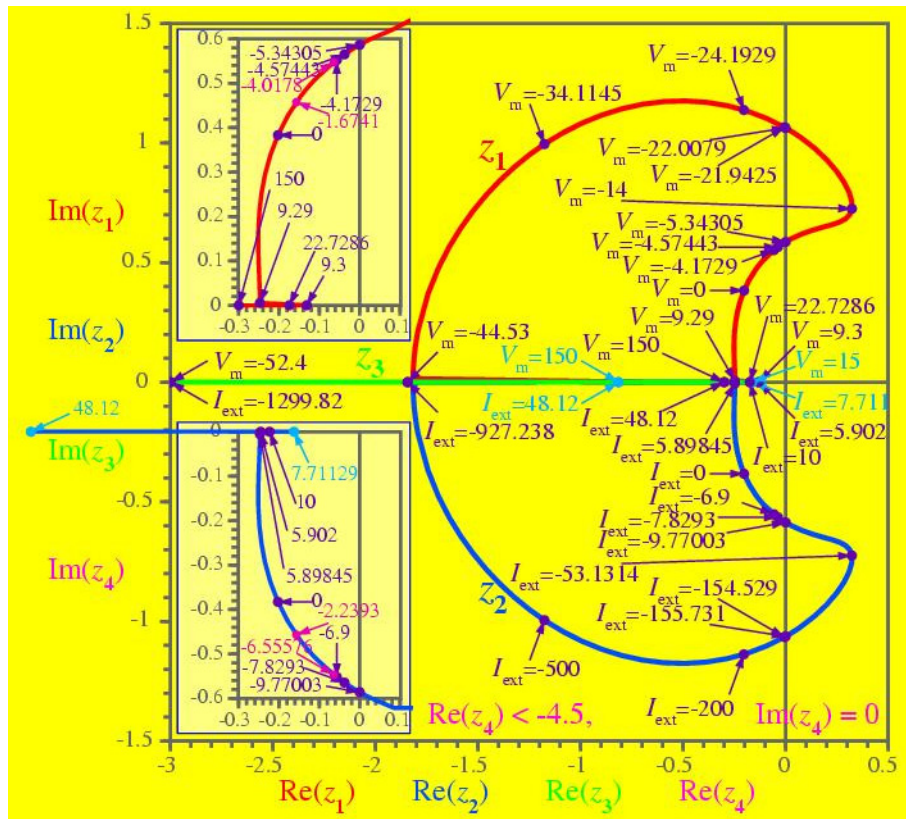


Fig. 13. Loci of the four zeros z_1, z_2, z_3 , and z_4 of the admittance function $Y(s; V_m(I_{\text{ext}}))$, with V_m indicated in the upper half of the loci, and with I_{ext} indicated in the lower half of the symmetrical loci. At $V_m = 5.343046848$ mV and $I_{\text{ext}} = 9.77003187256615$ μ A, the eigenvalues of the Jacobian matrix J_{HH} in Eq. (15) are given by: $\lambda_1 = 0.586124271589i$; $\lambda_2 = -0.586124271589i$; $\lambda_3 = -0.138460448475$; $\lambda_4 = -4.763834175202$.

⁷The symbol I in the leftmost column of Hassard's Table 1 is defined as entering the bottom terminal of the HH axon model in Fig. 1, and is therefore opposite to that of I_{ext} adopted in Fig. 10 of this paper.

The impedance function $Z(s; V_m(I_{\text{ext}}))$ of the memristive Hodgkin–Huxley axon circuit model has a pair of *poles* in the open right-half-plane over the parameter range.

$$\begin{aligned} -154.529 \mu\text{A} &< I_{\text{ext}} < -9.77003 \mu\text{A} \\ -21.9425 \text{ mV} &< V_m < -5.34305 \text{ mV} \end{aligned} \quad (18)$$

henceforth called the “HH RHP Pole domain.”

Theorem 6. *The memristor Hodgkin–Huxley axon circuit model is locally active in the HH RHP Pole domain.*

Proof. Follow from Theorem 3. ■

4. Mapping the Landscape of $\text{Re } Y(i\omega; V_m(I_{\text{ext}}))$

In the previous section, we had to explore the entire complex frequency plane $s = \text{Re } s + i \text{Im } s$

because any s is a possible root of the polynomial Eq. (17). In the case of the Hodgkin–Huxley equations, this task was relatively easy because the zeros of $Y(s; V_m(I_{\text{ext}}))$ in the open right-half plane (RHP) are located along a contiguous “nose” of the red loci located on the right of the vertical (imaginary) axis, bounded by the HH RHP Pole domain defined in Eq. (18).

Our next challenge is to identify the *edge of chaos* domain in the LHP plane⁸ $\text{Re } s < 0$ where $\text{Re } Z(i\omega; V_m(I_{\text{ext}})) < 0$ as prescribed by Eq. (8).

For future reference, let us reproduce the formulas of the impedance function $Z(s; V_m)$ and the admittance function $Y(s; V_m)$ from [Chua et al., 2012] for $s = i\omega$ as follows:

$$Z(i\omega; V_m) = \text{Re } Z(i\omega; V_m) + i \text{Im } Z(i\omega; V_m) \quad (19)$$

where

$$\begin{aligned} \text{Re } Z(i\omega; V_m) &= \frac{(a_0 - a_2\omega^2)(b_0 - b_2\omega^2 + b_4\omega^4) + (a_1 - a_3\omega^2)(b_1 - b_3\omega^2)\omega^2}{(b_0 - b_2\omega^2 + b_4\omega^4)^2 + (b_1 - b_3\omega^2)^2\omega^2} \\ &= \frac{(a_3b_3 - a_2b_4)\omega^6 + (a_0b_4 - a_1b_3 + a_2b_2 - a_3b_1)\omega^4 + (a_1b_1 - a_0b_2 - a_2b_0)\omega^2 + a_0b_0}{b_4^2\omega^8 + (b_3^2 - 2b_2b_4)\omega^6 + (b_2^2 + 2b_0b_4 - 2b_1b_3)\omega^4 + (b_1^2 - 2b_0b_2)\omega^2 + b_0^2} \end{aligned} \quad (20a)$$

$$\begin{aligned} \text{Im } Z(i\omega; V_m) &= \frac{[(a_1 - a_3\omega^2)(b_0 - b_2\omega^2 + b_4\omega^4) - (a_0 - a_2\omega^2)(b_1 - b_3\omega^2)]\omega}{(b_0 - b_2\omega^2 + b_4\omega^4)^2 + (b_1 - b_3\omega^2)^2\omega^2} \\ &= \frac{-a_3b_4\omega^7 + (a_1b_4 - a_2b_3 + a_3b_2)\omega^5 + (a_0b_3 - a_1b_2 + a_2b_1 - a_3b_0)\omega^3 - (a_0b_1 - a_1b_0)\omega}{b_4^2\omega^8 + (b_3^2 - 2b_2b_4)\omega^6 + (b_2^2 + 2b_0b_4 - 2b_1b_3)\omega^4 + (b_1^2 - 2b_0b_2)\omega^2 + b_0^2} \end{aligned} \quad (20b)$$

Similarly,

$$Y(i\omega; V_m) = \text{Re } Y(i\omega; V_m) + i \text{Im } Y(i\omega; V_m) \quad (21)$$

where

$$\begin{aligned} \text{Re } Y(i\omega; V_m) &= \frac{(a_0 - a_2\omega^2)(b_0 - b_2\omega^2 + b_4\omega^4) + (a_1 - a_3\omega^2)(b_1 - b_3\omega^2)\omega^2}{(a_0 - a_2\omega^2)^2 + (a_1 - a_3\omega^2)^2\omega^2} \\ &= \frac{(a_3b_3 - a_2b_4)\omega^6 + (a_0b_4 - a_1b_3 + a_2b_2 - a_3b_1)\omega^4 + (a_1b_1 - a_0b_2 - a_2b_0)\omega^2 + a_0b_0}{a_3^2\omega^6 + (a_2^2 - 2a_1a_3)\omega^4 + (a_1^2 - 2a_0a_2)\omega^2 + a_0^2} \end{aligned} \quad (22a)$$

⁸An equilibrium point of the HH equation is asymptotically stable, if, and only if, $\text{Re } \lambda_k = \text{Re } z_k < 0$, where λ_K is an eigenvalue of $J_{HH}(V, n, m, h; I_{\text{ext}})$, and z_k is a zero of the admittance function $Y(s; V_m(I_{\text{ext}}))$ [Chua, 1978].

$$\text{Im } Y(i\omega; V_m)$$

$$\begin{aligned}
 &= -\frac{[(a_1 - a_3\omega^2)(b_0 - b_2\omega^2 + b_4\omega^4) - (a_0 - a_2\omega^2)(b_1 - b_3\omega^2)]\omega}{(a_0 - a_2\omega^2)^2 + (a_1 - a_3\omega^2)^2\omega^2} \\
 &= \frac{a_3b_4\omega^7 - (a_1b_4 - a_2b_3 + a_3b_2)\omega^5 - (a_0b_3 - a_1b_2 + a_2b_1 - a_3b_0)\omega^3 + (a_0b_1 - a_1b_0)\omega}{a_3^2\omega^6 + (a_2^2 - 2a_1a_3)\omega^4 + (a_1^2 - 2a_0a_2)\omega^2 + a_0^2}
 \end{aligned} \tag{22b}$$

Here the coefficients of a_i and b_i are calculated from explicit formulas given in Table 8.

It follows from Theorem 2 that in so far as mapping the edge of chaos domain is concerned, it suffices for us to focus on $\text{Re } Y(i\omega; V_m)$, where $V_m = V_m(I_{\text{ext}})$ is given in Table 3. The landscape depicting $\text{Re } Y(i\omega; V_m)$ as calculated from Eq. (22a) is shown in Fig. 14. The two symmetric contours denote the loci of all $(\omega; V_m)$ where $\text{Re } Y(i\omega; V_m) = 0$. The corresponding surface representing $\text{Im } Y(i\omega; V_m)$ as calculated from Eq. (22b) is shown in Fig. 15.

Since we will often be interested in the landscape of $\text{Re } Y(i\omega; I_{\text{ext}})$ and $\text{Im } Y(i\omega; I_{\text{ext}})$ as well, the corresponding surface is shown in Figs. 16 and 17, respectively.

A detailed numerical analysis of the landscapes of $\text{Re } Y(i\omega; V_m)$ and $\text{Re } Y(i\omega; I_{\text{ext}})$ reveals that all points (in red) where the respective surfaces are below ground zero are confined inside the respective closed contours, as shown in Fig. 18.

For a clearer visualization of the surfaces depicted in Figs. 14 and 15, several cross-sections are exhibited in Figs. 19 and 20, respectively, where

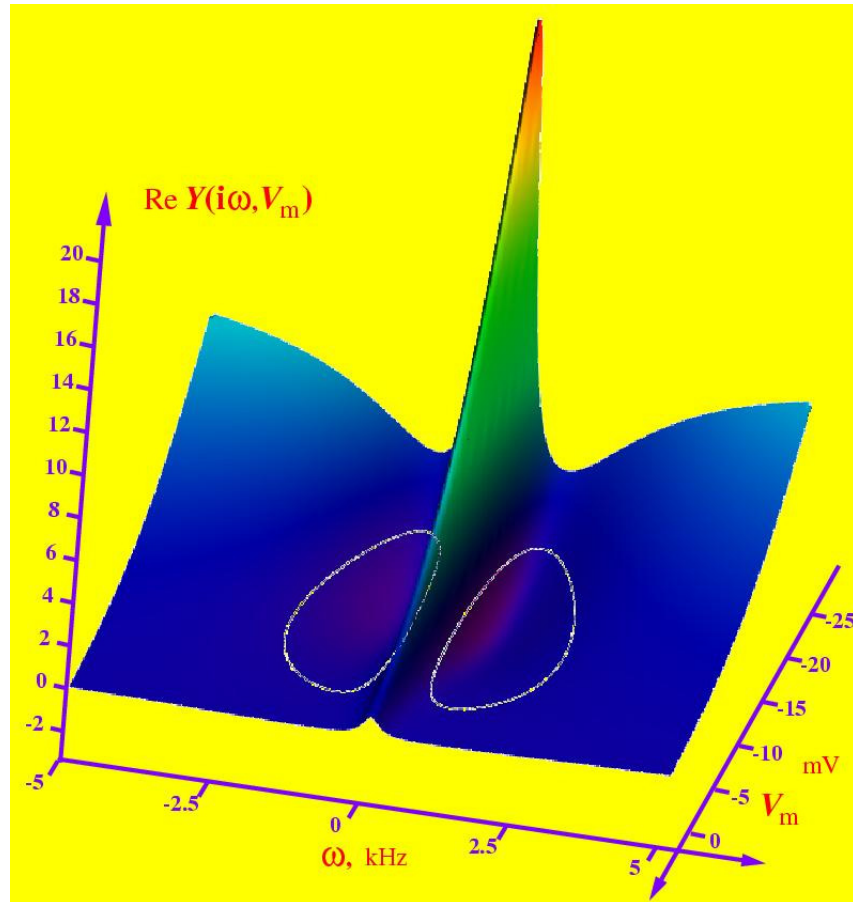


Fig. 14. Plot of the surface of $\text{Re } Y(i\omega; V_m)$ as a function of ω and V_m . The white contours denote the loci where $\text{Re } Y(i\omega; V_m) = 0$.

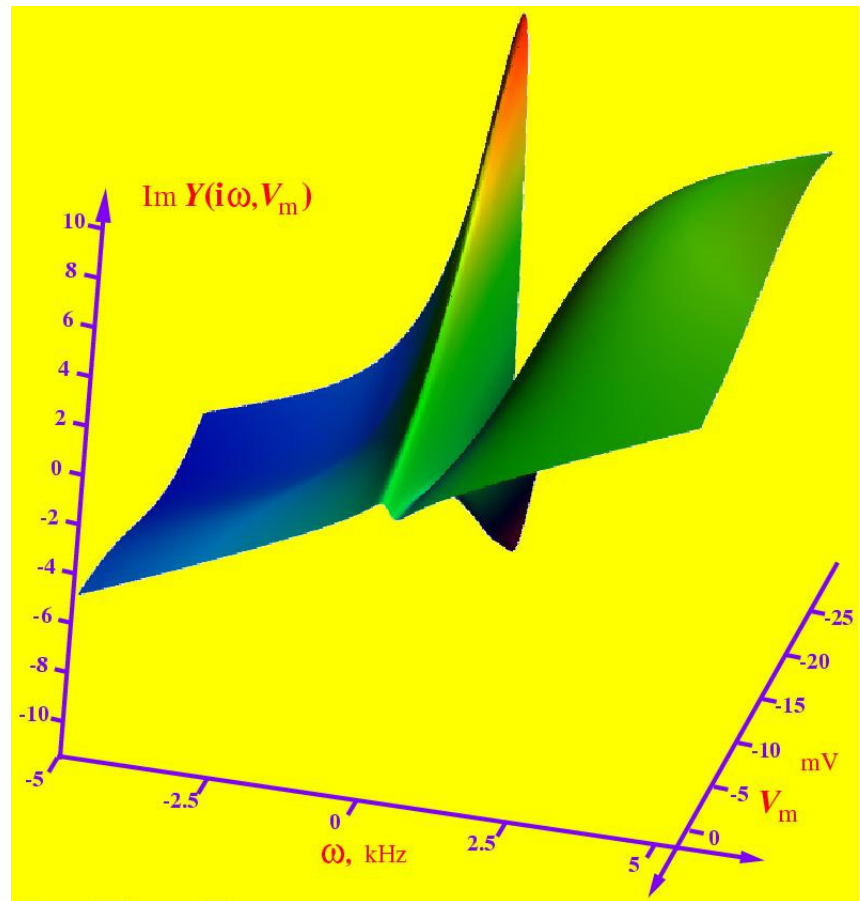


Fig. 15. Plot of the surface of $\text{Im } Y(i\omega; V_m)$ as a function of ω and V_m .

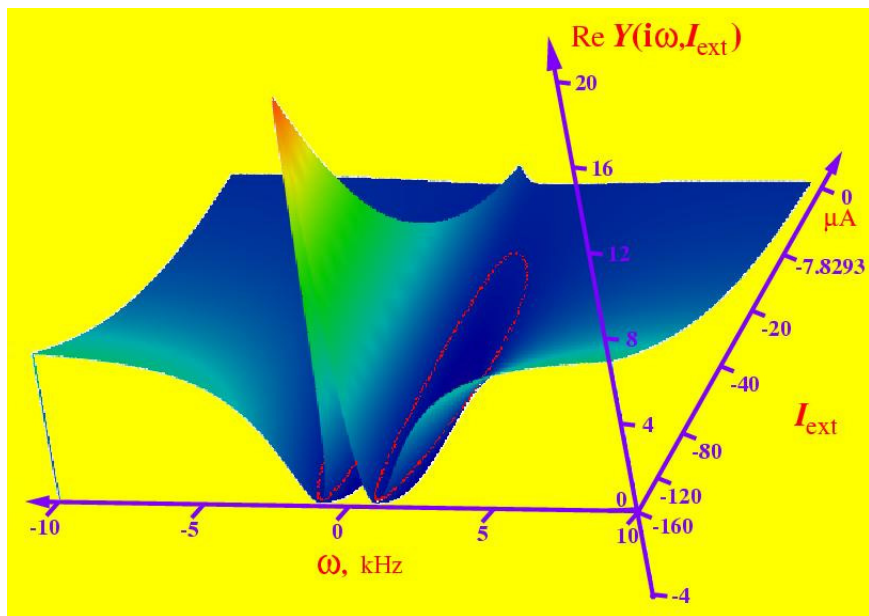


Fig. 16. Plot of the surface of $\text{Re } Y(i\omega; I_{\text{ext}})$ as a function of ω and I_{ext} .

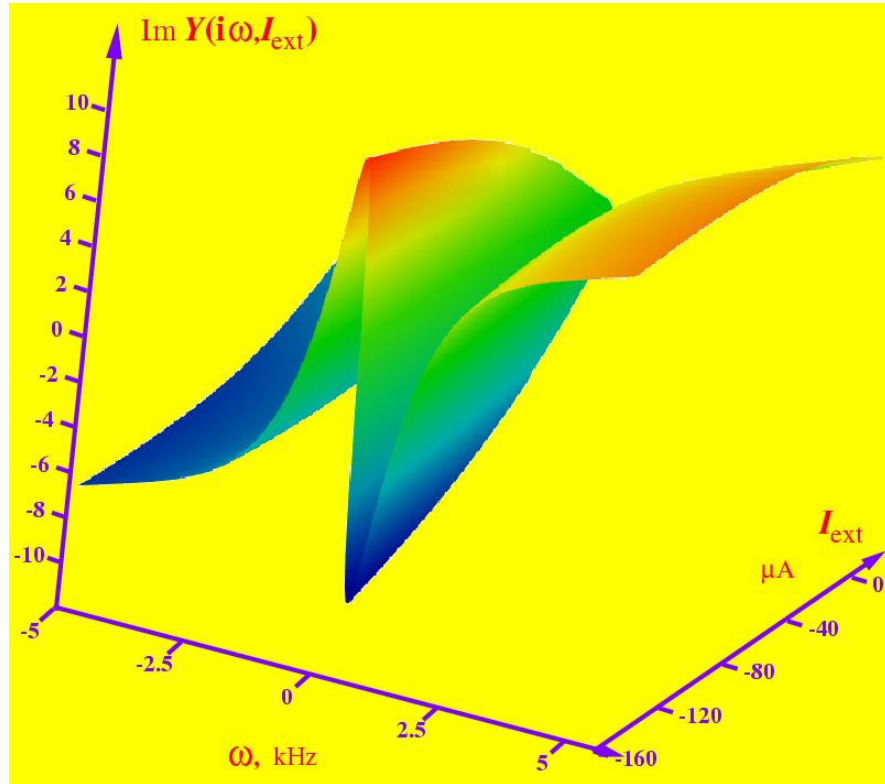


Fig. 17. Plot of the surface of $\text{Im } Y(i\omega; I_{\text{ext}})$ as a function of ω and I_{ext} .

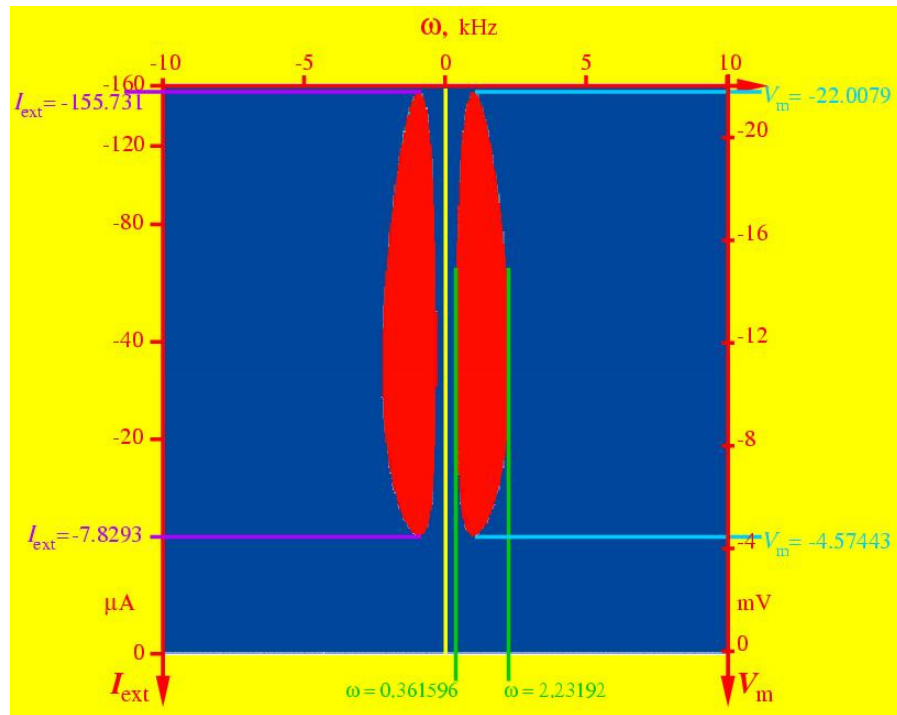


Fig. 18. All points inside the closed contours correspond to $\text{Re } Y(i\omega; V_m) < 0$ and $\text{Re } Y(i\omega; I_{\text{ext}}) < 0$.

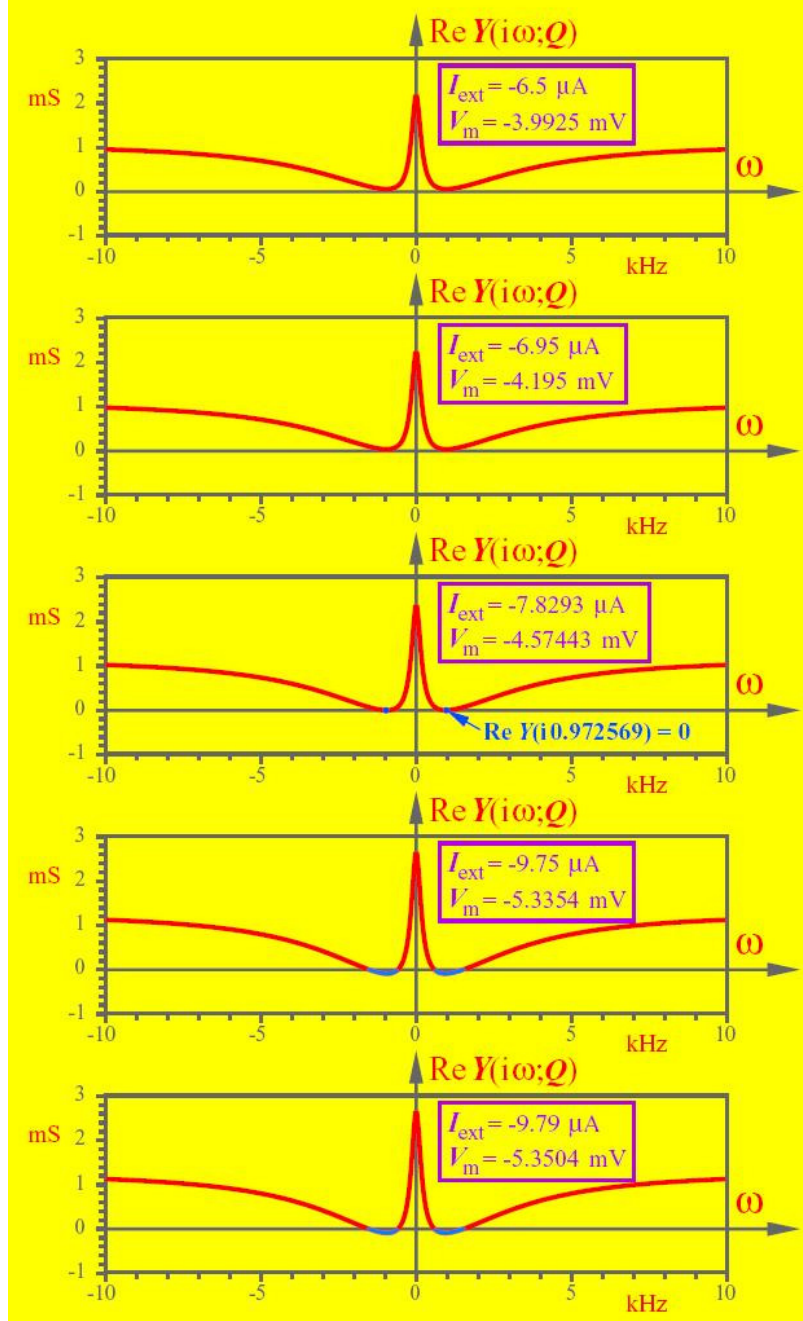


Fig. 19. Five cross-sections of $\text{Re } Y(i\omega; Q)$ from the surface in Figs. 14 and 16, where Q is the equilibrium point at $V_m = V_m(I_{\text{ext}})$, shown for five values of I_{ext} and V_m .

the parameter values of V_m and I_{ext} of each section are specified inside parameter boxes.

A careful examination of $\text{Re } Y(i\omega; V_m)$ in Fig. 14 and $\text{Re } Y(i\omega; I_{\text{ext}})$ in Fig. 16 shows that

$$\text{Re } Y(i\omega; V_m) > 0 \quad \text{for } V_m > -4.57443 \text{ mV} \quad (23a)$$

and

$$\text{Re } Y(i\omega; I_{\text{ext}}) > 0 \quad \text{for } I_{\text{ext}} > -7.8293 \mu\text{A}. \quad (23b)$$

It follows that the *edge of chaos* domain of the Hodgkin–Huxley axon model begins at $V_m = -4.57443 \text{ mV}$, or equivalently, at $I_{\text{ext}} = -7.8293 \mu\text{A}$ as manifested in the third cross-section in Fig. 19, and enlarged in Fig. 21, where the function $\text{Re } Y(i\omega; Q)$ is tangent to the ω -axis at the two blue dots (minima) located at $\omega = \pm 0.972569$.

Observe however from Fig. 13 that at $I_{\text{ext}} = -9.77004 \mu\text{A}$, or $V_m(I_{\text{ext}}) = -5.34305 \text{ mV}$ the

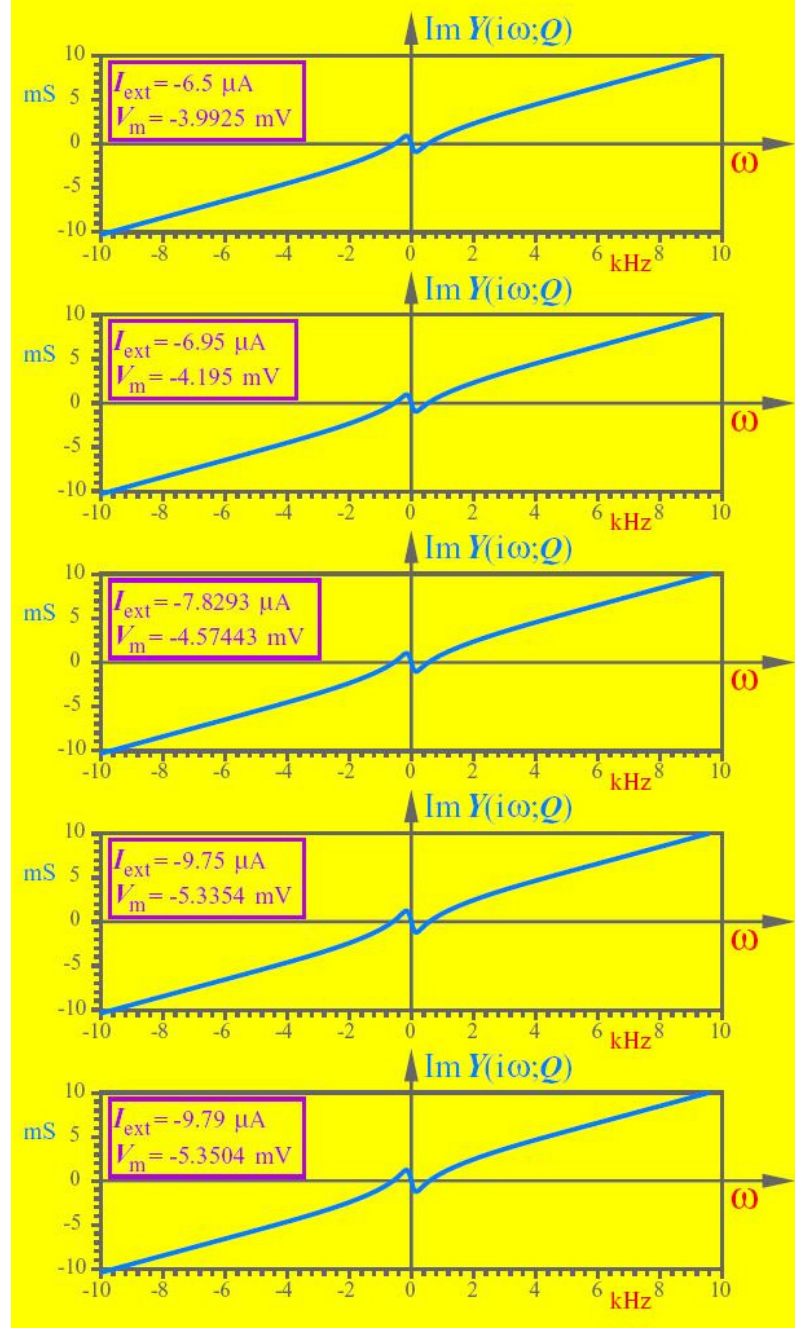


Fig. 20. Five cross-sections of $\text{Im } Y(i\omega; Q)$ corresponding to those depicted in Fig. 19.

complex zeros z_1 and z_2 of the admittance function $Y(s; Q)$, or equivalently, the complex poles p_1 and p_2 of the impedance function $Z(s; Q)$, have migrated to the imaginary axis. This is confirmed by the cross-section of $\text{Re } Y(i\omega; Q)$ shown in Fig. 22, at $I_{\text{ext}} = -9.77004 \mu\text{A}$, or equivalently, at $V_m = -5.34305 \text{ mV}$, where both $\text{Re } Y(i\omega; Q)$ and $\text{Im } Y(i\omega; Q)$ vanish at $\omega = 0.586124$. In other words $z_1 = i(0.586124)$ and $z_2 = -i(0.586124)$

are zeros of the admittance function $Y(s; Q)$ at the above parameter value. Hence, the impedance function $Z(s; Q)$ has a pair of complex-conjugate poles at $p_1 = i(0.586124)$ and $p_2 = -i(0.586124)$, respectively.

It follows that the equilibrium point Q is no longer asymptotically stable at the above parameter value of I_{ext} , and becomes unstable thereafter. In other words the *edge of chaos* regime which started

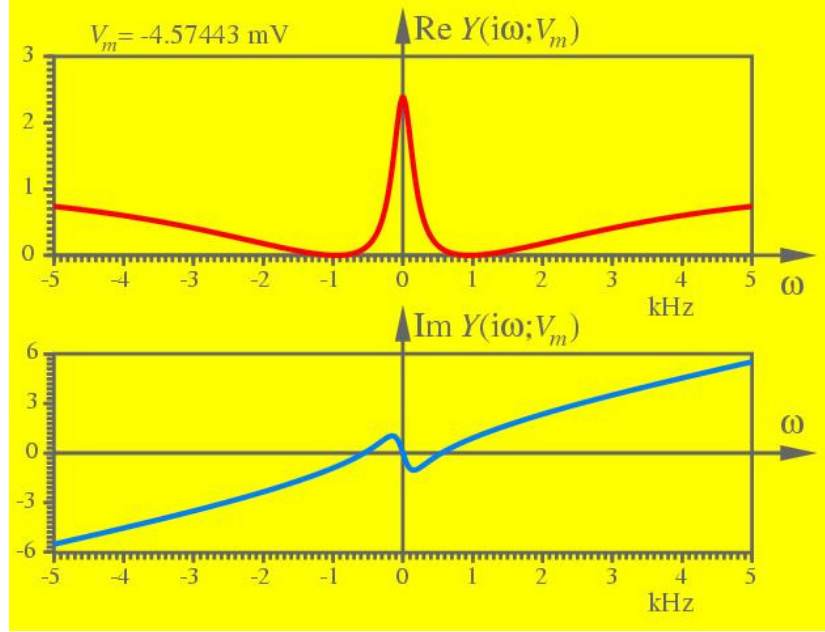


Fig. 21. Enlargement of $\text{Re } Y(i\omega; Q)$ at the onset of edge of chaos at $V_m = -4.57443 \text{ mV}$, or equivalently, at $I_{\text{ext}} = -9.75 \mu\text{A}$.

at $I_{\text{ext}} = -7.8293 \mu\text{A}$, or $V_m = -4.57443 \text{ mV}$, exists only over the following rather short interval:

Edge of Chaos domain 1:

$$\begin{aligned} -5.34305 \text{ mV} < V_m < -4.57443 \text{ mV} \\ -9.77003 \mu\text{A} < I_{\text{ext}} < -7.8293 \mu\text{A} \end{aligned} \quad (24)$$

But the loci of the two complex zeros z_1 and z_2 of $Y(s; Q)$ in Fig. 13 reveals that at $V_m = -21.9425 \text{ mV}$, or equivalently, at $I_{\text{ext}} = -154.529 \mu\text{A}$, the two complex zeros had migrated back to the imaginary axis and will enter the left-half plane (LHP) thereafter. This is confirmed by the cross-section of $\text{Re } Y(i\omega; Q)$ in Fig. 23 at $V_m = -21.9425 \text{ mV}$ or equivalently,

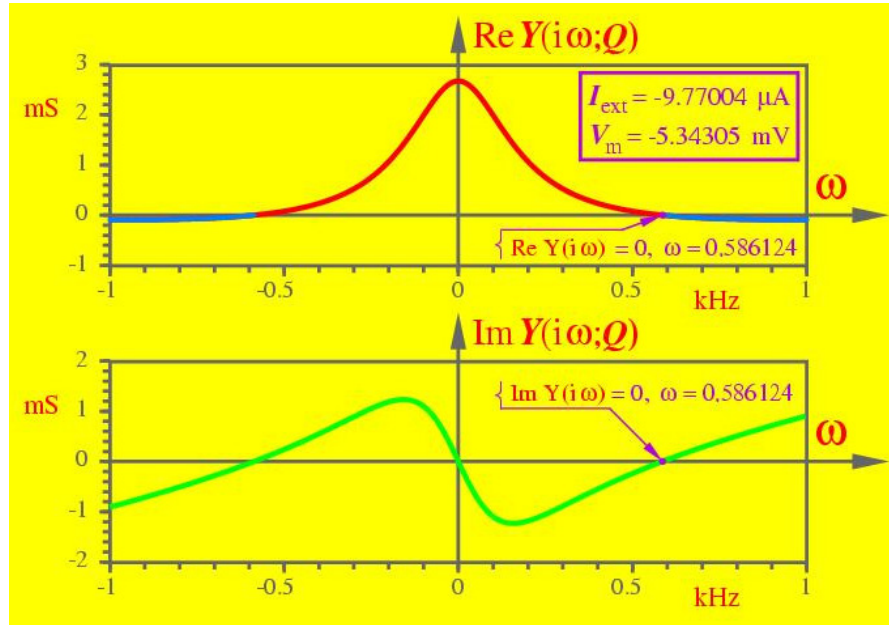


Fig. 22. Cross-section of $\text{Re } Y(i\omega; Q)$ at $V_m = -5.34305 \text{ mV}$, where $I_{\text{ext}} = -9.77004 \mu\text{A}$.

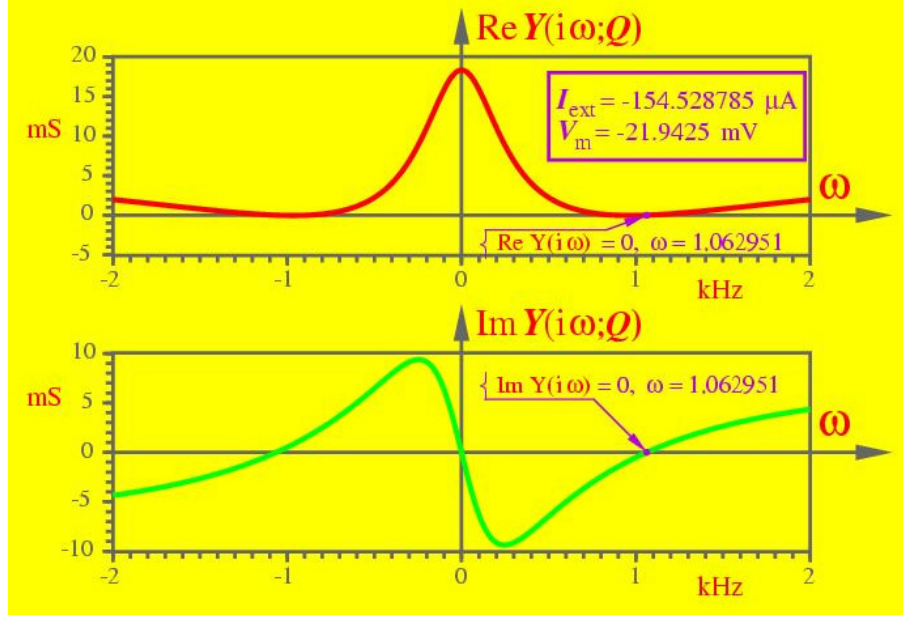


Fig. 23. Cross-section of $\text{Re } Y(i\omega; Q)$ at $V_m = -21.9425 \text{ mV}$, where $I_{\text{ext}} = -154.528785 \mu\text{A}$.

$I_{\text{ext}} = -154.528785 \mu\text{A}$, where both $\text{Re } Y(i\omega; Q)$ and $\text{Im } Y(i\omega; Q)$ vanish at $\omega = 1.062951$.

A careful examination of the surface $\text{Re } Y(i\omega; I_{\text{ext}})$ in Fig. 16 in the neighborhood of $I_{\text{ext}} = -154.529 \mu\text{A}$ reveals that the surface is below “ground” level, implying that there exists a second edge of chaos domain beginning from

$I_{\text{ext}} = -154.529 \mu\text{A}$, or $V_m = -21.9425 \text{ mV}$, where $\text{Re } Y(i\omega; Q) < 0$. Our numerical calculation confirms that this is indeed the case, and that $\text{Re } Y(i\omega; Q) = 0$ at $I_{\text{ext}} = -155.731 \mu\text{A}$, or equivalently, at $V_m = -22.0079 \text{ mV}$, as depicted in the cross-section shown in Fig. 24. It follows from this numerical analysis that the Hodgkin–Huxley axon

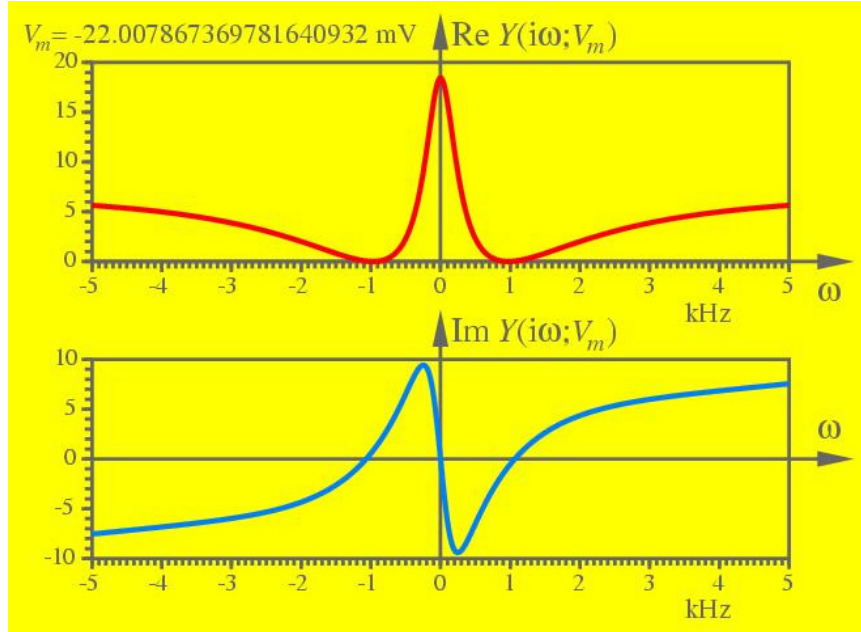


Fig. 24. Cross-section of $\text{Re } Y(i\omega; V_m)$ at $V_m = -22.0079 \text{ mV}$, where $I_{\text{ext}} = -155.731 \mu\text{A}$.

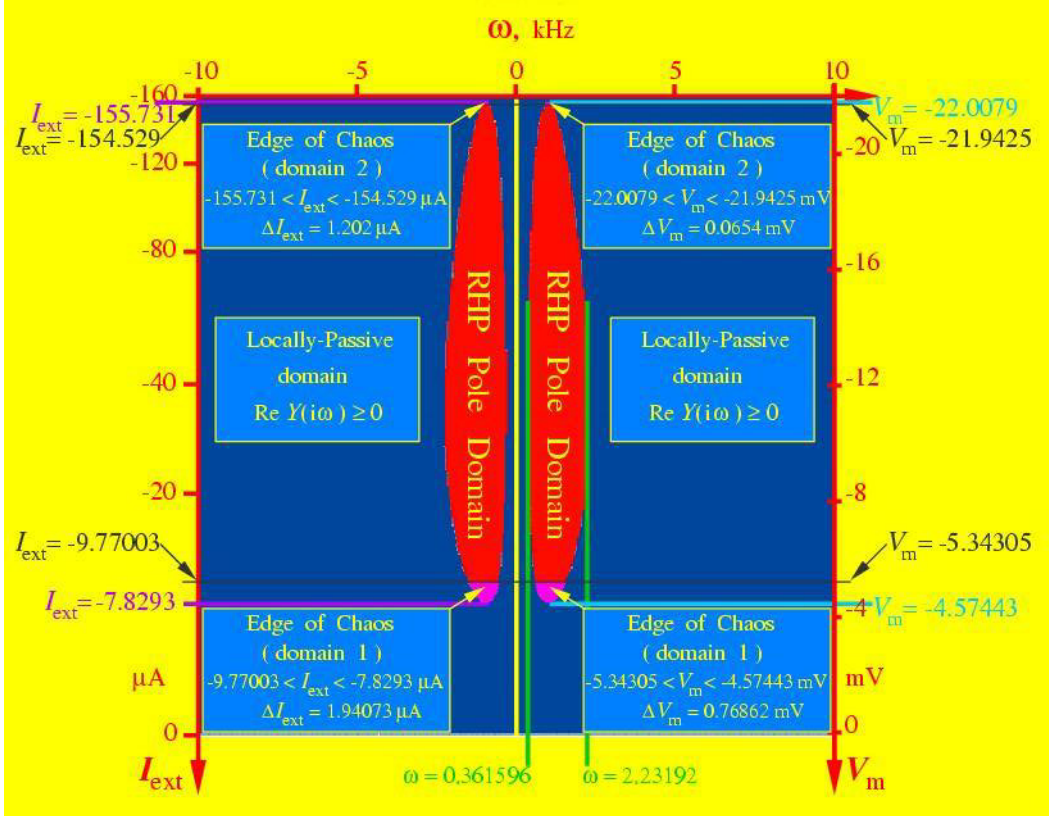


Fig. 25. The two disjoint Edge of Chaos domains are located at the lower and upper tips (not drawn according to scale in magenta color) of the two red Islands.

is endowed with a second, albeit even smaller, edge of chaos regime:

Edge of Chaos domain 2:

$$\begin{aligned} -22.0079 \text{ mV} < V_m < -21.9425 \text{ mV} \\ -155.731 \mu\text{A} < I_{\text{ext}} < 154.529 \mu\text{A} \end{aligned}$$

(25)

The above two disjoint Edge of Chaos domains of the Hodgkin–Huxley axon are identified at the lower and the upper tips of the two islands in Fig. 25. Note that the interval ΔV_m and ΔI_{ext} where the edge-of-chaos regime exists in Fig. 25 (identified in magenta color) is extremely small,⁹ namely ΔI_{ext} is less than 2 μA and ΔV_m is less than 1 mV!

5. Subcritical Hopf Bifurcation

Let us examine carefully the loci of the zeros of the admittance function $Y(s; V_m(I_{\text{ext}}))$, or equivalently, the poles of the impedance function $Z(s; V_m(I_{\text{ext}}))$

in Fig. 13, in the neighborhood of the resting potential $V_m = 0$ at $I_{\text{ext}} = 0$. As we decrease the DC excitation current from $I_{\text{ext}} = 0$ to $I_{\text{ext}} = -9.77003 \mu\text{A}$, V_m decreases from $V_m = 0$ to $V_m = -5.34305 \text{ mV}$, and the complex-conjugate poles p_1 and p_2 of $Z(s; V_m(I_{\text{ext}}))$ migrates from the resting equilibrium at $V_m = 0$ to a point on the imaginary axis. Any further decrease in $|I_{\text{ext}}|$ would cause the poles to cross the imaginary axis *transversally* and move into the RHP. By extensive numerical simulations, we have determined that a *subcritical Hopf bifurcation* [Alligood *et al.*, 1997] occurs at $I_{\text{ext}} = -9.77003 \mu\text{A}$.

The subcritical Hopf bifurcation theorem predicts that there is very small *unstable* sinusoidal solution with frequency ω equal approximately to the imaginary part of the pole of $Z(s; V_m(I_{\text{ext}}))$, or equivalently the zero of $Y(s; V_m(I_{\text{ext}}))$, at $I_{\text{ext}} = -9.77003 \mu\text{A}$, or $V_m = -5.34305 \text{ mV}$. This frequency was found earlier in Fig. 22 to be equal to $\omega = 0.586124 \text{ KHz}$, which is identical to the angular frequency $\omega = 0.586124 \text{ KHz}$ at the origin of the Nyquist plot of $\text{Im } Y(i\omega; V_m)$ versus $\text{Re } Y(i\omega; V_m)$

⁹The edge of chaos domain (magenta) in Fig. 25 are not drawn according to the scale of this figure for better visibility.

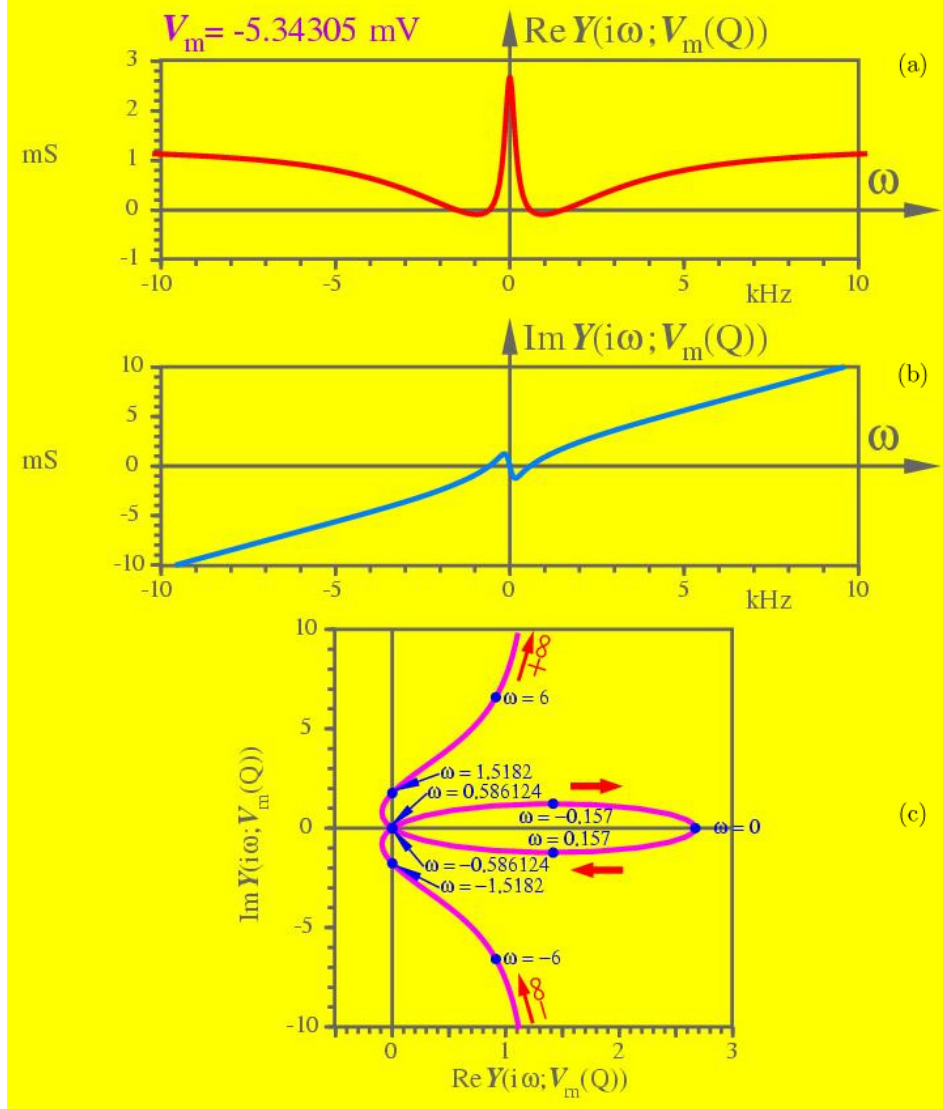


Fig. 26. Small-Signal Admittance $Y(i\omega; V_m(Q))$ frequency response of the Hodgkin–Huxley axon at $V_m = -5.34305$ mV. (a) $\text{Re } Y(i\omega; -5.34305 \text{ mV})$ versus ω . (b) $\text{Im } Y(i\omega; -5.34305 \text{ mV})$ versus ω . (c) Nyquist plot $\text{Im } Y(i\omega; -5.34305 \text{ mV})$ versus $\text{Re } Y(i\omega; -5.34305 \text{ mV})$.

depicted in Fig. 26. It follows from the prediction of the *subcritical* Hopf Bifurcation theorem that for I_{ext} chosen within the very small *edge of chaos* domain 1, where the equilibrium point Q has an eigenvalue with a negative real part and is therefore locally asymptotically stable, we can expect a very-small amplitude *unstable* sinusoidal oscillation which would diverge, in the presence of numerical noise, to either a stable equilibrium point V_m , or to a nonsinusoidal periodic oscillation (i.e. an attractor) namely, a *spike train*, i.e. an action potential with a large amplitude. The above possible scenarios are illustrated in Fig. 27. The upper waveform shows a transient waveform converging to a spike

train with the initial condition indicated. The second waveform shows a very small sinusoidal oscillation with amplitude $A = 1.7317 \times 10^{-6}$ mV, and frequency $f = 93.197$ Hz. Note that f is very close to the predicted Hopf frequency

$$f_{\text{Hopf}} = \frac{\omega}{2\pi} = \frac{0.586035 \times 10^3}{2\pi} = 93.270 \text{ Hz}$$

The initial condition in all four waveforms are identical, except for $V_m(0)$. The spike train results from $V_m(0) = -5.1366$ mV, whereas the small amplitude oscillation results from $V_m(0) = -5.3403497902$ mV. Observe that because the damping is very small ($\text{Re } z_1 \approx 0$ but negative) the

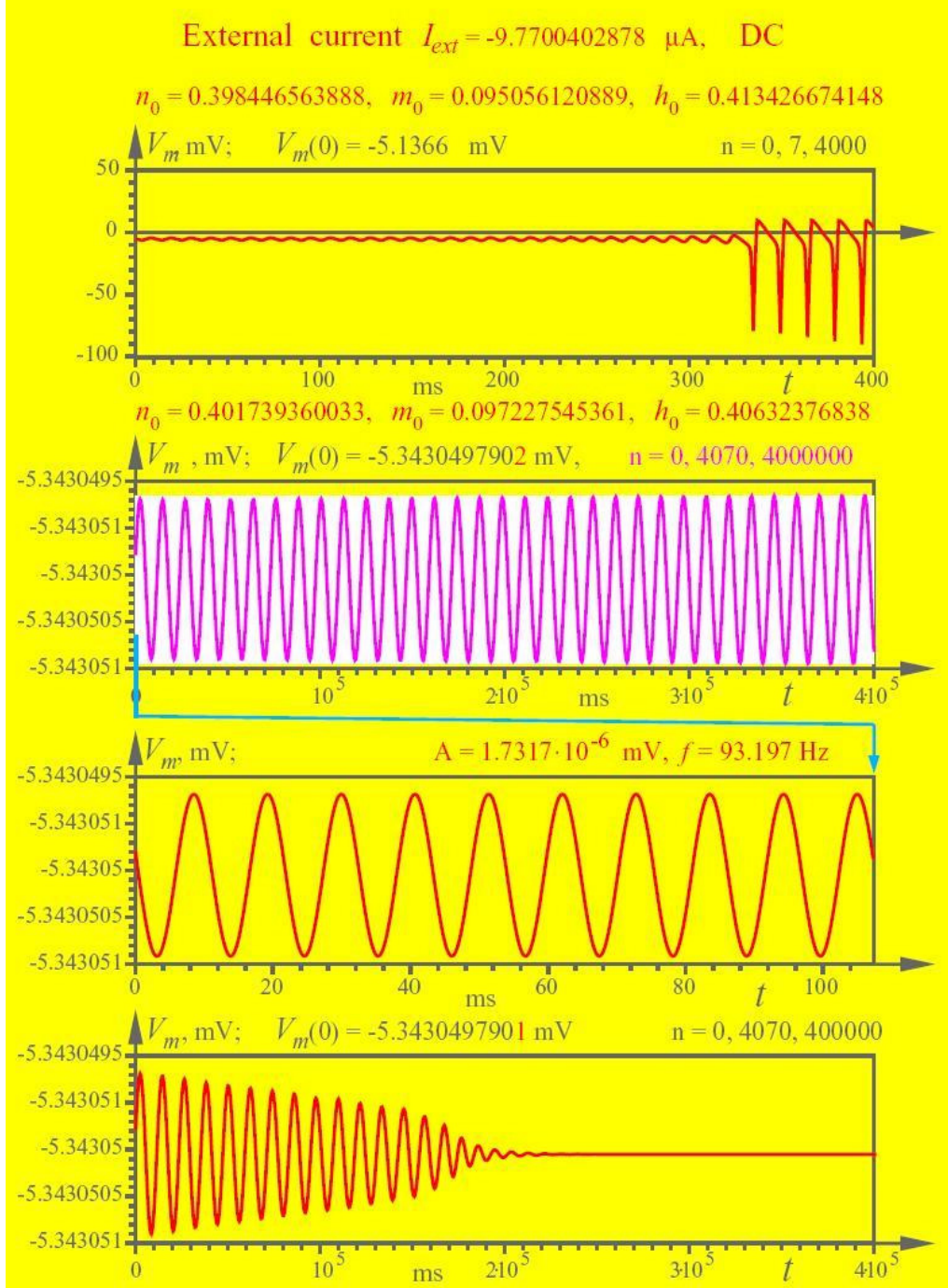


Fig. 27. Computer simulations confirming the prediction of the subcritical Hopf bifurcation theorem for $I_{ext} = -9.7700402878 \mu\text{A}$ and $V_m = -5.34305 \text{ mV}$. To avoid clutter and improve readability, the top waveform is plotted every seven time steps, whereas the second and the fourth waveforms are plotted every 4070 time steps.

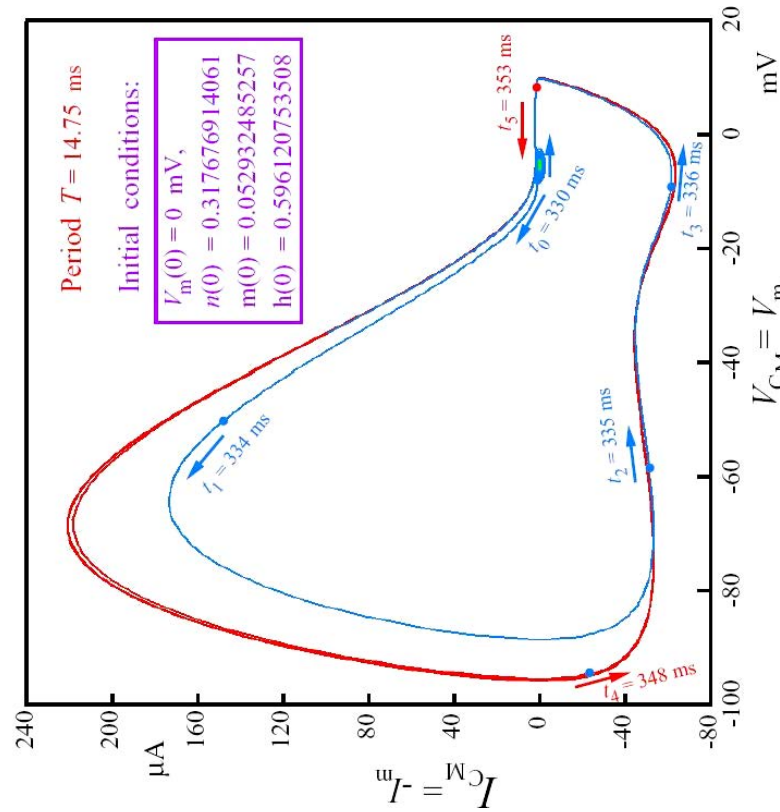
amplitude of the oscillation replotted in the third waveform over $t \in [0, 100 \text{ ms}]$ appears to remain constant.

Finally, with an infinitesimally small perturbation in the initial condition of the preceding oscillation $V_m(0) = -5.3430497902 \text{ mV}$, at

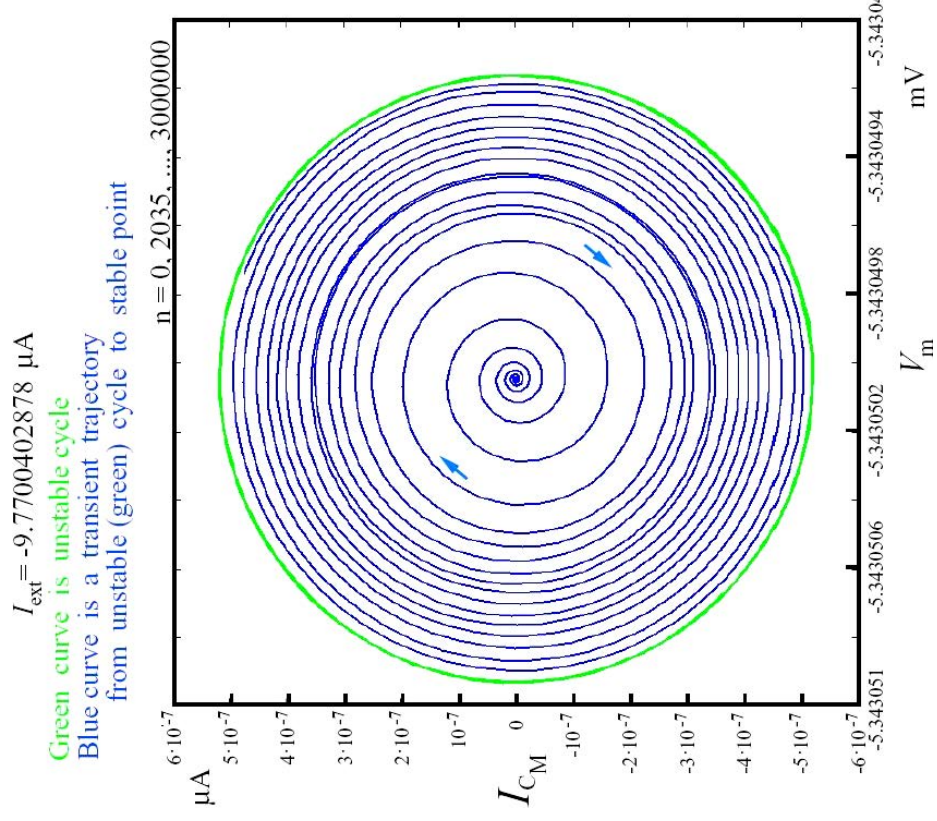
the tenth decimal position, namely, $V_m(0) = -5.3430497901 \text{ mV}$, we find this waveform converges to a DC equilibrium.

The Lissajous figure between the capacitor current $I_{CM}(t)$ and the membrane voltage $V_m(t)$ of the HH axon equations with $I_{ext} = -9.7700402878 \mu\text{A}$,

$I_{\text{ext}} = -9.7700402878 \mu\text{A}$
 Green curve is unstable cycle
 Blue curve is a transient trajectory from unstable (green) cycle to stable (red) outer cycle
 Red curve is a stable cycle of spike pulses



(a)



(b)

Fig. 28. Lissajous figures of I_{C_M} versus V_m associated with Fig. 27 for $I_{\text{ext}} = -9.7700402878 \mu\text{A}$. (a) Action potential. (b) Small sinusoidal oscillation. To avoid clutter and improve visibility, only data points at regular interval of 2035 time steps are shown.

$$I_{\text{ext}} = -9.7700402878 \mu\text{A}$$

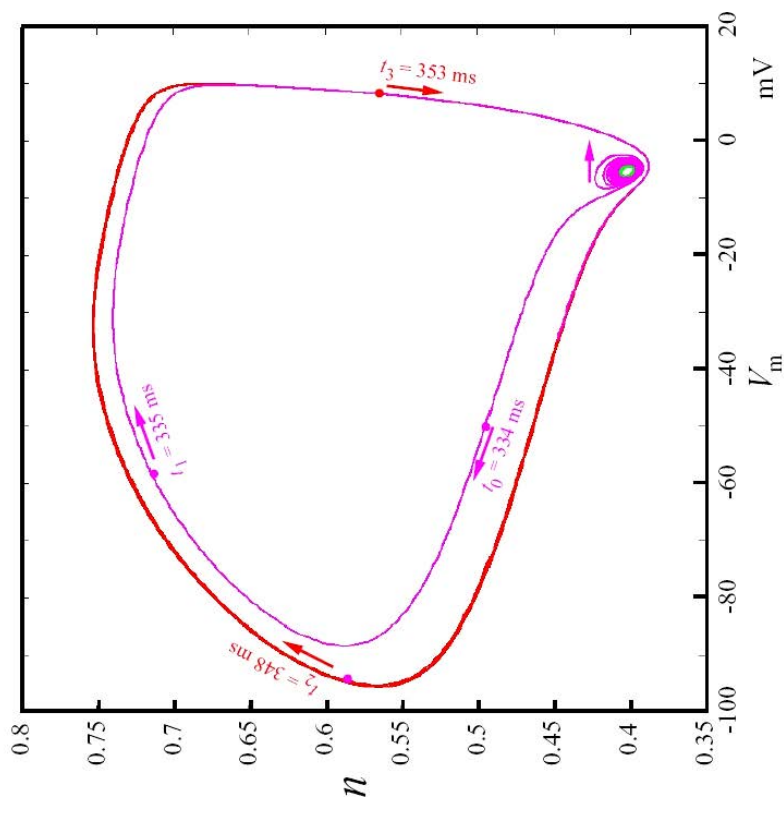
Green curve is unstable cycle

Blue curve is a transient trajectory from unstable (green) cycle to stable point
Magenta curve is a transient trajectory from unstable (green) cycle to stable (red) outer cycle
Red curve is a stable cycle of spike pulses

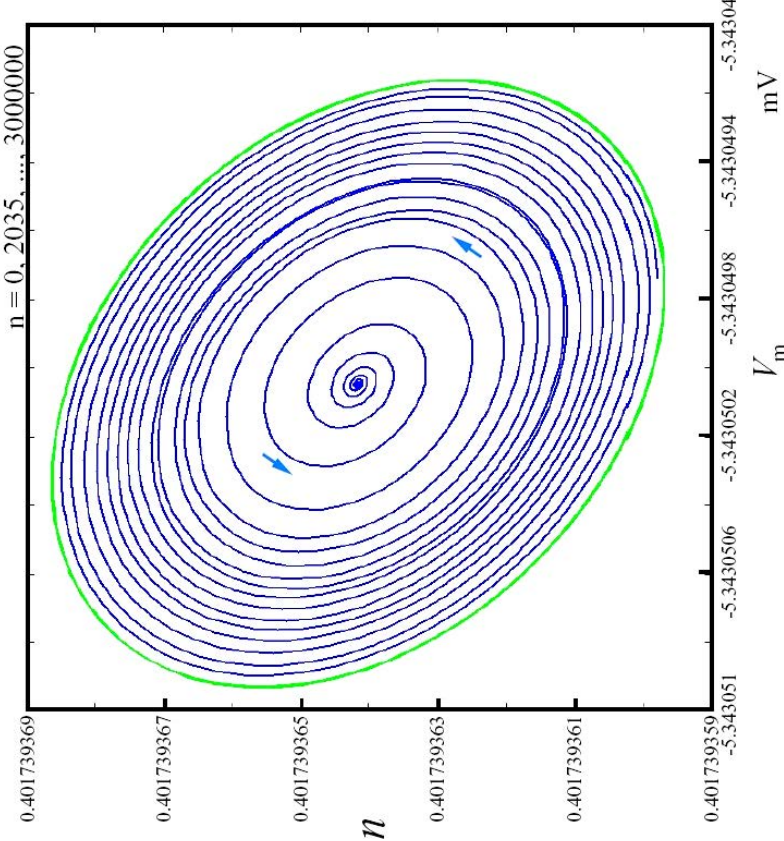
$$I_{\text{ext}} = -9.7700402878 \mu\text{A}$$

Green curve is unstable cycle

Blue curve is a transient trajectory from unstable (green) cycle to stable point
Magenta curve is a transient trajectory from unstable (green) cycle to stable (red) outer cycle
Red curve is a stable cycle of spike pulses



(a)



(b)

Fig. 29. Lissajous figures of n versus V_m associated with Fig. 27. (a) Action potential. (b) Small sinusoidal oscillation. To avoid clutter and improve visibility, only data points at regular interval of 2035 time steps are shown.

$$I_{\text{ext}} = -9.7700402878 \mu\text{A}$$

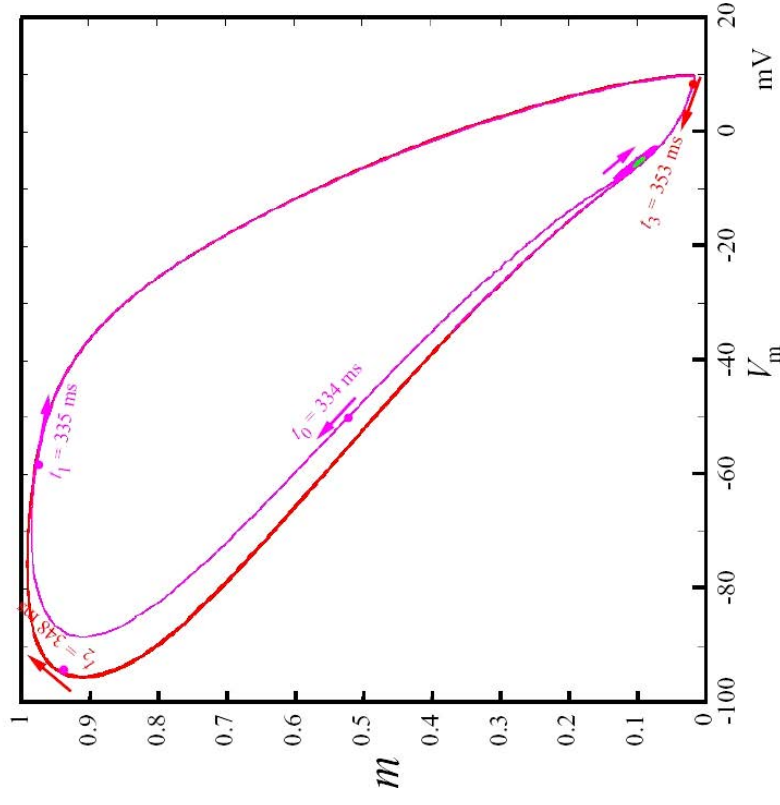
Green curve is unstable cycle

Blue curve is a transient trajectory from unstable (green) cycle to stable point
Magenta curve is a transient trajectory from unstable (green) cycle to stable (red) outer cycle
Red curve is a stable cycle of spike pulses

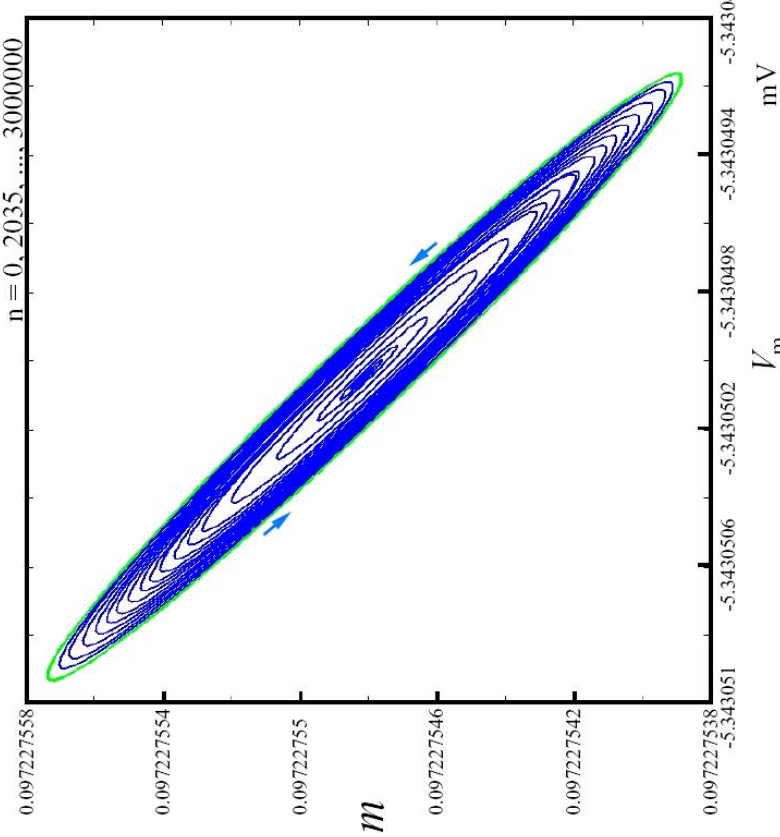
$$I_{\text{ext}} = -9.7700402878 \mu\text{A}$$

Green curve is unstable cycle

Blue curve is a transient trajectory from unstable (green) cycle to stable point
Magenta curve is a transient trajectory from unstable (green) cycle to stable (red) outer cycle
Red curve is a stable cycle of spike pulses



(a)



(b)

Fig. 30. Lissajoux figures of m versus V_m associated with Fig. 27. (a) Action potential. (b) Small sinusoidal oscillation. To avoid clutter and improve visibility, only data points at regular interval of 2035 time steps are shown.

$I_{\text{ext}} = -9.7700402878 \mu\text{A}$
Green curve is unstable cycle
 Blue curve is a transient trajectory from unstable (green) cycle to stable point
Magenta curve is a transient trajectory from unstable (green) cycle to stable (red) outer cycle
Red curve is a stable cycle of spike pulses

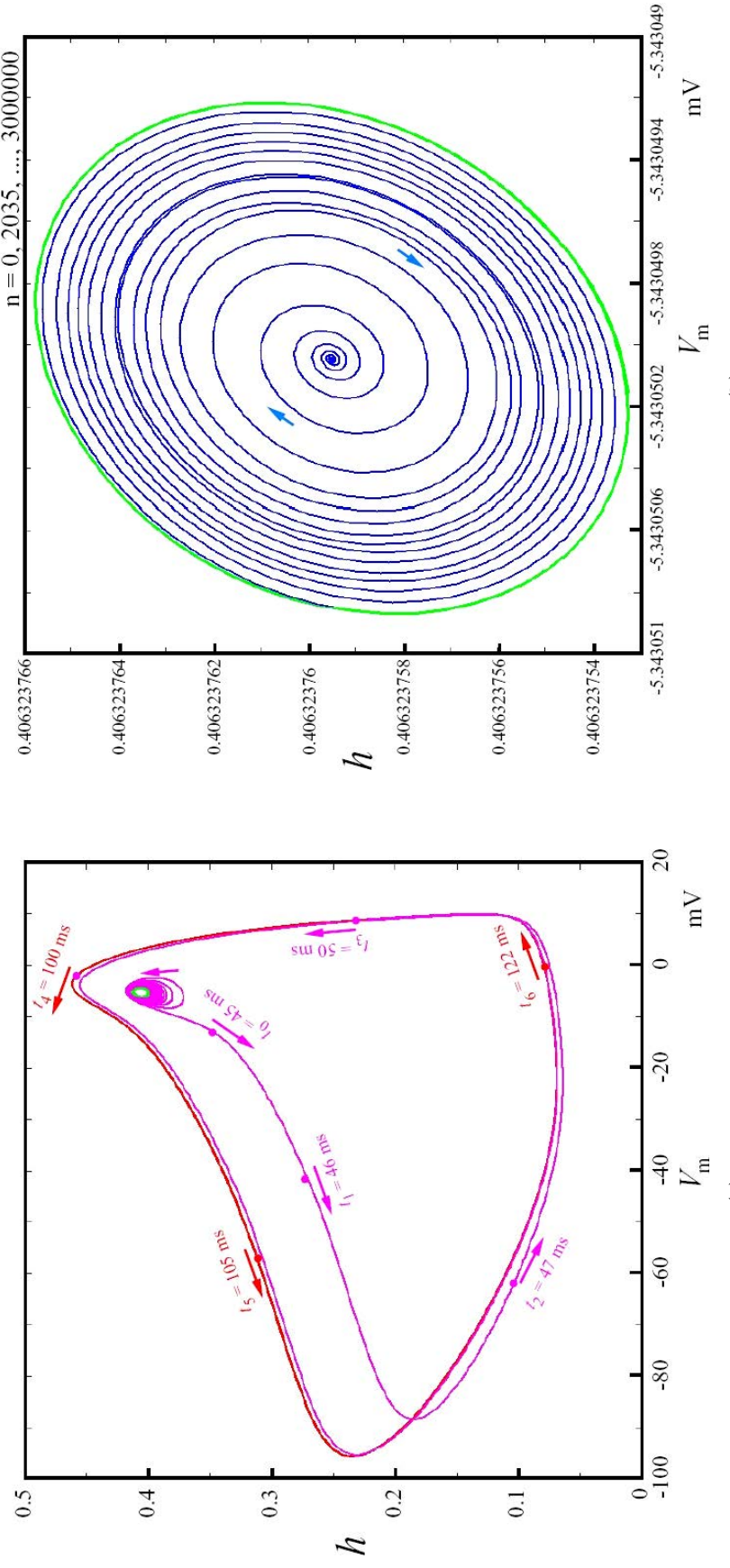


Fig. 31. Lissajous figures of h versus V_m associated with Fig. 27. (a) Action potential. (b) Small sinusoidal oscillation. To avoid clutter and improve visibility, only data points at regular interval of 2035 time steps are shown.

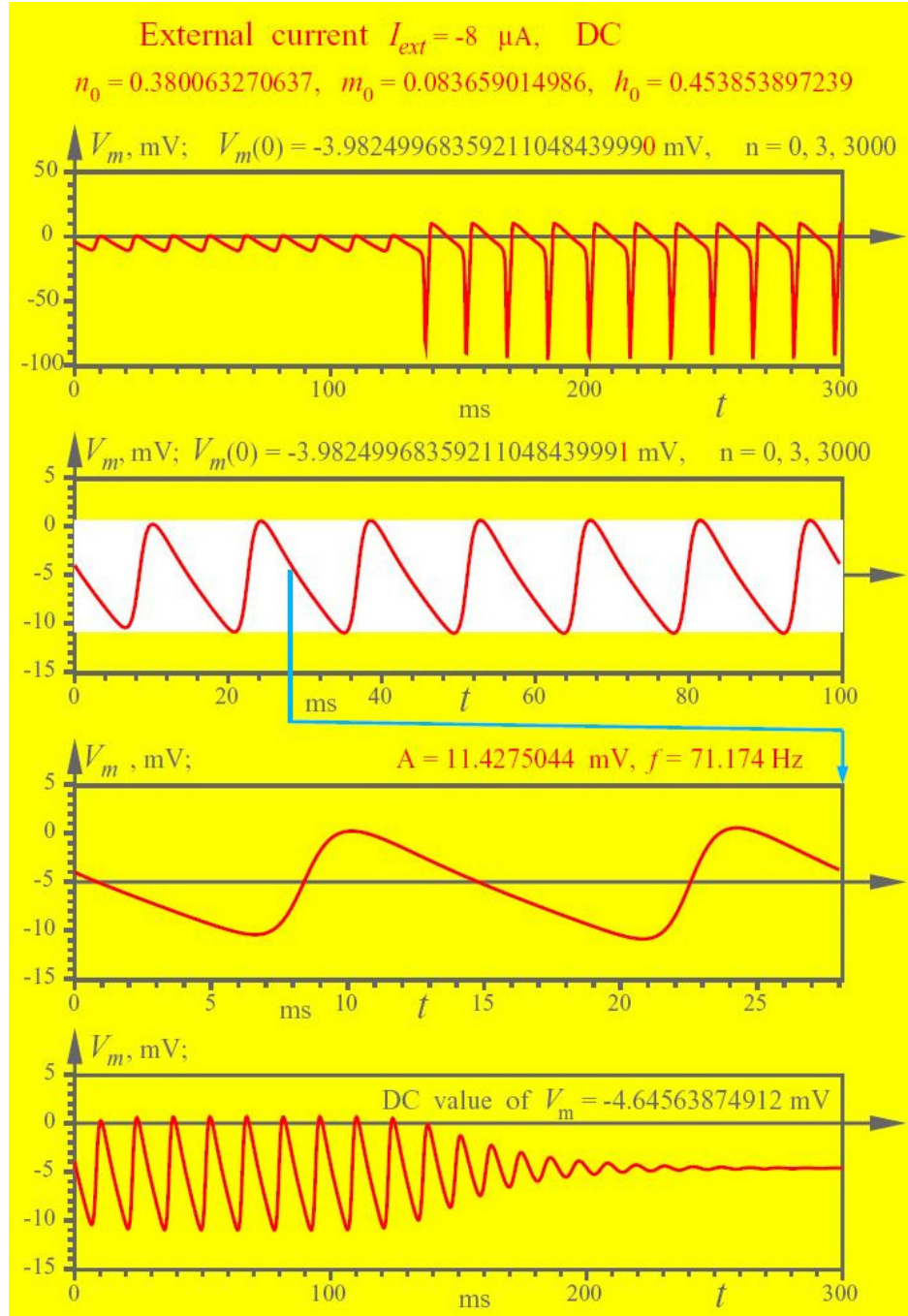


Fig. 32. Computer simulations confirming the prediction of the subcritical Hopf bifurcation theorem at $I_{ext} = -8 \mu\text{A}$ for three different initial conditions for $V_m(0)$. To avoid clutter and improve readability, the first two waveforms are plotted every three time steps.

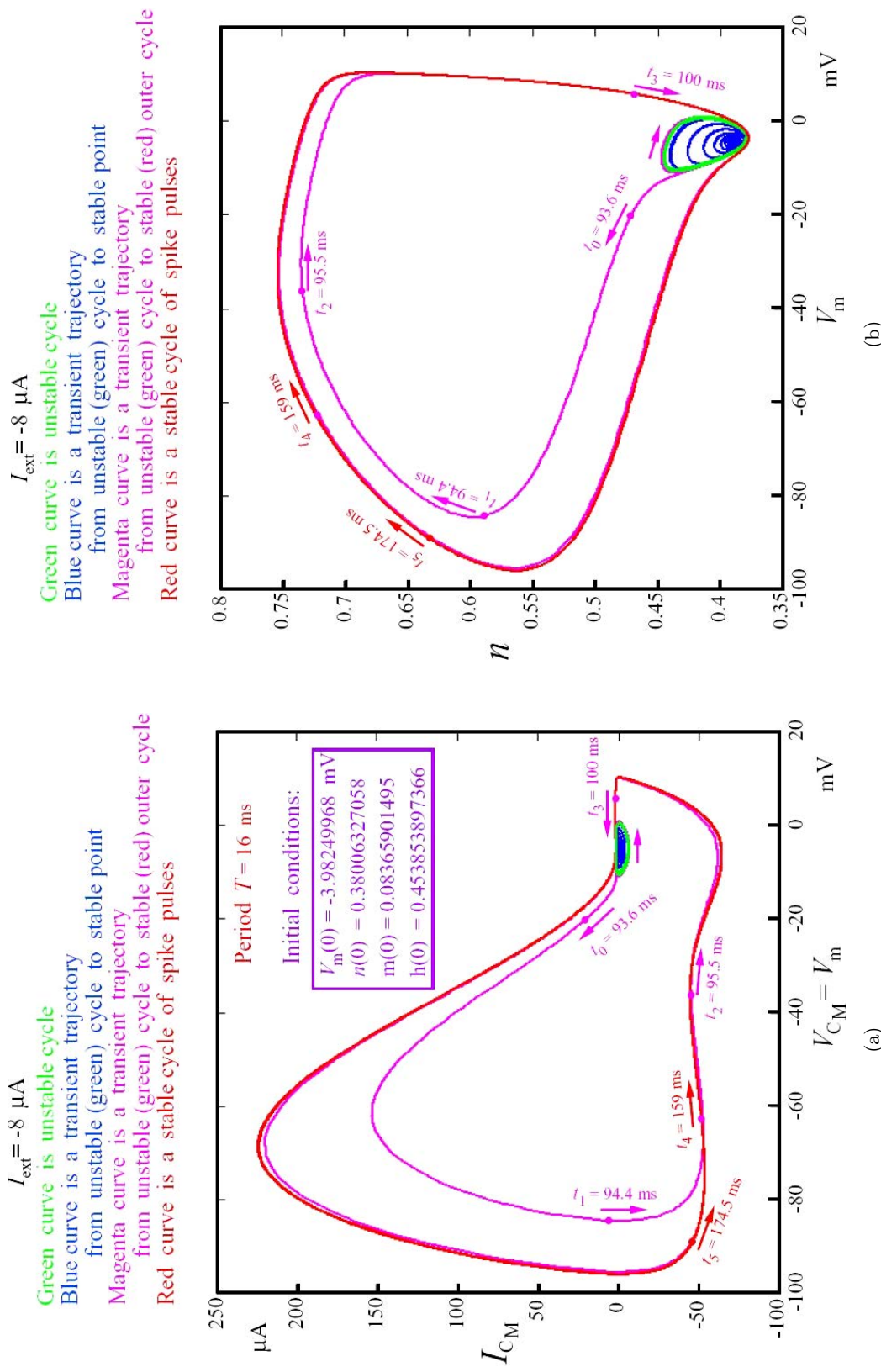


Fig. 33. Lissajous figures of action potential and unstable limit cycle associated with the waveform in Fig. 32 for $I_{ext} = -8 \mu A$. (a) I_{CM} versus V_m . (b) n versus V_m . (c) m versus V_m . (d) h versus V_m .

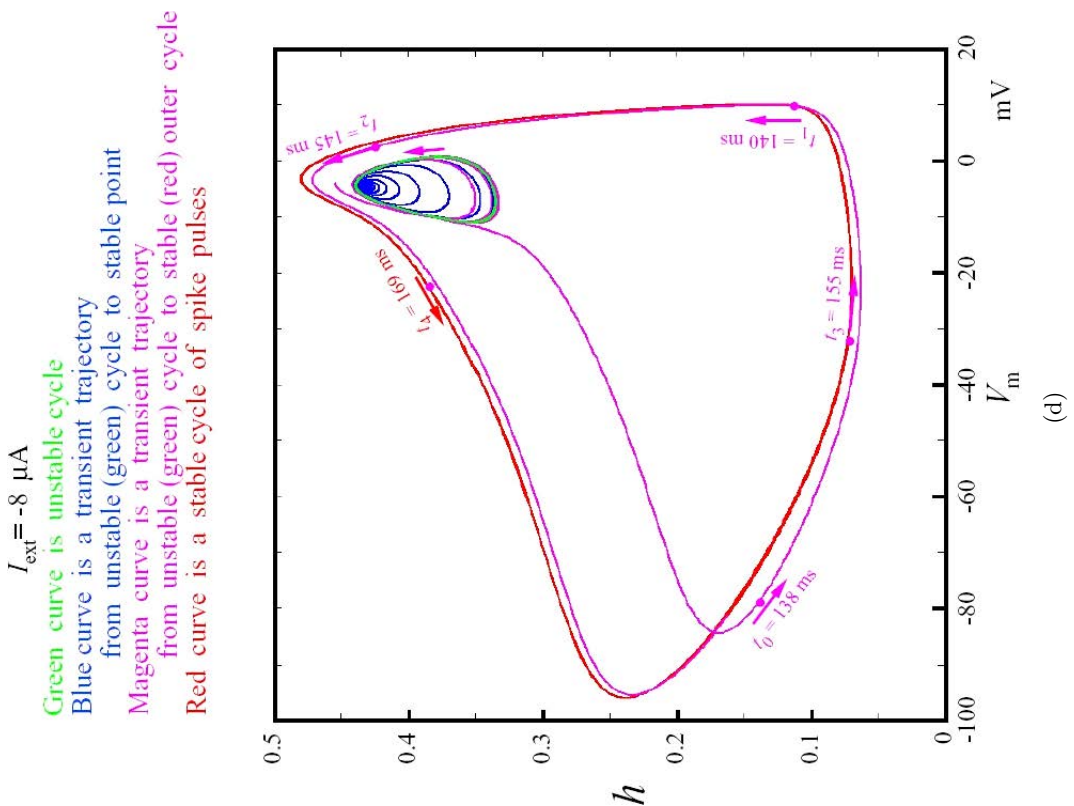
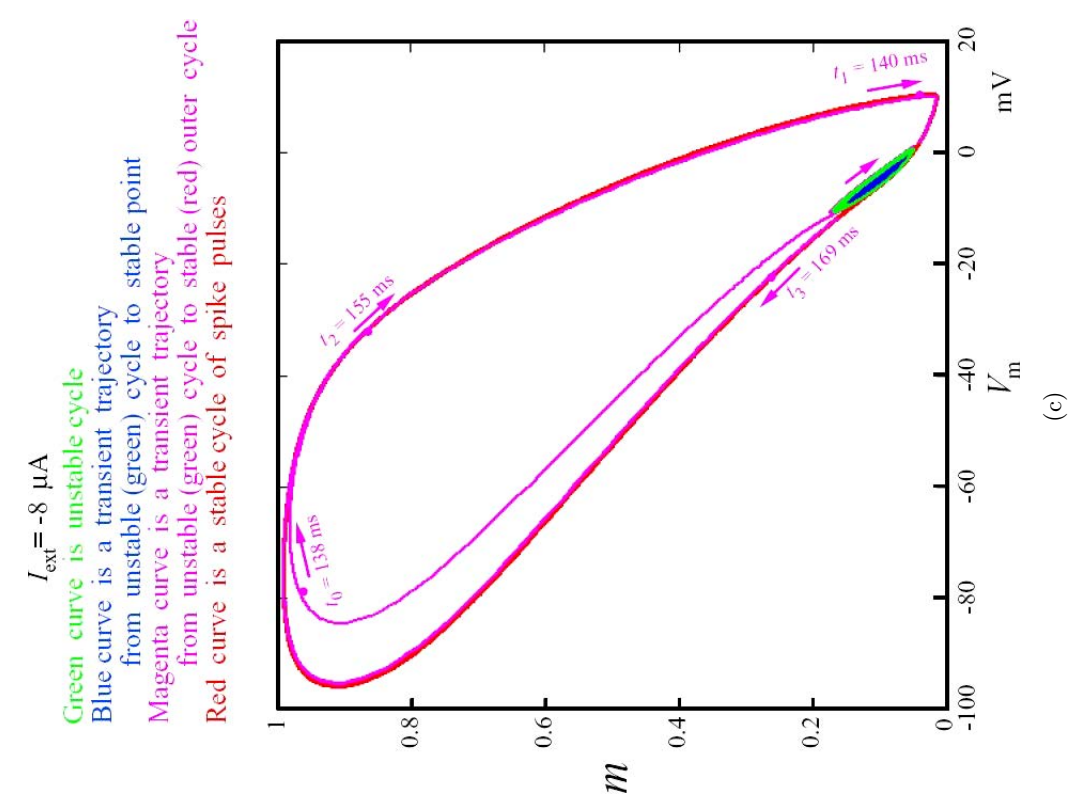


Fig. 33. (Continued)

or $V_m = -5.3403497902$ mV, is shown in Fig. 28(a) for a typical action potential, and in Fig. 28(b) for the very small sinusoidal oscillation. The Lissajoux figure of the corresponding pairs of the state variables n versus V_m , m versus V_m , and h versus V_m , are given in Figs. 29–31, respectively.

Finally, the waveforms and Lissajoux figures of the HH axon at $I_{\text{ext}} = -8 \mu\text{A}$ are shown in Figs. 32 and 33, respectively. Observe that the corresponding equilibrium point Q lies on the *edge of chaos* domain 1.

6. From Subcritical to Super-Critical Hopf Bifurcation

The preceding section shows that the right boundary $I_{\text{ext}} = -9.77003 \mu\text{A}$ (or $V_m(I_{\text{ext}}) = -5.34305$ mV) of the *edge of chaos* domain 1 in Fig. 25 coincides with the critical situation where a complex zero z_1 of the admittance function $Y(s; V_m)$ arrives at the imaginary axis. This critical situation gives rise to a *subcritical* Hopf bifurcation which predicts that an action potential can emerge even for smaller values of $|I_{\text{ext}}|$, where the zero z_1 has not yet arrived at the imaginary axis, but is sufficiently close to it, such as when the HH axon is poised on or *near* the edge of chaos domain 1. This counter-intuitive phenomenon arises in the HH equations because, as illustrated clearly in Figs. 28–31, the periodic sinusoidal solution predicted by the subcritical Hopf bifurcation theorem is very close to the stable equilibrium point and a very small perturbation from the stable equilibrium point Q at $V_m(I_{\text{ext}})$ could swing it into the basin of attraction of a much larger periodic attractor, namely, a spike train. Observe that the existence of a stable spike train is *not* predicted by the subcritical Hopf bifurcation theorem, which is valid only for dynamical phenomena confined to a small neighborhood of Q . However the *instability* of a limit cycle near Q makes it highly likely for the unstable limit cycle to diverge from Q and to converge to another attractor, assuming that the system is unstable at infinity.

Figure 34 shows the graph of the zeros of $Y(s; Q)$ as a function of I_{ext} as calculated from the polynomial Eq. (17). Only the graphs of $\text{Re } z_k$, $k = 1, 2, 3$, appear in the upper part of Fig. 34 because the graph of $\text{Re } z_4$ lies outside the domain represented in this figure. Since z_1 and z_2 are complex conjugate numbers over the range of interest in this paper, namely $I_{\text{ext}} < 0$, we plot the real parts $\text{Re } z_k$

of z_k in the upper part, and the imaginary part $\text{Im } z_k$ in the lower part of Fig. 34. In particular, the red and blue branches in the lower part are denoted by $\text{Im } z_1$ and $\text{Im } z_2$, respectively. Since both z_3 and z_4 are real numbers, $\text{Im } z_3$ (green) and $\text{Im } z_4$ (magenta) are both zero for all $I_{\text{ext}} < 0$. They are represented by the alternating green and magenta loci along the real axis.

The graphs of $\text{Re } z_1$ and $\text{Re } z_2$ are represented by alternating red and blue dashes in the upper part of Fig. 34 because $\text{Re } z_1 = \text{Re } z_2$.

The graph of $\text{Re } z_3$ is shown as green dashes in the lower curve to be consistent with its representation in $\text{Im } z_3$ in the bottom part of Fig. 34.

Now let us investigate how a typical spike train evolves as we decrease the value of $|I_{\text{ext}}|$ continuously along the upper “red-nose” RHP loci in Fig. 13.

Observe that

$$\text{Re } z_1 > 0, \quad \text{Re } z_2 > 0 \quad (26a)$$

over the range

$$-154.529 \mu\text{A} < I_{\text{ext}} < -9.77004 \mu\text{A} \quad (26b)$$

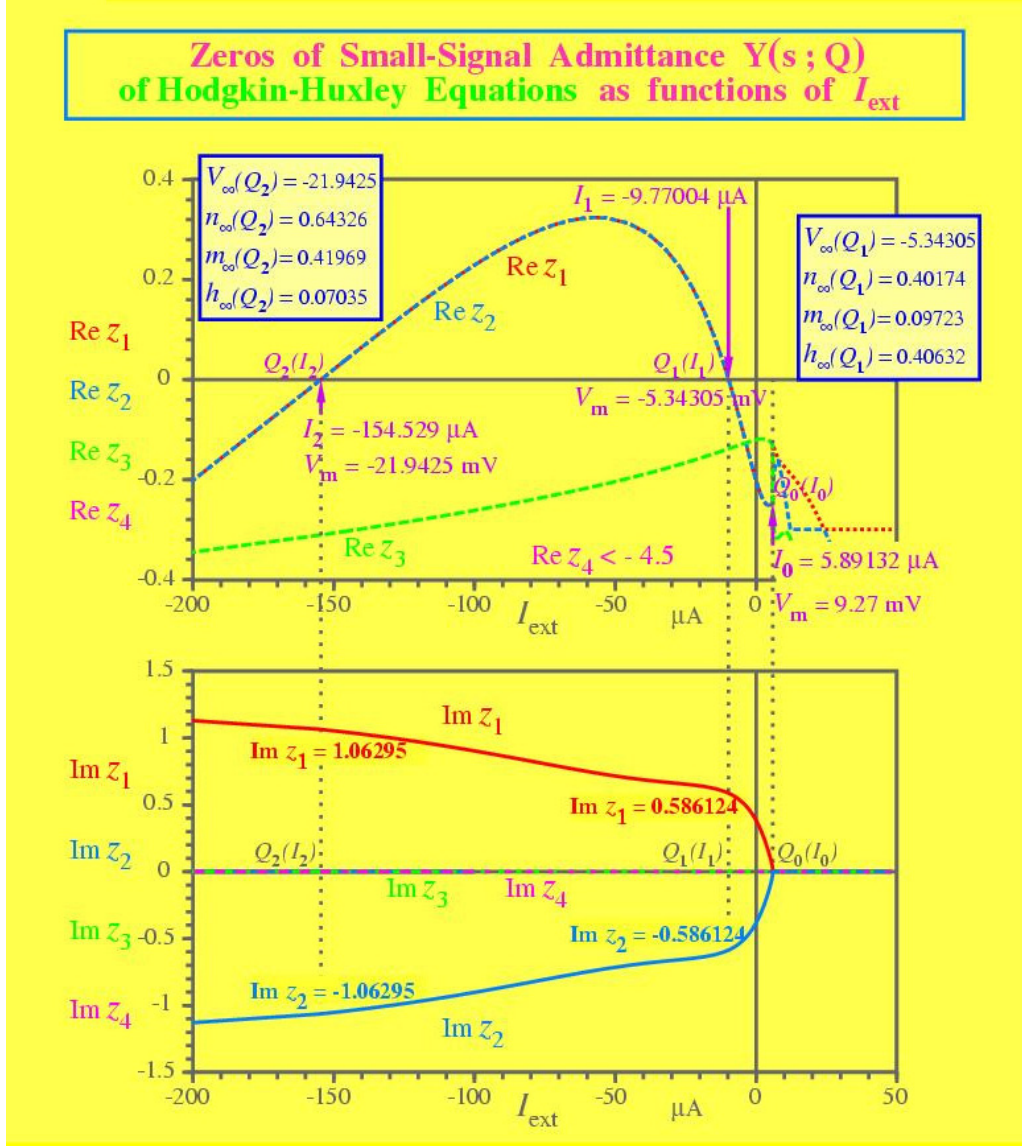
Observe also that at the *subcritical* Hopf bifurcation point, we have:

$$\text{Re } z_1 = \text{Re } z_2 = 0, \quad \text{at } I_{\text{ext}} = -9.77004 \mu\text{A}. \quad (27)$$

As we decrease $|I_{\text{ext}}|$, the loci of the zero z_1 in the upper RHP of Fig. 13 would initially move in a north east direction until it reaches the right-most point of the “red-nose” loci, where it would change direction and move along a northwest direction until it arrives once again at the imaginary axis at $I_{\text{ext}} = -154.529 \mu\text{A}$, or $V_m = -21.9425$ mV. This is precisely the point where the loci of $\text{Re } z_1$ and $\text{Re } z_2$ intersect the I_{ext} axis in Fig. 34.

Observe that $Y(s; Q)$ has a zero at $s = i(1.062951)$ in Fig. 23. If we plot $\text{Im } Y(i\omega)$ versus $\text{Re } Y(i\omega)$, we would obtain the Nyquist plot shown in Fig. 35.

Let us now focus our attention on the “red-nose” RHP loci in the upper part of Fig. 13 between the subcritical Hopf bifurcation point at $V_m = -5.34305$ mV and the point at $V_m = -21.9425$ mV. This point is identified in the upper figure of Fig. 34 as the equilibrium point $Q_1(I_1)$ where $I_1 = I_{\text{ext}}(Q_1) = -9.77004 \mu\text{A}$. As we decrease $|I_{\text{ext}}|$ from $I_{\text{ext}} = -9.77004 \mu\text{A}$ to $I_{\text{ext}} = -154.529 \mu\text{A}$, or equivalently, from $V_m = -5.34305$ mV to $V_m = -21.9425$ mV, we will end up at the upper intersection point between the “red-nose” loci and the

Fig. 34. Loci of the zeros of $Y(s; I_{\text{ext}})$ as a function of I_{ext} .

imaginary axis in Fig. 13, which we can identify as the equilibrium point $Q_2(I_2)$ in Fig. 34, where $I_2 = I_{\text{ext}}(Q_2) = -154.529 \mu\text{A}$. Indeed if we rotate the “red-nose” loci in Fig. 13 counterclockwise by 90° , we can see this loci maps in a one-to-one manner onto the red-blue hump in the upper part of Fig. 34.

Now recall that a *subcritical Hopf bifurcation* takes place at the equilibrium point $Q_1(I_1)$ in Fig. 34, giving rise to a large-magnitude spike (action potential) whose Lissajoux figure was projected onto the $I_{C_M} - V_m$ plane in Fig. 28(a). Over some limited neighborhood of $Q_1(I_1)$ in Fig. 34, the spike is found via detailed numerical simulations, to persist with only a slight decrease in the

“peak-to-peak amplitude” defined as follows:

$$A_{pp}(I_{\text{ext}}) = |\max V_m(t)| - |\min V_m(t)| \quad (28)$$

As we decrease $|I_{\text{ext}}|$ towards $I_{\text{ext}} = I_2 = -154.529 \mu\text{A}$ at $Q_2(I_2)$ in Fig. 34, we find that $A_{pp}(I_{\text{ext}})$ decreases monotonically, as depicted by the vertical distance between the upper blue boundary curve in the lower part of Fig. 36, representing the maximum value of the spike at I_{ext} , and the lower magenta boundary curve representing the minimum value of the spike at I_{ext} . These two boundary curves eventually meet at the equilibrium point $Q_2(I_2)$ depicted in Fig. 34 at $I_{\text{ext}} = I_2 = -154.529 \mu\text{A}$ where $A_{pp}(I_2) = 0$.

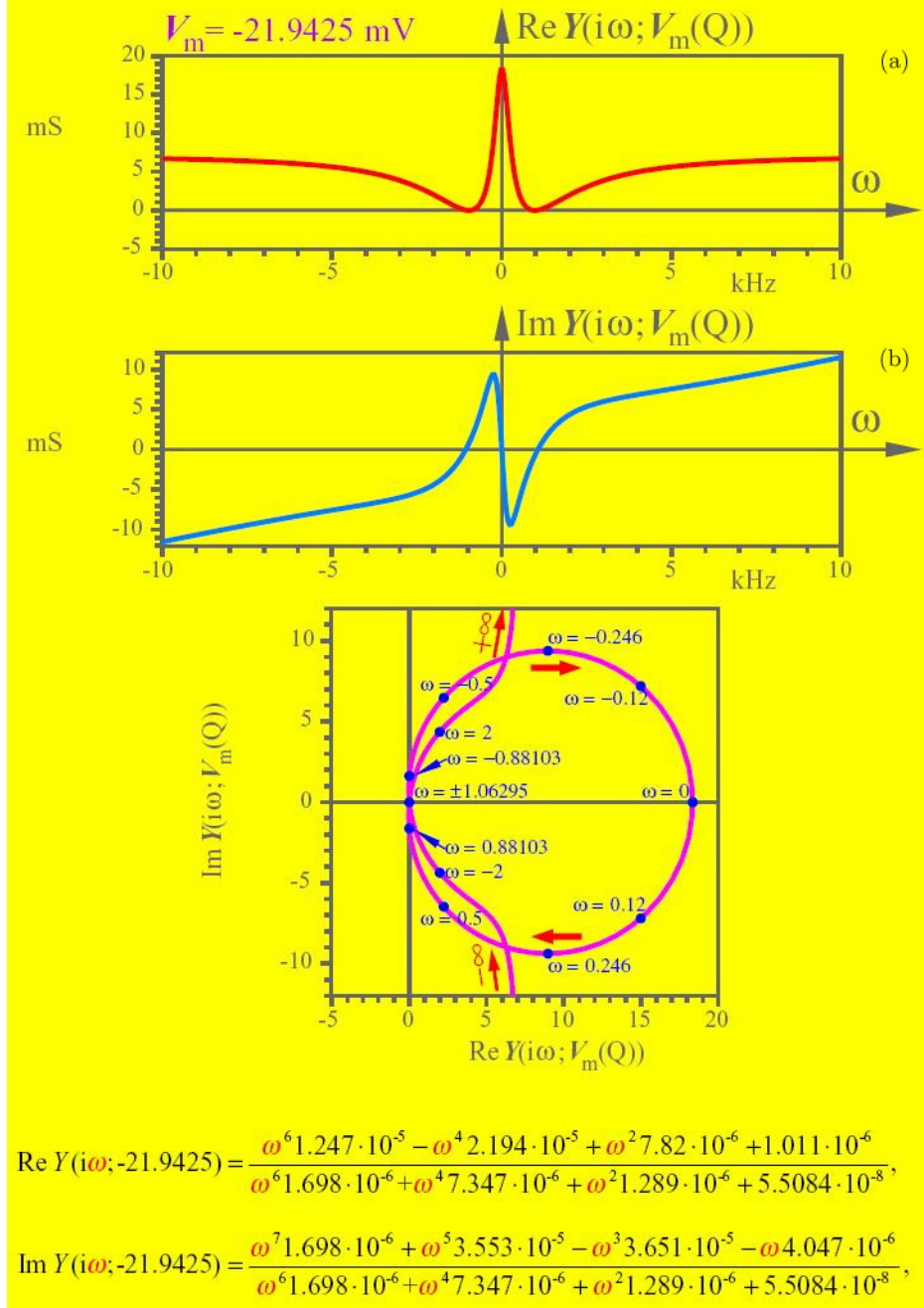


Fig. 35. Nyquist plot of $\text{Im } Y(i\omega; V_m(Q))$ versus $\text{Re } Y(i\omega; V_m(Q))$.

For $I_{\text{ext}} < -154.529 \mu\text{A}$, we find only a stable equilibrium point, which is not surprising since all zeros of $Y(s; I_{\text{ext}})$ have a *negative* real part for $I_{\text{ext}} < -154.529 \mu\text{A}$ as is evident from a cursory inspection of the upper part of Fig. 34.

In fact, a careful numerical simulation shows that a very small sinusoidal oscillation emerges as the upper “red-nose” loci in Fig. 13 crosses the imaginary axis from left to right transversally at $V_m = -21.9425 \text{ mV}$, which corresponds to $I_{\text{ext}} =$

$-154.529 \mu\text{A}$. Moreover, our numerical simulation shows the amplitude of the sinusoidal oscillation grows like the square root of $|I_{\text{ext}}|$ over a small increment in $|I_{\text{ext}}|$. All of these observations fit the fingerprint of a *super-critical* Hopf bifurcation at $Q_2(I_2)$ [Alligood et al., 1997].

The above bifurcation scenario is summarized in the lower part of Fig. 36 in the form of a three-prong fork where the center branch (cyan–magenta dashes) is part of the red DC V_m-I_m curve in

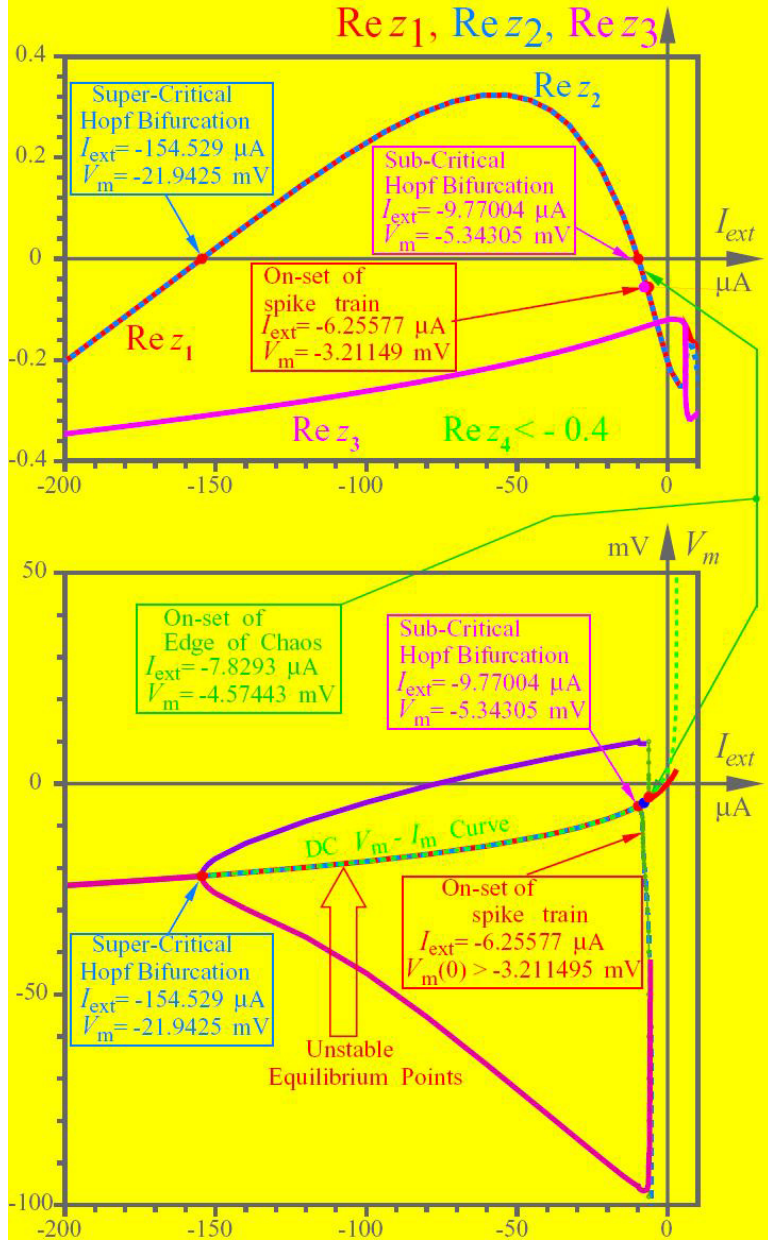


Fig. 36. Bifurcation diagram showing the subcritical Hopf bifurcation point $Q_1(I_1)$ at $I_1 = -9.77004 \mu A$ is connected via the unstable equilibrium loci (denoted by the alternating cyan–magenta DC $V_m - I_m$ curve) to the super-critical Hopf bifurcation point $Q_2(I_2)$ at $I_2 = -154.525 \mu A$.

the fourth quadrant derived earlier in Fig. 9(b). Observe that the segment of the DC $V_m - I_m$ between $Q_1(I_1)$ and $Q_2(I_2)$ is shown in alternating cyan–magenta color to emphasize that the zeros z_1 and z_2 of the admittance function $Y(s; I_{ext})$, or equivalently, the eigenvalues of the Jacobian matrix $J_{HH} = (V, n, m, h; I_{ext})$ of the Hodgkin–Huxley axon equation have a *positive real* part, implying that the equilibrium points on this segment are unstable.

We end this paper by selecting a sample of 12 points along the DC $V_m - I_m$ curve shown in Fig. 37

where the waveform of $V_m(t)$ at these points, corresponding to various initial conditions, are shown in Fig. 38.

Finally, we remark that the bifurcation diagram shown in Fig. 37 is virtually identical to that presented in Fig. 5.7 (page 210) of [Keener & Sneyd, 2009], which we reproduced in Fig. 39(a). Since the reference voltage polarity and direction adopted in [Keener & Sneyd, 2009] is the *negative* of those chosen in [Hodgkin & Huxley, 1952], and hence also of ours, we have replotted Fig. 37(a) with

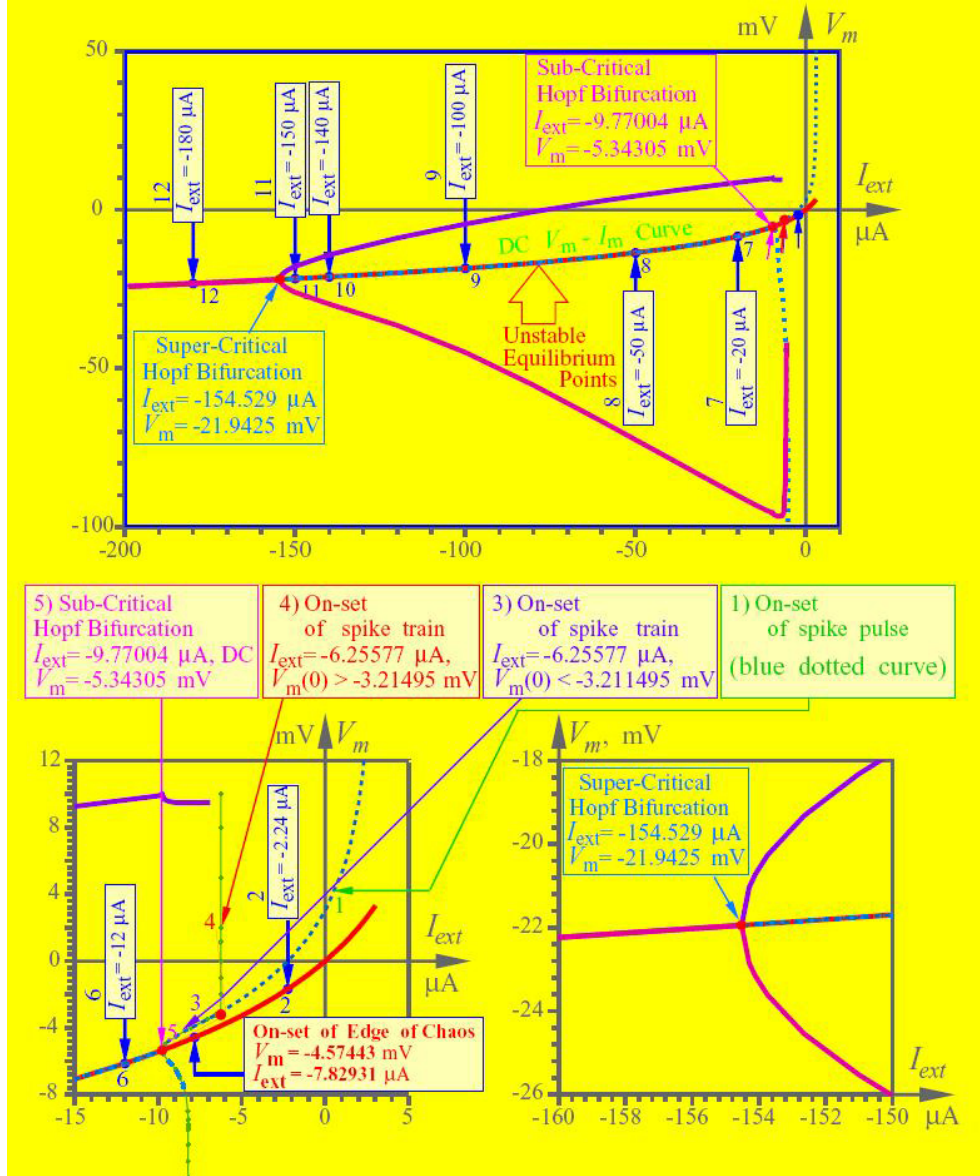


Fig. 37. Location of 12 sample points on the DC $V_m - I_m$ curve representing the equilibrium points of the Hodgkin–Huxley equation as a function of the DC excitation current I_{ext} . The left inset in the bottom is an enlargement around the *subcritical Hopf bifurcation point* $Q_1(I_1)$. The right inset is an enlargement around the *super-critical Hopf bifurcation point* $Q_2(I_2)$.

their reference convention in Fig. 39(b) for ease of comparison.

For the reader's convenience, we have calculated the waveform for $V_m(t)$ at 12 selected points (green) in Fig. 39(b) and exhibited them in Fig. 40. In each waveform, we have calculated the *maximum* steady-state value $\max V_m(\infty)$ and indicated its position along the upper (magenta) curve in Fig. 39(b) with the corresponding waveform sample number, $k = 1, 2, \dots, 12$. Similarly the corresponding *minimum* steady-state value $\min V_m(\infty)$ is indicated in the lower (blue) branch.

To confirm that the point ($I_{\text{ext}} = 154.515 \mu\text{A}$, $V_m = 21.9425 \text{ mV}$) in Fig. 39(b) corresponds to a *Super-Critical Hopf Bifurcation Point*, we have calculated the waveforms of $V_m(t)$ at eight additional points over the range $-151 \mu\text{A} < -I_{\text{ext}} < 154.525 \mu\text{A}$ and summarized the results in Fig. 41. Observe the rotated “parabola” bears the fingerprint of a Super-Critical Hopf Bifurcation.

The reader should note that the dotted middle branch shown in Fig. 39(a) is almost identical to the DC $V_m - I_m$ curve from Fig. 9(b),

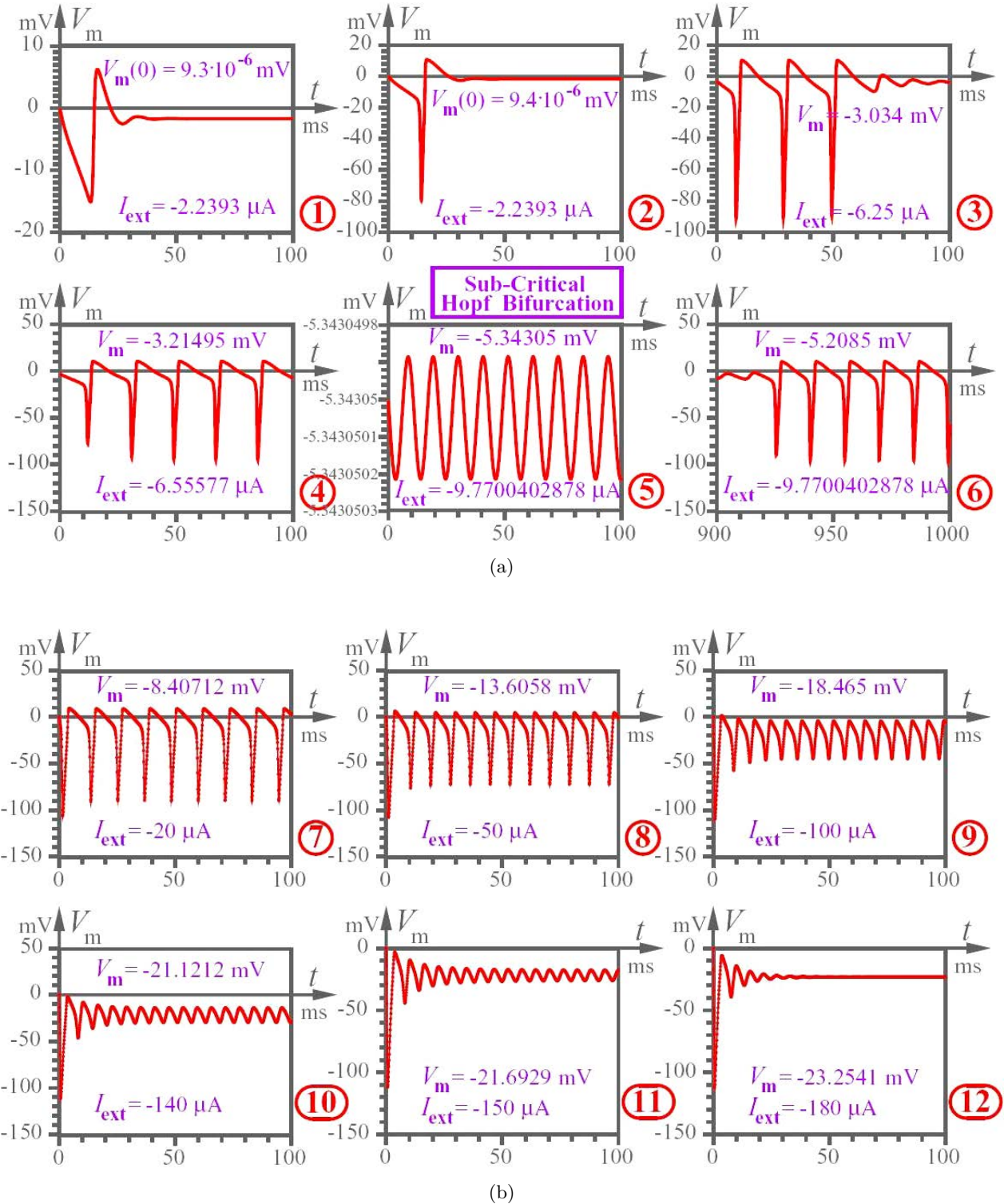


Fig. 38. Waveform of $V_m(t)$ of the Hodgkin-Huxley axon at 12 sampled equilibrium points on the DC V_m - I_m curve. (a) Points ① to ⑥. (b) Points ⑦ to ⑫.

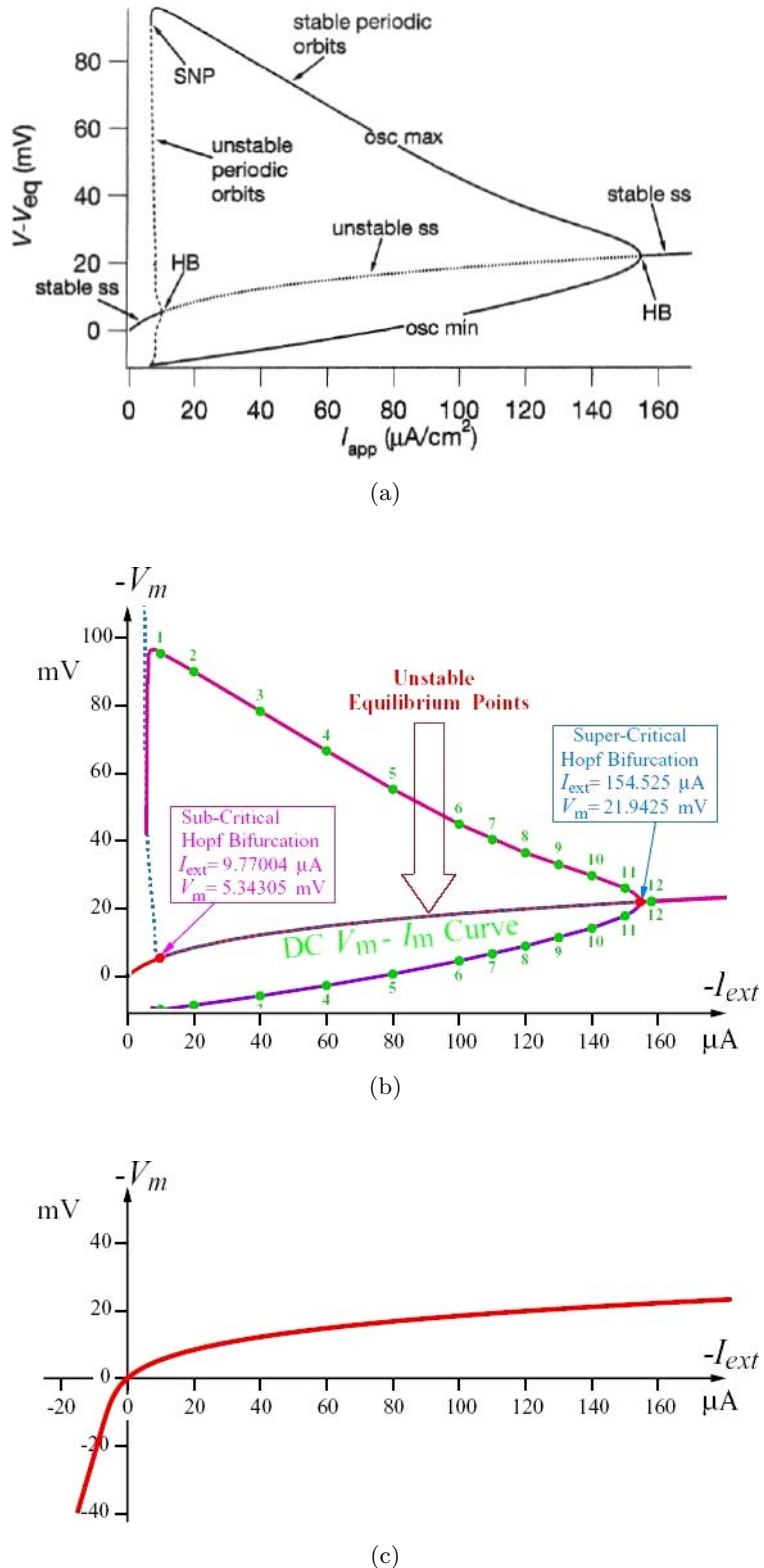


Fig. 39. Comparison of bifurcation diagram from [Keener & Sneyd, 2009] and Fig. 37. (a) Reproduction of Fig. 5.7 from [Keener & Sneyd, 2009]. (b) 180° rotation of the upper bifurcation curve from Fig. 37. (c) 180° rotation of the DC $V_m - I_m$ curve in the upper part of Fig. 37 (which is identical to Fig. 9(b)).

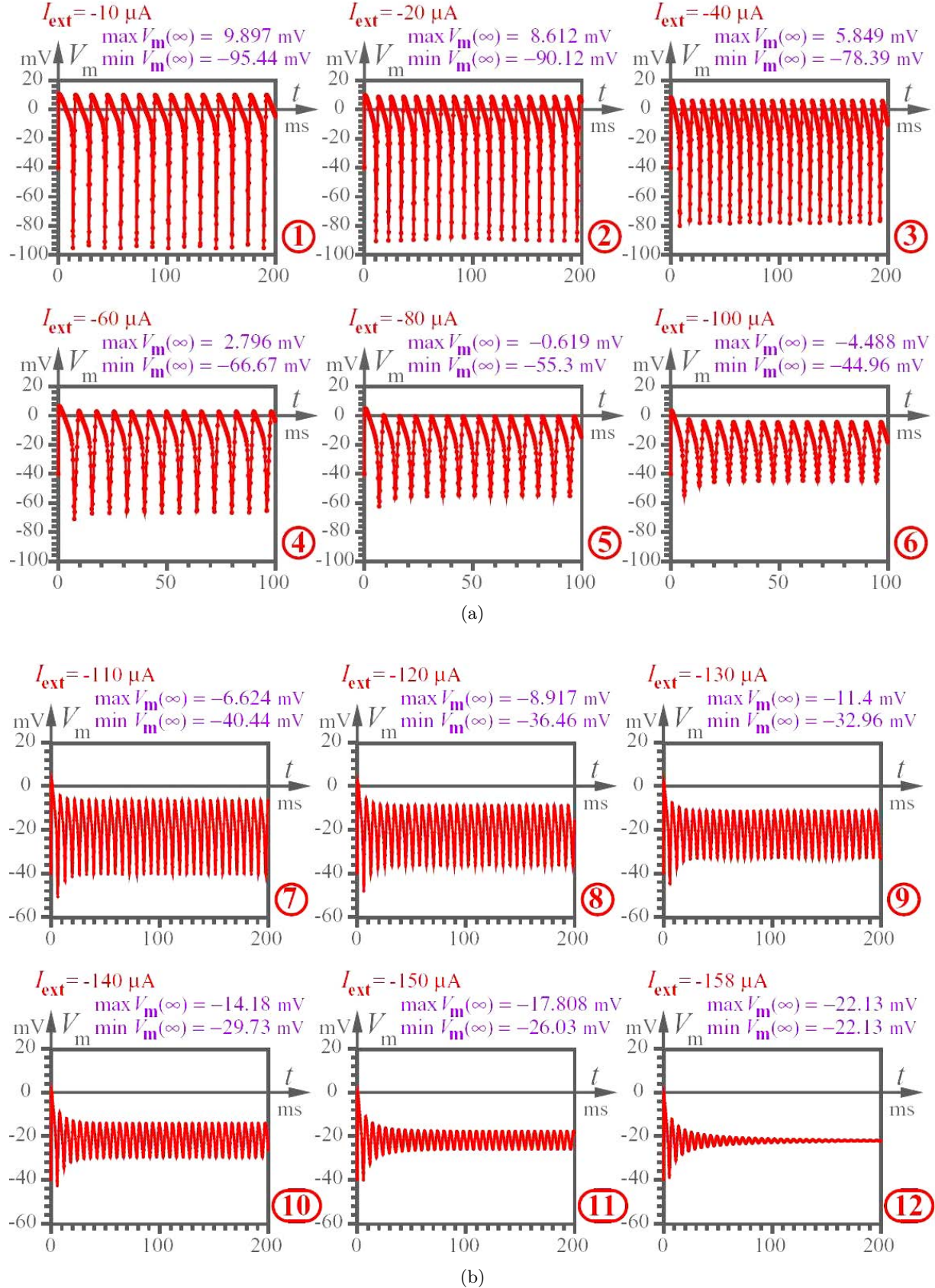


Fig. 40. Waveform of $V_m(t)$ with initial condition $V_m(0) = -40 \text{ mV}$, $m(0) = 0.8166592$, $n(0) = 0.8063613$, $h(0) = 0.0127928$.
(a) Sample points ①, ②, ..., ⑥. (b) Sample points ⑦, ⑧, ..., ⑫.

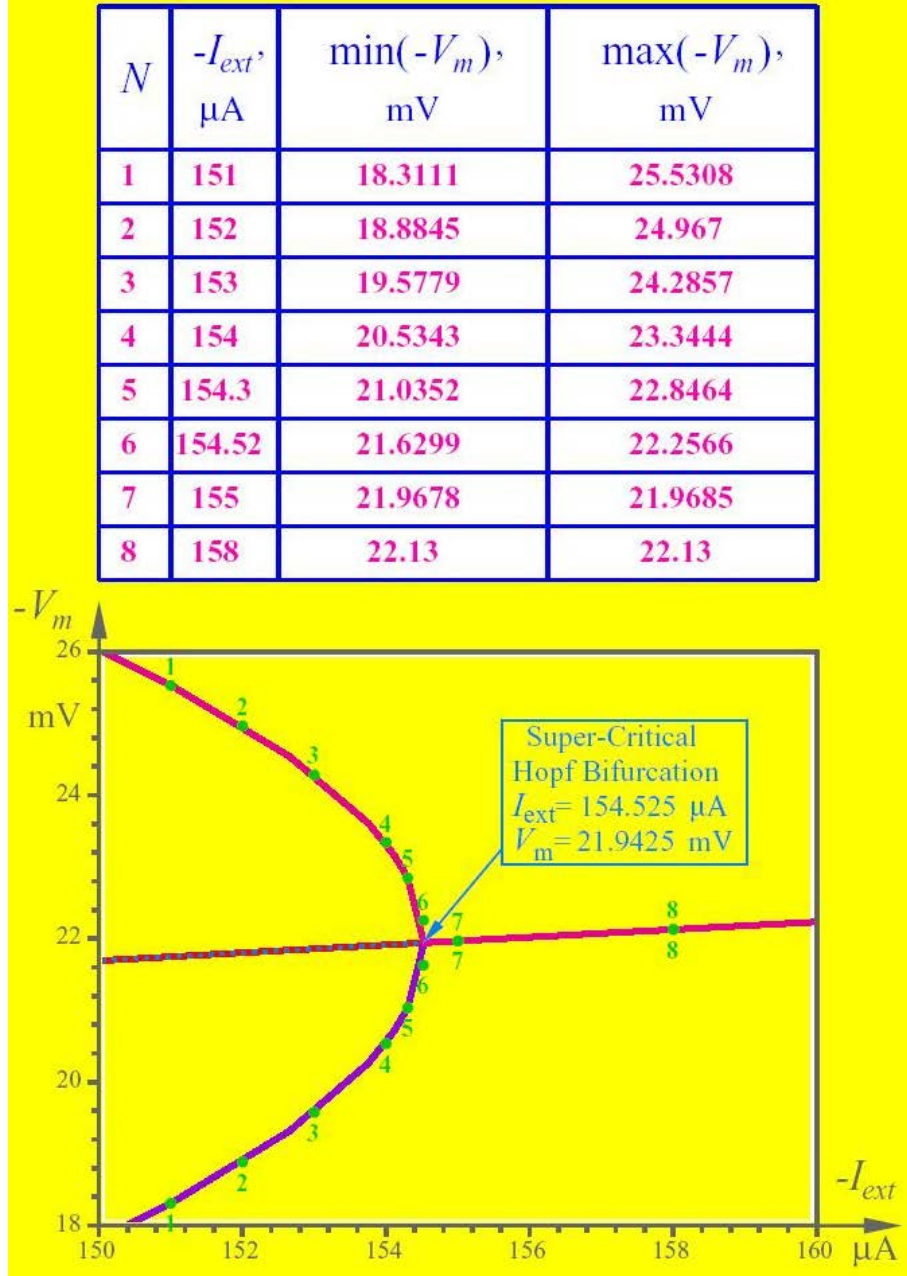


Fig. 41. Loci of maximum and minimum of the steady-state waveform $V_m(t)$ over the range $-150 \mu\text{A} < -I_{ext} < 160 \mu\text{A}$.

which we reproduced in Fig. 39(c) for comparison. It is indeed quite remarkable that these two bifurcation diagrams are virtually identical, using two entirely different approaches. The bifurcation diagram in Fig. 39(a) was obtained by [Keener & Sneyd, 2009] via the numerical software package XPPAUT [Ermentrout, 2002]. In sharp contrast, our bifurcation diagram was obtained by finding the roots of a fourth degree polynomial equation, which

we have proved to be identical to the eigenvalues of the Jacobian matrix $J_{\text{HH}} = (V, n, m, h; I_{ext})$ of the Hodgkin–Huxley equation.

Acknowledgments

This research is supported in part by a Guggenheim Fellowship and by an AFOSR grant no. FA9550-10-1-0290.

The authors would also like to thank Maheshwar Prasad Sah and Ram Kaji Budhathoki for their assistance in the preparation of this manuscript.

References

- Alligood, K. T., Sauer, T. D. & Yorke, J. M. [1997] *Chaos: An Introduction to Dynamical Systems* (Springer-Verlag, NY).
- Chua, L. O. [1969] *Introduction to Nonlinear Network Theory* (McGraw-Hill Book Co., NY).
- Chua, L. O. [1978] “Nonlinear circuit theory,” *Modern Network Theory — An Introduction*, ed. Brayton, R. K. et al. (Georgi, St-Saphorin Switzerland).
- Chua, L. O. [1980] “Device modeling via basic nonlinear circuit elements,” *IEEE Trans. Circuits Syst. CAS-27*, 1014–1044.
- Chua, L. O., Desoer, C. A. & Kuh, E. S. [1987] *Linear and Nonlinear Circuits* (McGraw-Hill Book Co., NY).
- Chua, L. O. [1998] *CNN: A Paradigm for Complexity* (World Scientific, Singapore).
- Chua, L. O. [2005] “Local activity is the origin of complexity,” *Int. J. Bifurcation and Chaos* **15**, 3435–3456.
- Chua, L. O., Sbitnev, V. & Kim, H. [2012] “Hodgkin–Huxley axon is made of memristors,” *Int. J. Bifurcation and Chaos* **22**, 1230011-1–48.
- Ermentrout, B. [2002] *Simulating, Analyzing, and Animating Dynamical Systems: A Guide to XPPAUT for Researchers and Students* (SIAM, Philadelphia).
- Haken, H. [1983] *Synergetic, An Introduction*, 3rd edition (Springer-Verlag, Berlin).
- Hassard, B. [1978] “Bifurcation of periodic solutions of the Hodgkin–Huxley model for the squid giant axon,” *J. Theor. Biol.* **71**, 401–420.
- Hodgkin, A. L. & Huxley, A. F. [1952] “A quantitative description of membrane current and its application to conduction and excitation in nerve,” *J. Physiol.* **117**, 500–544.
- Keener, J. & Sneyd, J. [2009] *Mathematical Physiology I: Cellular Physiology*, 2nd edition (Springer, NY).
- Prigogine, I. [1980] *From Being to Becoming* (Freeman, San Francisco).
- Schrodinger, E. [1944] *What is Life* (Cambridge University Press, London).
- Smale, S. [1974] “A mathematical model of two cells via Turing’s equations,” *Lectures in Applied Mathematics* **6**, 15–26.
- Turing, A. M. [1952] “The chemical basis of morphogenesis,” *Philos. Trans. Roy. Soc. London, Series B* **237**, 37–72.
- Yang, T. & Chua, L. O. [2001] “Testing for local activity and edge of chaos,” *Int. J. Bifurcation and Chaos* **11**, 1495–1591.